

---

Theses and Dissertations

---

Fall 2010

# Nonlinear optics in Bragg-spaced quantum wells

Wesley James Johnston  
*University of Iowa*

Copyright 2010 Wesley James Johnston

This dissertation is available at Iowa Research Online: <http://ir.uiowa.edu/etd/826>

---

## Recommended Citation

Johnston, Wesley James. "Nonlinear optics in Bragg-spaced quantum wells." PhD (Doctor of Philosophy) thesis, University of Iowa, 2010.  
<http://ir.uiowa.edu/etd/826>.

---

Follow this and additional works at: <http://ir.uiowa.edu/etd>

 Part of the [Physics Commons](#)

NONLINEAR OPTICS IN BRAGG-SPACED QUANTUM WELLS

by

Wesley James Johnston

An Abstract

Of a thesis submitted in partial fulfillment of the  
requirements for the Doctor of Philosophy  
degree in Physics in the  
Graduate College of The  
University of Iowa

December 2010

Thesis Supervisor: Associate Professor John Prineas

## ABSTRACT

Bragg spaced quantum wells represent a unique class of resonant photonic materials, wherein a photonic bandgap is created by the periodic spacing of quantum wells and the associated variation in the complex susceptibility (index and absorption) of the material. Interest in BSQWs has grown in the past decade due to their large ultrafast nonlinearities and the corresponding large ultrafast reflectivity changes and transmissivity. These nonlinearities are of particular interest in areas of communication technology, where ultrafast all-optical logic components have become increasingly in demand. This research will further investigate BSQWs and the for the first time effects of spin-dependent nonlinear excitation on their photonic band structures. It will also investigate how these effects can be used in all-optical polarization switching and tunable optical buffer (slow light) applications.

Abstract Approved: \_\_\_\_\_  
Thesis Supervisor

\_\_\_\_\_  
Title and Department

\_\_\_\_\_  
Date

NONLINEAR OPTICS IN BRAGG-SPACED QUANTUM WELLS

by

Wesley James Johnston

A thesis submitted in partial fulfillment of the  
requirements for the Doctor of Philosophy  
degree in Physics in the  
Graduate College of The  
University of Iowa

December 2010

Thesis Supervisor: Associate Professor John Prineas

Copyright by  
WESLEY JAMES JOHNSTON  
2010  
All Rights Reserved

Graduate College  
The University of Iowa  
Iowa City, Iowa

CERTIFICATE OF APPROVAL

---

PH.D. THESIS

---

This is to certify that the Ph.D. thesis of

Wesley James Johnston

has been approved by the Examining Committee  
for the thesis requirement for the Doctor of  
Philosophy degree in Physics at the  
December 2010 graduation.

Thesis Committee: \_\_\_\_\_  
John P. Prineas, Thesis Supervisor

\_\_\_\_\_  
David R. Anderson

\_\_\_\_\_  
Thomas F. Boggess Jr.

\_\_\_\_\_  
Christopher M. Cheatum

\_\_\_\_\_  
Craig E. Pryor

Dedicated to my mom.

## ACKNOWLEDGMENTS

I would like to acknowledge John Prineas and Arthur Smirl for the time they spent teaching and tutoring me on aspects of this research from data collection to analysis, as well the other members of my dissertation committee, David Anderson, Craig Pryor, Tom Boggess, and Chris Cheatum. I would also like to acknowledge my wonderful wife, Monica Lees for putting up with a lot of late nights and an occasionally grouchy personality.

Some of this information is reproduced with the permission of the American Institute of Physics. In particular Section 3.1 is reprinted with permission from:

- W. J. Johnston, M. Yildirim, J. P. Prineas, A. L. Smirl, H. M. Gibbs, and G. Khitrova. "All-optical spin-dependent polarization switching in Bragg-spaced quantum well structures". *Applied Physics Letters*, 87(10):101113, 2005, and
- W. J. Johnston, J. P. Prineas, and A. L. Smirl. "Ultrafast all-optical polarization switching in Bragg-spaced quantum wells at 80 K". *Journal of Applied Physics*, 101(4):046101, 2007.

Section 3.2 is reprinted with permission from:

- J. P. Prineas, W. J. Johnston, M. Yildirim, J. Zhao, and Arthur L. Smirl. "Tunable slow light in Bragg-spaced quantum wells". *Applied Physics Letters*, 89:241106, 2006.

## ABSTRACT

Bragg spaced quantum wells represent a unique class of resonant photonic materials, wherein a photonic bandgap is created by the periodic spacing of quantum wells and the associated variation in the complex susceptibility (index and absorption) of the material. Interest in BSQWs has grown in the past decade due to their large ultrafast nonlinearities and the corresponding large ultrafast reflectivity changes and transmissivity. These nonlinearities are of particular interest in areas of communication technology, where ultrafast all-optical logic components have become increasingly in demand. This research will further investigate BSQWs and for the first time effects of spin-dependent nonlinear excitation on their photonic band structures. It will also investigate how these effects can be used in all-optical polarization switching and tunable optical buffer (slow light) applications.

## TABLE OF CONTENTS

LIST OF FIGURES . . . . .	vii
LIST OF ABBREVIATIONS AND SYMBOLS . . . . .	xiv
CHAPTER	
1 INTRODUCTION . . . . .	1
2 BACKGROUND . . . . .	5
2.1 Basics of semiconductor materials . . . . .	5
2.2 Fabrication of layered semiconductor structures . . . . .	8
2.3 Quantum well basics . . . . .	9
2.4 Nonlinear effects in semiconductor quantum wells . . . . .	12
2.5 Fabrication of Bragg-spaced quantum wells . . . . .	15
2.6 Using a transfer matrix to model optical properties of layered structures . . . . .	18
2.7 Linear properties of Bragg-spaced quantum wells . . . . .	21
2.8 History of studying nonlinearities in photonic crystals . . . . .	25
2.9 Applications of Bragg-spaced quantum wells in modern communication systems . . . . .	26
2.10 All-optical switching . . . . .	29
2.10.1 Amplitude switching . . . . .	31
2.10.2 Polarization switching . . . . .	33
3 RESEARCH . . . . .	39
3.1 All-optical polarization switching in Bragg-spaced quantum wells . . . . .	39
3.1.1 10K All-optical polarization switch . . . . .	40
3.1.2 80K All-optical polarization switch . . . . .	44
3.2 Slow light and optical buffers using Bragg-spaced quantum wells . . . . .	51
3.3 Nonlinearities in Bragg-spaced quantum wells . . . . .	62
3.3.1 Broadband measurements of the nonlinear response . . . . .	62
3.3.2 Measurement of nonlinearities in BSQWs using narrow-band probe pulses . . . . .	72
3.3.3 Time delay dependence of the nonlinear response . . . . .	75
3.3.4 Preliminary theoretical analysis of the nonlinear response of BSQWs . . . . .	77
3.3.5 Preliminary polarization state measurements . . . . .	80
3.3.6 Summary of nonlinear measurements of Bragg-spaced quantum wells . . . . .	85
4 FUTURE RESEARCH . . . . .	88
4.1 Pulse amplification . . . . .	88
4.2 All-optical switching . . . . .	89

4.3	Slow light . . . . .	90
4.4	Alternative materials . . . . .	91
5	CONCLUSIONS . . . . .	94
APPENDIX		
A	TRANSFER MATRIX DERIVATION . . . . .	97
A.1	Maxwell's equations . . . . .	97
A.2	Transfer matrix for non-resonant media . . . . .	98
A.3	Transfer matrix with quantum well susceptibility . . . . .	99
A.4	Bloch Equations . . . . .	101
B	TRANSFER MATRIX SOLUTIONS FOR THE PHOTONIC BAND- STRUCTURE AND REFLECTIVITY OF BSQWS . . . . .	106
REFERENCES		

## LIST OF FIGURES

1.1	Schematic of a one layer anti-reflection coating. . . . .	1
1.2	Schematic of a 3D photonic crystal. The periodicity in this case extends in three dimensions rather than one. . . . .	2
1.3	Schematic of an resonant photonic material. Rather than varying just the index of the materials, materials with a resonance at the same frequency as the periodicity are used. . . . .	4
2.1	Schematic of a <i>III-V</i> semiconductor unit cell. . . . .	5
2.2	On the left is a schematic electronic band structure for a <i>III-V</i> semiconductor. This is an one particle picture showing allowed levels for electrons in the <i>hh</i> , <i>lh</i> , and <i>so</i> valence bands, as well as the lowest lying conduction band. On the right is the two particle, excitonic band structure. Since excitons do not exist until a particle has been excited, there is no “ground” state. . .	6
2.3	Schematic of quantum well band structure versus position in the <i>z</i> -direction. Conduction band energies and valence band energies are shown. (a) represents type-I quantum wells. (b) represents type-II quantum wells. $E_B$ and $E_W$ represent the bandgap of the semiconductor materials inside the barrier and well layers respectively. . . . .	8
2.4	Optical selection rules coupling left ( $\sigma+$ ) and right ( $\sigma-$ ) circularly polarized light between the <i>hh</i> and <i>lh</i> valence band electrons and excited conduction band electrons. Many body effects which can allow the two systems to interact are indicated in red. . . . .	11
2.5	Schematic of Pauli-blocking (a) and Hartree-Fock (b) effects. . .	12
2.6	Schematic of bound (a) and unbound (b) biexciton states. . . .	14
2.7	Schematic of a BSQWs. The light shaded (blue) areas represent barriers made of GaAs, and the dark shaded (red) ones $\text{In}_{0.04}\text{Ga}_{0.96}\text{As}$ layers. The spacing between the wells, $a$ , determines the Bragg resonance, $\omega_B$ . Electric fields used in calculating the transfer matrix (see Section 2.6) between individual layers are also shown. . . . .	16

2.8	Reflection from glass with (solid) and without (dotted) an anti-reflection coating. The anti-reflection coating has a width is equal to $\lambda/4n_1$ where $\lambda = 1.5$ eV and $n_1$ (the refractive index of the layer) is 1.225. . . . .	21
2.9	Photonic bandstructure of Bragg-spaced quantum wells. (a) Calculated photonic band structure using Eq. 2.21. Solid blue lines show the band structure when $\omega_B = \omega_X$ and the dotted red lines show the band structure when $1.001\omega_B = \omega_X$ . (b) A calculation of the reflection from BSQWs when $\omega_B = \omega_X$ (blue, solid) and $\omega_B \neq \omega_X$ (red, dashed). . . . .	24
2.10	Applications of Bragg-spaced quantum wells. (a) An example of using an optical switch to temporally filter a long signal. (b) Using optical delay lines to synchronize and time division multiplex several signals. . . . .	28
2.11	Setup of an amplitude optical switching experiment. The pump pulse (red solid) induces a nonlinearity in the structure, the changes the reflection of a signal pulse (blue dashed). Those changes are detected as switching signals. . . . .	29
2.12	Setup of an all-optical polarization switching experiment. The circularly polarized pump pulse (red, solid) induces a nonlinearity in the structure for one circular polarization, creating a circular-dichroism and/or circular-birefringence. These cause the linearly polarized probe pulse's (blue, dashed) polarization to be rotated, and the changes are detected as switching signals. . . . .	34
3.1	All-optical switching in Bragg-spaced quantum wells. (a) Setup for switching experiments with the probe pulse spectrally resolved after the switching material. (b) Contrast ratio (solid circles) as a function of control-signal delay ( $\tau$ ) for a $14 \mu\text{J}/\text{cm}^2$ , 1 ps control pulse, and a 650 fs signal pulse spectrally positioned as shown in Fig 3.2. The temporally resolved control pulse (solid line) is shown for comparison. Reproduced with permission from Ref. [1]. . . . .	40
3.2	The reflectivity stop band of the 200 period BSQW when excited by a right circularly polarized $\sigma+$ , $14 \mu\text{J}/\text{cm}^2$ , 1 ps control pulse (spectrum of the control pulse indicated by the shaded dark gray area) as measured by a broadband signal pulse (21 meV, spectrally centered at the position of the arrow) having the same circular polarization, $\sigma+$ , (solid red line) and the opposite circular polarization, $\sigma-$ , (dashed blue line). The measured reflectivity stop bands without the control for both $\sigma+$ and $\sigma-$ polarizations are indicated by the light gray shaded area. Reproduced with permission from Ref. [1]. . . . .	41

3.3	The differential reflectivity for control and signal pulses with same (a) and opposite (b) circular polarizations, for signal-control time delays of $\tau = 0$ ps (solid, black squares), $\tau = +10$ ps (solid, red line), and $\tau = -10$ ps, (dashed, blue line). All energies are plotted relative to the $hh$ exciton resonance, $E_x = 1.4994$ eV. Reproduced with permission from Ref. [1]. . . . .	43
3.4	Spectrally resolved contrast ratio (solid blue line) and throughput (dashed red line) for the $14 \mu\text{J}/\text{cm}^2$ 1 ps control pulse used in Fig. 3.1(b) and 3.3 and shown in Fig. 3.2 at $\tau = 0$ ps. Spectra were taken using the experimental geometry shown in the inset to Fig. 3.1(b)(inset) and a spectrally broad signal pulse (21 meV). The linear reflectivity stop band is shown for reference (shaded area). Reproduced with permission from Ref. [1]. . . . .	44
3.5	Simulated reflection (black), absorption (blue), and transmission (red) from a BSQW with two different exciton dephasing rates (0.1 meV solid, 0.5 meV dashed) (see Ref. [2]) . . . . .	45
3.6	Setup for all-optical switching in Bragg-spaced quantum wells at 80K. (a) Linear reflection (light gray shading) of the reflection stopgap. Dark gray shading shows the spectral position of the control used for high temperature switching measurements. Spectral shape of the signal is shown by the blue dashed line. Inset shows the temporally resolved signal (blue dashed line) and control (dark gray shaded) pulses with an 80 fs gating pulse. (b) Experimental setup for high temperature switching. Reproduced with permission from Ref. [3]. . . . .	46
3.7	Reflection of a broadband, $\sigma+$ polarized probe pulse (27 meV, 80 fs) as a function of $\sigma+$ pump spectral position (dark shaded area, 1.3 meV, 1.2 ps). Reflection was measured at pump-probe delays of $-10$ ps (light shading), $0$ ps (red, solid) and $+10$ ps (blue, dashed) in each case. Reproduced with permission from Ref. [3]. . . . .	48
3.8	Performance of all-optical switching in Bragg-spaced quantum wells at 80K. (a) Maximum recorded contrast ratio (solid circles) and throughput (red squares) as a function of center signal frequency. Linear reflection from the BSQW is shown in light shading. (b) Measured contrast ratio vs. control-signal time delay (blue, solid) and control fluence (c) at the spectral position showing maximum contrast ratio in (a). The dotted line in (b) indicates a contrast ratio of 1 (switch off). Control-signal cross correlation is shown in (b) for reference (black, dashed). Inset in (b) shows the contrast ratio plotted on a logarithmic scale. (c) also lists the corresponding throughput for each control fluence. Reproduced with permission from Ref. [3]. . . . .	49

- 3.9 Differential reflection vs. pump-probe time delay for the spectrally narrow probe pulse shown in Fig. 3.7. Probe with the opposite (same) circular polarization as the pump is shown in part (a) (part (b)). Reproduced with permission from Ref. [3]. 50
- 3.10 Simulations of slow light in Bragg-spaced quantum wells. (a) Simulated bandstructure of a detuned ( $\Delta\omega = \omega_B - \omega_x = -3.0$  meV), Bragg-spaced quantum well structure with unit cell parameters chosen to match those of  $\text{In}_{0.025}\text{Ga}_{0.975}\text{As}/\text{GaAs}$  quantum wells:  $\omega_B = 1.491$  eV,  $\omega_x = 1.494$  eV,  $\Gamma = 30\mu$  eV the radiative damping rate,  $\gamma = 0.15$  meV the dephasing rate, and  $n_b = 3.61$ . (b) Simulated group velocity of a Bragg-spaced quantum well structure at two detunings,  $\Delta\omega = \omega_B - \omega_x = -3.0$  meV (red, solid) and  $\Delta\omega = -1.25$  meV (blue, dashed). By varying the detuning  $\Delta\omega$ , the group velocity of the pulse is continuously tunable (inset). Reproduced with permission from Ref. [4]. . . . . 53
- 3.11 Spectrally resolved slow light in Bragg-spaced quantum wells. (a) Simulated reflection (black, solid) from, transmission (red, dashed) through, and absorption (blue, dotted) by an  $N = 210$  Bragg-spaced  $\text{In}_{0.025}\text{Ga}_{0.975}\text{As}/\text{GaAs}$  quantum well structure. (b) Low temperature measurements (10K) on the corresponding experimental structure. (c) Measured relative delay (black, square) and pulse broadening (blue, triangle) of a 0.67 meV (3.5 ps) pulse, shown for reference in black/gray fill. Reproduced with permission from Ref. [4]. . . . . 55
- 3.12 Measured temporally-resolved 0.67 meV, 3.5 ps pulses transmitted through the experimental structure of Fig. 3.11. Pulses were centered on photon energies  $E - E_x = -0.79$  meV,  $-1.08$  meV,  $-2.26$  meV,  $-11.51$  meV for the blue dash-dot line, the dark yellow dotted line, the red dashed line, and the black solid line, respectively. Delays are relative to the transmitted pulse at  $-11.51$  meV. Reproduced with permission from Ref. [4]. . . . 57
- 3.13 Simulation of a Bragg-spaced quantum well sample identical to Fig. 3.11 except with antireflection coatings on the front and exit interfaces designed for (a)  $\Delta\omega = -3.3$  meV and (b)  $\Delta\omega = 22$  meV, including reflection (black, solid), transmission (red, dashed), and absorption (blue, dotted). (c) Measured reflection, transmission, and absorption of an experimental sample with target structure of (a), but actual structure closer to (b). The percentage error in antireflection coating layer thicknesses equals 1.5%. (d) Measured relative delay (black, square) and pulse broadening (blue, triangle) of a 0.67 meV (3.5 ps) pulse, shown for reference in black/gray fill. Reproduced with permission from Ref. [4]. . . . . 58

3.14	Setup for nonlinear measurements. (a) Reflection spectrum of a $\sigma+$ (blue, solid) and $\sigma-$ (red, dashed) polarized probe at $\tau = 0$ ps pump-probe delay for a $\sigma+$ polarized pump. The linear reflection from the structure is shown in the light shaded area. The pump (dark shaded) and incident probe (black, dotted) spectrums are shown for reference. (b) Schematic experimental setup for nonlinear measurements. A strong $\sigma+$ polarized spectrally shaped pump (red solid), and weak $\sigma+$ or $\sigma-$ polarized probe (black dashed) are incident on the BSQW structure. Signals in both the reflected (R, black dashed line); the backwards probe, background-free four-wave mixing (FWM, blue dotted line); and in the transmission direction (T, green solid line) directions are detected. . . . .	63
3.15	Spectrally resolved reflection, transmission and background free signals of a $\sigma+$ polarized probe at time delays ranging from $-3$ ps to $+3$ ps. . . . .	65
3.16	Spectrally resolved reflection, transmission and background free signals of a $\sigma-$ polarized probe as a function of time delay ( $-3$ ps to $+3$ ps) with respect to a $\sigma+$ pump. Background-free signals are plotted in the same arbitrary units as the background-free signals in Fig. 3.15. . . . .	66
3.17	Intensity of the background-free four-wave-mixing (FWM) signal versus pump intensity (round, hollow), and probe intensity (square, solid). Fit lines (red, quadratic for the pump and blue, linear for the probe) are shown for reference. . . . .	68
3.18	Numerically integrated differential reflection (blue, hollow circles) and transmission (red, filled squares) at different time delays. Also included is $\Delta S - \Delta A = \Delta R + \Delta T$ at each time delay (black, hollow triangles). . . . .	71
3.19	Experimental setup for narrowband measurements. . . . .	72
3.20	Spectrally resolved reflection as a function of pump-probe time delay. (left) Integrated measurements of the narrowband probe vs. pump-probe delay. Note that the x-axis in this case is the energy at the center of the probe pulse. (right) Similar results taken with a broadband probe. The x-axis in this case is the absolute energy being spectrally resolved. . . . .	73
3.21	Spectrally resolved reflection (red filled squares) and differential intensity (blue open diamonds) of a narrowband probe (black solid line) co-circularly polarized with the pump vs. pump-probe delay. Rows show different time delays ranging from $\tau = -2.5$ ps (top) to $\tau = +2$ ps (bottom). The pump spectrum (dark shaded area) and linear reflection from the structure (light shaded area) are shown for reference. . . . .	74

3.22	Comparisons of simulated and measured reflection. (a) Experimentally measured reflection at pump-probe delays of $-1.5\text{ps}$ (black, solid), $-1.0\text{ps}$ (blue, dashed) and $-0.5\text{ps}$ (red, dotted). (b) Theoretically simulated reflection at $-2.0\text{ps}$ (black, solid), $-1.0\text{ps}$ (blue, dashed) and $-0.6\text{ps}$ (red, dotted). The pump (dark gray shaded area) and linear reflection (light gray shaded area) spectrum are shown for reference. . . . .	78
3.23	Simulated signals traveling in the backwards probe, background free direction, at $\tau = 0\text{ps}$ pump-probe delay ((a)), and in the transmission direction at $\tau = +1\text{ps}$ pump-probe delay ((b)). The pump (dark gray shaded area) and linear reflection (light gray shaded area) spectrum are shown for reference. . . . .	78
3.24	Theoretically modeled reflection with all many body effects (solid, blue) included to beyond third order, and only the Hartree-Fock interaction to third order (dashed, red) at a pump-probe delay of $-1\text{ps}$ . In all figures the linear reflection is shown in the light shaded area, and the pump in the dark shaded area. . . . .	79
3.25	The polarization ellipse used for these measurements. $P$ , $\theta_{\text{sig}}$ and $\epsilon$ are shown, along with the major (a) and minor (b) axes of the ellipse. . . . .	81
3.26	Experimental setup for measuring the polarization state of a pulse. A $\lambda/4$ plate, $\lambda/2$ plate and a polarizer are placed in the beam path after the sample. Different orientations of the three allow measuring the linear polarization along 4-axes and both circular polarization components. . . . .	83
3.27	Preliminary measurements of the spectrally and temporally integrated polarization state of the probe pulse. The total polarization state (black), along with the orientation (red) and ellipticity (blue) of the pulse are shown at $\tau = 0\text{ps}$ pump-probe delay. . . . .	84
4.1	Schematic of a periodic ring resonator array. In this particular example, a series of ring resonators are arranged between two waveguides. The rings contain a resonance based on the radius of the ring and its material parameters (index, absorption, etc). By arranging them in periodic arrays separated by some distance (a), the photonic properties of the rings can be altered. These and other photonic materials are candidates for next generation all-optical computing platforms and as mediums for tunable slow light. . . . .	91
A.1	Transfer matrix across an interface between two materials. . . . .	98

A.2 A simple closed two level system with individual level decay rates,  $\gamma_{ab}$ . . . . . 101

## LIST OF ABBREVIATIONS AND SYMBOLS

$\text{\AA}$	Angstrom, $10^{-10}$ m
$\wp$	Oscillator strength of an exciton
$\hbar$	Plank's constant / $2\pi$
$i$	Imaginary unit, $\sqrt{-1}$
$\alpha$	Absorption coefficient
$\alpha_{\text{Total}}$	Total absorption of a structure
$\alpha_j$	Absorption of the $j^{\text{th}}$ quantum well
$\alpha_{x/y}^{\text{on/off}}$	Absorption coefficient of a x or y polarized component of light in the on/off state of a switch
$\alpha_{x/y}$	Absorption coefficient for x and y polarized light
$\alpha_{+/-}^{\text{pump/no pump}}$	Absorption coefficient for right (+) and left (-) circularly polarized light with and without the pump present
$\Delta\alpha$	Difference in absorption coefficient for right and left circular polarized light, $\delta\alpha_+ - \delta\alpha_-$
$\Delta\alpha_{x/y}$	Change in absorption coefficient for x and y polarized light during switching, $\alpha_{x/y}^{\text{on}} - \alpha_{x/y}^{\text{off}}$
$\delta\alpha_{+/-}$	Difference in absorption coefficient for right (+) and left (-) circularly polarized light with and without the pump present, $\alpha_{+/-}^{\text{pump}} - \alpha_{+/-}^{\text{no pump}}$
$\beta$	Resonant component included in transfer matrix
$\epsilon_0$	Dielectric constant
$\epsilon$	Ellipticity angle
$\epsilon^{\text{on/off}}$	Ellipticity of light in the on/off state of a switch
$\Phi$	Wave function for a particle
$\phi_{a,b}$	Wave function for a particle in the a or b state
$\tilde{\phi}(\vec{r})$	Wave function for an exciton with electron/hole wavefunction separation given by $\vec{r}$

$ \phi_{a,b}\rangle$	State vector for a particle in state a or b
$\gamma$	Polarization non-radiative dephasing rate
$\gamma_0$	Linear (in carrier density) component of the non-radiative polarization dephasing rate
$\Gamma$	Radiative decay rate of an excited electron
$\lambda$	Wavelength of light
$\lambda_B$	Wavelength of Bragg-resonance
$\lambda_{\text{ASFP}}$	Design wavelength of an ASFP
$\mu$	Effective mass of a system
$\mu_0$	Permeability of free space
$\langle\mu\rangle$	Expectation value of the dipole moment
$\eta$	Extinction ratio of a polarizer
$\rho$	Density matrix
$\rho^{(n)}$	$n^{\text{th}}$ order component of the density matrix
$\rho_{\text{free}}$	Free charges in a material
$\rho_{ij}$	Element at the $i^{\text{th}}$ row and $j^{\text{th}}$ column of the density matrix
$\sigma+$	Right-circularly polarized light
$\hat{\sigma}+$	Right-circular unit vector, $\hat{x} - i\hat{y}$
$\sigma-$	Left-circularly polarized light
$\hat{\sigma}-$	Left-circular unit vector, $\hat{x} + i\hat{y}$
$\tau$	Pump-probe (signal-control) time delay
$\tau_{\text{delay}}$	Time delay of a pulse
$\tau_{\text{bit}}$	Time delay of a pulse in units of bitwidth
$\theta_{\text{sig}}$	Orientation of an ellipse
$\theta_{\text{sig}}^{\text{on/off}}$	Orientation of transmitted/reflected light in the on/off state of a switch
$\chi$	Susceptibility

$\chi_B$	Background susceptibility
$\chi^{(n)}$	$n^{\text{th}}$ order susceptibility
$\chi^{(3)}$	Third order susceptibility
$\omega_{ba}$	Frequency difference between levels a and b
$\omega_i$	Frequency of pulse $i$ . $i$ in the text includes 1 and 2 (pulse 1 or pulse 2), S (signal pulse), C (control pulse), and pump/probe (pump and probe pulses)
$\omega_B$	Bragg-resonance of a material in frequency space
$\omega_0$	Center frequency of an electro-magnetic pulse
$\Delta\omega$	Detuning between $\omega_B$ and $\omega_X$
$\Delta\omega_{\text{IB}}$	Width of the intermediate band
$\xi$	Local field parameter
$A$	Fraction of incident fluence absorbed by a material
$A_{\text{probe}}$	$1 - R_{\text{probe}} - T_{\text{probe}}$
$\mathcal{A}$	Amplitude of the field
$a$	Inter-well spacing
$a$	Major axis of an ellipse
$b$	Minor axis of an ellipse
AR	Anti-reflection
AlGaAs	Aluminum Gallium Arsenide
ASFP	Asymmetric Fabry-Perot etalon
$\vec{B}$	Applied magnetic field
BBO	$\beta$ -barium borate
BSQW	Bragg-spaced quantum wells
$c$	Speed of light
$c_{+,-}$	Coefficient of polariton eigenvectors
$c_{a,b}$	Probability of being in state a or b
CR	Contrast ratio

$CR_{dB}$	Contrast ratio in decibels
$CR_{T/R}$	Contrast ratio of a transmission (T) or reflection (R) switch
$\vec{D}$	Displacement field
$d$	Width of an ASFP cavity
DCT	Dynamics controlled truncation scheme
$\vec{E}$	Electric field
$\vec{E}_{LF}$	Local field generated by aligned dipoles excited in a material
$\vec{E}_j^{+-}$	Electric field traveling to the left (+) or right (-) at the right edge of the $j^{\text{th}}$ layer
$\vec{E}_{\text{probe}}$	Probe electric field
$\vec{E}_{\text{pump}}$	Pump electric field
$\vec{\mathcal{E}}(t)$	Envelope function of an electronic field
$\vec{\mathcal{E}}_0$	Incident field envelope function
$\vec{E}_T$	Electric field transmitted through a material
$E_c^m$	$m^{\text{th}}$ confinement energy of electrons in a well layer
$E_g$	Energy gap between the hh- and conduction-band in a direct-bandgap III-V material at its $\Gamma$ point
$E_{hh}$	Energy at the peak of the hh-band
$E_j^\pm$	Electric field propagating through the $j^{\text{th}}$ layer of a material. $\pm$ denotes direction of travel. + waves travel to the left, - to the right
$E_X^n$	Energy of $n^{\text{th}}$ exciton level
$E_b$	Binding energy of the exciton
$E_B$	Fundamental bandgap in barrier layers
$E_W$	Fundamental bandgap in well layers
$E_{3D,x}^n$	Confinement energy of electron or hole in a well layer. Particle is in the $n^{\text{th}}$ energetic state ( $n$ is integers $> 0$ ) of the $x^{\text{th}}$ band (i.e. light-hole, heavy-hole, etc)

$\mathcal{E}_S$	Signal field envelope function
$\mathcal{E}_C$	Control field envelope function
EID	Excitation induced dephasing
eV	Electron-volts
FWHM	Full-width at half-maximum
FWM	Four-wave-mixing direction
GaAs	Gallium Arsenide
$\vec{H}$	Magnetizing field
$H$	Hamiltonian
$H_{0,aa/bb}$	Atomic Hamiltonian
$H_{\text{int}}$	Interaction Hamiltonian
$H_{\text{Coul}}$	Coulomb Hamiltonian
hh	Heavy-hole
$I$	Intensity of an electric field
$I_T$	Intensity of the field transmitted through a material
$I_R$	Intensity measured in the reflected probe direction
$I_0$	Incident intensity from probe direction
$I_X$	Intensity of the x-polarized component of a field
$I_Y$	Intensity of the y-polarized component of a field
$I_{45}$	Intensity of the component of a field polarized $45^\circ$ from the x-axis
$I_{-45}$	Intensity of the component of a field polarized $-45^\circ$ from the x-axis
$I_{\sigma+}$	Intensity of the right circular polarized component of a field
$I_{\sigma-}$	Intensity of the left circular polarized component of a field
IB	Intermediate band
$\text{In}_x\text{Ga}_{1-x}\text{As}$	Indium Gallium Arsenide containing $x\%$ Indium

InGaAsP	Indium Gallium Arsenide Phosphide
InGaAs(P)	Indium Gallium Arsenide Phosphide
$J$	Angular momentum of a particle
$J_z$	z-component of a particle's angular momentum
$\vec{J}$	Currents inside a medium
$J_{\text{pol}}^y$	Jones matrix for a polarizer aligned on the y-axis
$K$	Total wavevector of a system
$\vec{k}_{1,2}$	Wavevector of pulse 1 or 2
$\vec{k}_e$	Electron wavevector
$\vec{k}_h$	Hole wavevector
$k_{\text{probe}}$	Probe wavevector
$k_{\text{pump}}$	Pump wavevector
$k_{xyz}$	x, y, or z component of a particle's wavevector
$l_{\text{Design}}$	Design thickness of an anti-reflection coating
$l_W$	Width of a quantum well layer
$l_j$	Width of the $j^{\text{th}}$ quantum well layer
$l_{\text{Total}}$	Sum of all quantum well layer widths in a structure
$L_{\text{LF}}$	Local field constant
lh	Light-hole
$M$	Total mass of a system
$m_e^*$	Electron effective mass
$m_h^*$	Hole effective mass
$\mathcal{M}$	Total transfer matrix for a system
$\mathcal{M}_j$	Transfer matrix for the $j^{\text{th}}$ layer of a system
$m_{ij}$	Element at the $i^{\text{th}}$ row, and $j^{\text{th}}$ column of a transfer matrix
MBE	Molecular beam epitaxy

meV	mili Electron-volts
ml	monolayer
MQW	Multiple quantum wells
$N$	Number of wells in a MQW system
$N_e$	Exciton density
$n$	Quantum number of the exciton
$n_{\text{air}}$	Refractive index of air
$n_{\text{glass}}$	Refractive index of glass
$n_b$	Background refractive index of a meta-material
$n_j$	Complex index of refraction of the $j^{\text{th}}$ layer of a material
$n_0$	Linear refractive index of a material
$n_2$	Second order change to the refractive index of a material
$n_g$	Group index of an electro-magnetic pulse
$n_{\text{NL}}$	Nonlinear component of refractive index of a material
$n_{\text{eff}}$	Effective index of a metamaterial
$n_{+/-}^{\text{pump/no pump}}$	Index of refraction for right (+) and left (-) circularly polarized light with and without the pump present
$\Delta n$	Difference between index of refraction change for right and left circularly polarized light, $\delta n_+ - \delta n_-$
$\delta n_{+/-}$	Difference in index of refraction for right (+) and left (-) circularly polarized light with and without the pump present, $n_{+/-}^{\text{pump}} - n_{+/-}^{\text{no pump}}$
$P$	Polarization in a material
$P$	Degree of polarization of an electromagnetic field
$P_B$	Background polarization of a material
$P_{\text{res}}$	Resonant component of the polarization in a material
$p_j$	Polarization of the $j^{\text{th}}$ well

$q$	Photon wavevector outside a material
$q_e$	Fundamental charge
QCSE	Quantum confined Stark effect
$r$	Reflection coefficient of a structure
$r_N$	Reflection coefficient from a BSQW structure with N wells
$R^*$	Rydberg for exciton binding energy
R	Percent of incident fluence reflected from a surface
$R_b$	Percent of incident fluence reflected from the back surface of an ASFP
$R_f$	Percent of incident fluence reflected from the front surface of an ASFP
$R^{\text{on}}$	Fraction of incident fluence reflected in a switches on-state
$R^{\text{off}}$	Fraction of incident fluence reflected in a switches off-state
$R_{\text{Goal}}$	Goal reflectance for an AR coating
$R_{\text{probe}}$	Reflected light traveling in the probe direction
$R_{\text{pump}}$	Reflected light traveling in the pump direction
$\Delta R_{\text{probe}}$	Change in the temporally and spectrally integrated signal in the probe's reflected direction, $R_{\text{probe}}^{\text{on}} - R_{\text{probe}}^{\text{off}}$
$\Delta R$	Change in the temporally integrated (spectrally resolved) reflection, $R^{\text{on}} - R^{\text{off}}$
RHEED	Reflection high-energy electron diffraction
RPBG	Resonant photonic bandgap
$S_0, S_1, S_2, S_3$	Stokes parameters
so	Split-off
$\Delta S$	Change in total intensity traveling in both reflected and transmitted probe directions, $\Delta R_{\text{probe}} + \Delta T_{\text{probe}}$

$T$	Fraction of incident fluence transmitted through a material
$T^{\text{on,off}}$	Fraction of incident fluence transmitted in a switches on- or off-state
$[\ ]^T$	Transpose of a matrix
$T_{\text{probe}}$	Reflected light traveling in the probe direction
$T_{\text{pump}}$	Reflected light traveling in the probe direction
$\Delta T_{\text{probe}}$	Change in the temporally and spectrally integrated signal in the probe's transmitted direction, $T_{\text{probe}}^{\text{on}} - T_{\text{probe}}^{\text{off}}$
$\Delta T$	Change in the temporally integrated (spectrally resolved) transmission, $T^{\text{on}} - T^{\text{off}}$
Ti:Sapphire	Titanium sapphire
TP	Throughput
$TP_{\text{dB}}$	Throughput in decibels
$TP_{\text{T/R}}^{\text{on/off}}$	Throughput of the on/off state of a transmission (T) or reflection (R) switch
$\delta t$	Temporal width of a pulse
$u_{+,-}$	Component of the $W_{+,-}$ eigenvector
$v_{+,-}$	Component of the $W_{+,-}$ eigenvector
$v_g$	Group velocity of an electro-magnetic pulse
$W_{+,-}$	Eigenvectors of the transfer matrix
$\hat{x}$	Unit vector in the x-direction
$\hat{y}$	Unit vector in the y-direction
ZnSe	Zinc Selenide

## CHAPTER 1 INTRODUCTION

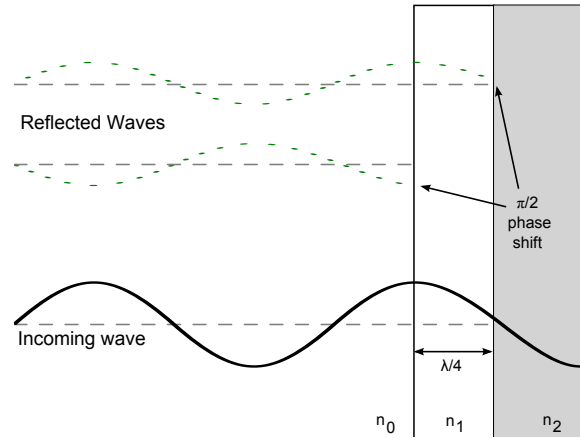


Figure 1.1: Schematic of a 1 layer anti-reflection coating. Reflections from the two interfaces interfere destructively, and the net reflection is decreased. Note that this only shows the first order reflections from the surfaces.

Photonic materials first attracted attention in the late 1800's [5] when researchers noticed that the thin coatings formed on lenses affected their reflective and transmissive properties [6]. It was quickly determined that the changes in reflection were due to constructive and destructive interference between waves reflecting off the front and back interfaces of the film (see a simplified model in Fig. 1.1). When the optical path length of the film is such that the reflected waves are exactly  $\pi/2$  out of phase, the net reflected light is zero. The idea was quickly put to use, and by the early 1900's [7] both fabricated and natural anti-reflection coatings were being used and encouraged in telescopes and other optical devices.

Fabricated films were initially created by a chemical etching process [8, 9] where material was etched away until only a small amount was left on the substrate. During WWII the need for better quality, more reproducible coatings to be used in gun sights and other military apparatus grew. A gun sight with 40%

more light passing through it could allow a soldier to use it for an extra 30-45 minutes at both dawn and dusk. To improve the quality of the films made and to allow more complex multilayered structures, vacuum deposition techniques were developed where a heated material would be evaporated and deposited directly onto the surface of a substrate [10, 11]. These techniques became the precursors to modern techniques such as molecular beam epitaxy (MBE), chemical vapor deposition, and sputtering techniques [12].

Along with the enhanced technology for creating films, research in new types of films also grew. This included better anti-reflection coatings capable of removing almost all reflection over a wide range of wavelengths [9], and films which enhance the reflectivity of a material (dielectric mirrors). Such dielectric mirrors can have very high reflectivity (99.999%), and have proven useful in many applications. For instance, dielectric mirrors are used almost exclusively in laser cavities where the high tunability (both in terms of total fraction reflected and in terms of the bandwidth) allows for optimization of the losses in the cavity. They can also be fabricated along with the resonant materials to form things such as small vertical-cavity surface-emitting lasers [13].

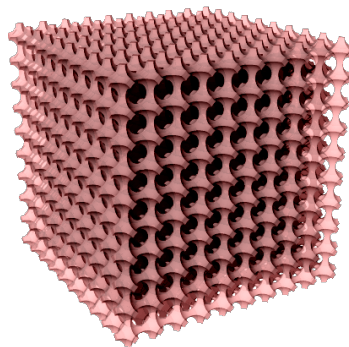


Figure 1.2: Schematic of a 3D photonic crystal. The periodicity in this case extends in three dimensions rather than one.

Since their discovery, photonic materials have been noted in many areas of

biology [14, 15] including butterfly wings [16] and peacock feathers [17]. Some of these structures are capable of changing the way light interacts with them from all directions (see Fig. 1.2). While these 2D and 3D photonic crystals differ from 1D thin film coatings, the principles of their operation remain the same. Light encounters periodic structures in all directions, and the interference between waves causes the structures to reflect or transmit light differently than the individual components normally would.

Artificially produced 2D and 3D photonic crystals<sup>1</sup> first gained attention in the late 1980's when Yablonovich [19] and John [20] proposed that the lack of photonic modes in such a crystal could prohibit spontaneous emission in all directions. In devices such as laser cavities, this could significantly reduce losses from a system. This drove interest in photonic crystals, and still today there is a lot of research in both generic photonic *materials*, and in 2D and 3D photonic *crystals* [21].

Along with this came an interest in the *resonant* photonic materials discussed here. Resonant photonic materials may be constructed similarly to the dielectric mirrors or anti-reflection coatings talked about earlier, and give rise to similar reflection spectrum, but contain a resonance in the system near the same frequency as the index variation (see Fig. 1.3). Periodic micro-ring cavities [22] and the multiple quantum well structures discussed here have both been used to produce resonant photonic materials. The ability to use them to control the propagation of light promises to provide exciting new capabilities in areas of communications and optics.

---

<sup>1</sup>There has been some debate about what qualifies a structure as a “photonic crystal”. For the most part this label is only appropriate for 2D or 3D structures where the word crystal is more apt, and where the index contrast between materials in the structure is large [18].

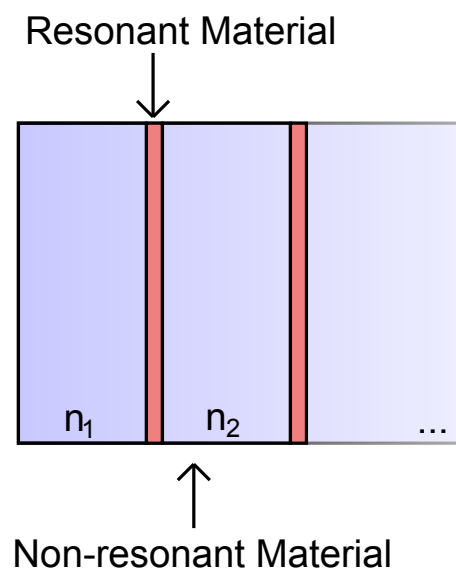


Figure 1.3: Schematic of an resonant photonic material. Rather than varying just the index of the materials, materials with a resonance at the same frequency as the periodicity are used.

## CHAPTER 2 BACKGROUND

This research focuses on resonant photonic materials composed of a large number of periodically spaced quantum wells in III-V semiconductor material, also known as Bragg-spaced quantum wells (BSQWs). In order to establish a language and background for talking about BSQWs, it is important to begin by describing quantum wells and the semiconductor materials used to compose them.

### 2.1 Basics of semiconductor materials

*III-V* semiconductors are materials composed of elements from group 13 and group 15 of the periodic table. Only the eight outer level electrons (three from the anion and five from the cation) contribute to the chemical bonds in the structure. The rest are tightly bound to the nucleus. Two of the electrons form deeply bound s-bands which are always occupied, while the remaining six form bound p-like orbitals [23].

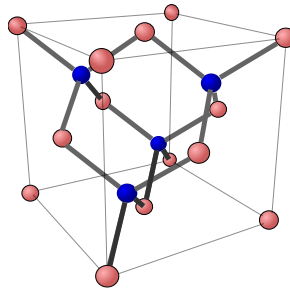


Figure 2.1: Schematic of *III-V* semiconductor unit cell. The cell consists of two face-centered cubic lattices displaced by one fourth of one of the cube's main diagonals.

When crystallized, these materials form a zinc-blend structure, consisting of two face-centered cubic lattices, displaced by one fourth of one of the cube's main

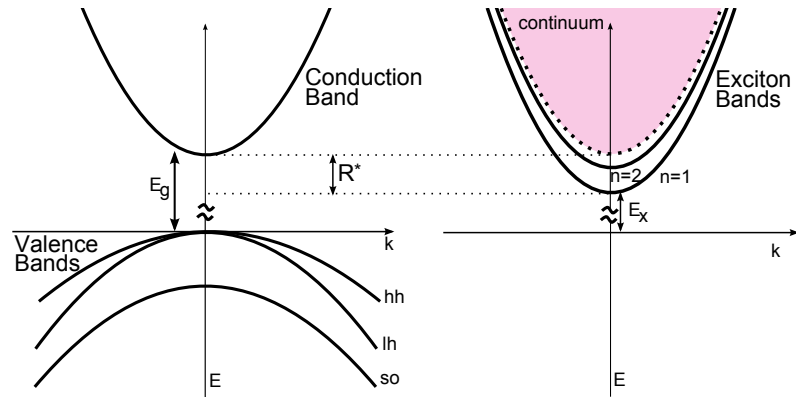


Figure 2.2: On the left is a schematic electronic band structure for a *III-V* semiconductor. This is an one particle picture showing allowed levels for electrons in the *hh*, *lh*, and *so* valence bands, as well as the lowest lying conduction band. On the right is the two particle, excitonic band structure. Since excitons do not exist until a particle has been excited, there is no “ground” state.

diagonals (see Fig. 2.1). Because the structures are periodic, the *energy levels* of the molecules expand to form *energy bands* in the structure. At 0K the conduction band is defined as the lowest energy band containing no electrons, and the valence bands as those completely filled in insulators and semiconductors or partially filled in metals. In some semiconductors such as GaAs, a direct bandgap forms where the top of the valence band and the bottom of the lowest lying conduction band occur at the same symmetry point, known as the  $\Gamma$ -point of the Brillouin zone (see left in Fig. 2.2). Two of the binding orbitals are split off due to spin orbit coupling, and are known as the split off (*so*) bands. The other four electrons lie in the light hole (*lh*) and heavy hole (*hh*) bands, which are degenerate at the  $\Gamma$ -point.

A schematic figure of the band structure in a parabolic approximation is shown on the left in Fig. 2.2 where the peak of the *hh*-band has been designated as  $E_{hh} = 0$ , and the energetic difference between this peak and lowest conduction band energy has been designated  $E_g$ , the energy bandgap. The *lh*- and *so*-bands are also shown.

When an electron is excited into the conduction band, the Coulomb interaction between it and the hole (absence of charge) left in the valence band can result in the formation of a bound state. The resulting quasi-particle is referred to as an exciton. For situations where the electron and hole are tightly bound to a particular lattice site or unit cell (for instance in ionic crystals), the binding is strong and the exciton is typically small and confined to a single lattice site. However, in semiconductors electron and hole may be at different lattice sites and the attraction screened by valence electrons at nearest neighbor cells. In these cases the bond is weaker and the excitons (known as Wannier-Mott excitons) are often much larger and can move in the structure [24, 25].

The interaction between the two particles can be written in terms of the center-of-mass coordinates of both the electron and hole, and reduces into two parts. One part resembles a free particle with mass  $M = m_e^* + m_h^*$  (where  $m_e^*$  and  $m_h^*$  are the effective masses of both the electron and hole respectively) and wave vector  $K = k_e + k_h$ . The second is a relative-motion term resembling a Hydrogen atom and labeled by three quantum numbers,  $nml$ . Assuming the effective mass of the quasi-particle is isotropic, only the  $n$  quantum number is important to the total energy of the exciton which can then be approximated:

$$E_X^n = E_g + \frac{\hbar^2 K^2}{2M} - \frac{\mu q_e^4}{2\hbar^2 \epsilon_0^2 n^2} \quad (2.1)$$

where  $1/\mu = 1/m_e^* + 1/m_h^*$  is the effective mass of the system,  $q_e$  is the fundamental charge,  $\hbar$  is Plank's constant, and  $\epsilon_0$  is the permittivity of free space [24, 26], and  $n$  is an integer number the excitonic energy bands. The band structure of the exciton in this model appears as a series of parabolas centered below the electronic bandgap by a distance  $E_b = \frac{R^*}{n^2}$  where  $R^* = \frac{\mu q_e^4}{2\hbar^2 \epsilon_0^2}$ . Because these are two particle states they are shown separately (on the right) from the one particle band structure (on the left) in Fig. 2.2. For semiconductors such as GaAs, this binding energy can be significant ( $\approx 5$  meV).

## 2.2 Fabrication of layered semiconductor structures

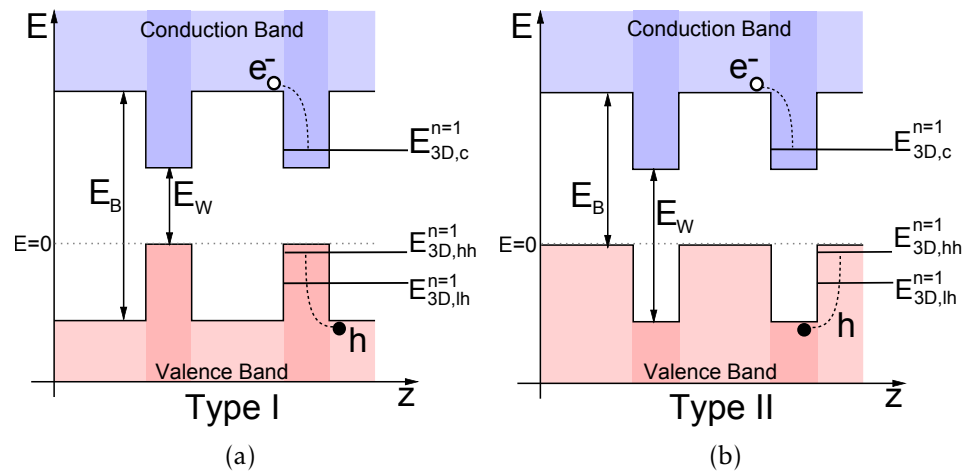


Figure 2.3: Schematic of quantum well band structure versus position in the  $z$ -direction. Conduction band energies and valence band energies are shown. (a) represents type-I quantum wells. (b) represents type-II quantum wells.  $E_B$  and  $E_W$  represent the bandgap of the semiconductor materials inside the barrier and well layers respectively.

Semiconductor structures have been fabricated by layering materials with different electronic bandgaps, resulting in a bandgap that changes as a function of the perpendicular direction to the layers (referred to here as the  $z$ -direction, see Fig. 2.3).

One technique used to create these structures is molecular beam epitaxy (MBE). This type of semiconductor fabrication involves evaporating or sublimating materials and allowing them to attach to the surface of a substrate. This process is kept slow (approximately 0.5 monolayers (ml) of material are grown per second) to maintain good precision in the growth rate ( $\approx 1$  ml precision). Because this is a slow process and the distances required for materials to travel are often large, it is performed under high vacuum ( $\approx 10^{-10}$  torr) in order to inhibit the attachment of impurities and to provide a longer mean free path for the materials (i.e. typically over long distances many scattering events would occur. At high

vacuum, the mean-free path of particles increases and scattering events become less common).

### 2.3 Quantum well basics

Quantum well materials are a subset of layered semiconductor materials. In quantum wells, thin well layers with some bandgap ( $E_W$ ) are placed between thicker barrier layers with a different bandgap ( $E_B$ ). Two main types of quantum wells are shown in Fig. 2.3. Type-I wells (shown in Fig. 2.3(a)) require that 1.) the conduction band of the well material extends below the conduction band of the barrier material, and 2.) the valence band of the well extends above that of the barrier. In type-II wells [shown in Fig. 2.3(b)] only one of these conditions is met.

Electrons (and holes) inside these wells are effectively confined in the  $z$ -direction. This confinement changes their energy, and as such they display yet another subset of energy levels. The simple case of infinitely high barriers ( $E_B = \infty$ ) has been presented in detail many times [23, 27], but the primary results are reviewed here. For electrons in the conduction band, an infinite number of subbands appear. The altered energy of electrons in these subbands can be written:

$$E_{2D,c}^m = E_W + \frac{\hbar^2(k_x^2 + k_y^2)}{2m_e^*} + E_c^m \quad (2.2)$$

where  $E_W$  is the bandgap of the well,  $m_e^*$  is the effective mass of the conduction band electrons, and  $E_c^m$  represents the  $m^{\text{th}}$  energy level of the electrons due to their confinement, and is given by known energy levels for particles in an infinite well:

$$E_c^m = \frac{\hbar^2 \pi^2}{2m_e^* l_W^2} m^2 \quad (2.3)$$

where  $l_W$  is the width of the well, and  $m$  denotes integers greater than zero.

Similarly the  $hh$  and  $lh$  valence bands are also split, although an accurate picture of the two at  $k_x$  and  $k_y \neq 0$  requires a more advanced formalism [28] due to mixing between the two bands. However, since excitons are unlikely to form at larger  $k$  values, it is sufficient here to note that at  $k_x = k_y = 0$ , the bands are lowered

by amounts:

$$E_{2D, hh}^m = \frac{-\hbar^2 \pi^2}{2m_{hh}^* l_W^2} m^2 \quad (2.4)$$

$$E_{2D, lh}^m = \frac{-\hbar^2 \pi^2}{2m_{lh}^* l_W^2} m^2 \quad (2.5)$$

Due to the difference in effective masses of the  $hh$  and  $lh$  valence bands, confinement in the  $z$ -direction has removed the degeneracy between the two. When quantum wells with finite barrier heights are considered, the situation changes slightly as evanescent waves from the particles are allowed to penetrate into the barriers, and there is a cap on the number of energy levels present in the well material before the top of the barrier is reached. Exact solutions of this situation are not possible, although they can be found numerically.

The confinement of electrons and holes within the quantum well increases the overlap between electron and hole wave functions by forcing the two into the same plane. As a result, the Coulomb interaction between the two is enhanced [28]. This has profound effects on the binding strength of the exciton, and as such on both the absorption and reflection from such quantum wells. The resulting exciton resonance is often visible even at room temperature [27, 29].

In addition to the many splittings and shifts of energies that have been discussed so far, electrons (and excitons) observe strict selection rules for optical transitions between the structure's energy levels [27]. These can be summarized by looking at the angular momentum changes between the  $hh$  ( $J = \frac{3}{2}, J_z = \pm\frac{3}{2}$ ) and  $lh$  ( $J = \frac{3}{2}, J_z = \pm\frac{1}{2}$ ) states, and excited conduction band states ( $J = \frac{1}{2}$  and  $J_z = \pm\frac{1}{2}$ ). Here  $J$  is the total angular momentum of the electron, and  $J_z$  represents the projection of the angular momentum onto the  $z$ -axis (where units of  $\hbar$  have been left out for convenience). Circularly polarized light (with angular momentum  $\pm 1$ ) can only excite transitions which satisfy angular momentum conservation. For instance, circularly polarized light with angular momentum  $-1$  can excite a transition from the  $+\frac{3}{2} hh$  to the  $+\frac{1}{2}$  conduction band but not a transition from the  $+\frac{3}{2} hh$  to the  $-\frac{1}{2}$

conduction band. The selection rules for the  $hh$  and  $lh$  levels are summarized in Fig. 2.4. Also shown are many body effects which can couple the two resonances, and are discussed in more detail in Sec. 2.4.

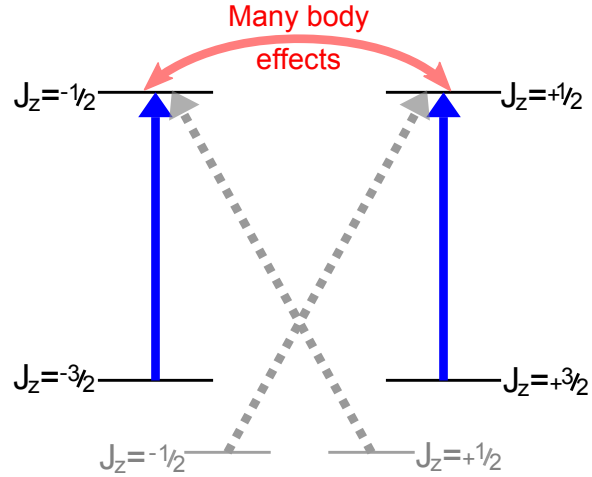


Figure 2.4: Optical selection rules coupling left ( $\sigma+$ ) and right ( $\sigma-$ ) circularly polarized light between the  $hh$  and  $lh$  valence band electrons and excited conduction band electrons. Many body effects which can allow the two systems to interact are indicated in red.

Finally, multiple quantum well (MQW) structures have also been constructed that are composed of more than one quantum well stacked together (as shown previously in Fig. 2.3). In a simple model, the effect of stacking wells is additive. Electrons in each well absorb a small amount of light creating a total absorption,  $\alpha_{\text{Total}} l_{\text{Total}} = \sum_j \alpha_j l_j$  where  $\alpha_j$  ( $l_j$ ) is the absorption (width) of the  $j^{\text{th}}$  well and  $l_{\text{Total}}$  the combined width of all the wells. In real situations reflections at the interfaces, as well as slight differences between adjacent wells and surface roughness along the walls of the well can lead to changes in the exact line shape.

A unique structure, known as a super-lattice, occurs when the barriers are thin and the bandgap difference between barriers and wells are small enough for the wave functions of the electrons and holes to extend significantly into the adjacent wells. In this case the usual discrete energy levels of the wells broaden

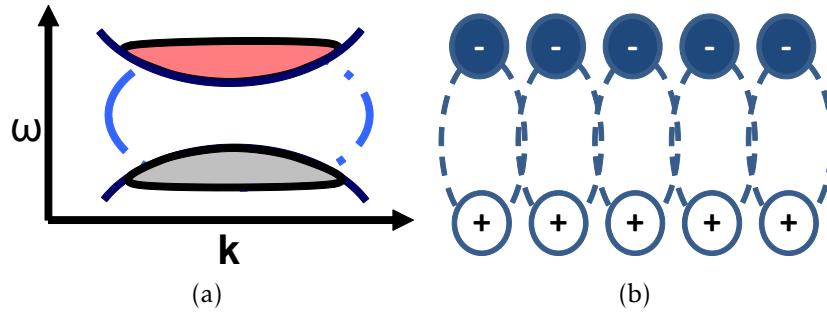


Figure 2.5: Schematic of Pauli-blocking (a) and Hartree-Fock (b) effects.

into mini-bands.

#### 2.4 Nonlinear effects in semiconductor quantum wells

The nonlinear response of MQW materials has been described in several different models including a few-level system [30], "microscopic" models in which the semiconductor dynamics are modeled in terms of individual interacting electrons and holes [31], and bosonic models where the exciton interactions are modeled via a bosonic Hamiltonian [32]. A brief review of a few-level model (using only 2-levels) is given in Appendix A.4. The nonlinearities appearing in these models can be separated into a few distinct effects. In particular, some of these effects can couple excitons of different spin, as shown in red in Fig. 2.4, while others will only affect systems having the same spin. In the limit that effects coupling spin systems, and higher lying transitions such as the lh-conduction band transition, can be ignored, the four-level system shown in Fig. 2.4 reduces to two, uncoupled, two-level systems. Using these two weakly coupled systems to induce circular dichroisms and circular anisotropies to construct a polarization switch is one of the main subjects of this research detailed in Sec. 3.1.

The many body effects of interest here can be separated into a few categories, including:

**Pauli-blocking** effects [Fig. 2.5(a)] prohibit two electrons from inhabiting the

same state simultaneously. Since electrons of opposite spin won't occupy the same states, Pauli-blocking effects will not couple the two spin systems shown in Fig. 2.4.

**Hartree-Fock** effects, also known as local field corrections [Fig. 2.5(b)], arise due to fields created by arrays of aligned dipoles inside the system. Because these fields have the same polarization as the exciting fields, they will not couple the separate spin systems. In a simple two-level system model, Hartree-Fock effects can be included via an ad hoc method where a new field is introduced inside the material, such that [33, 30]:

$$\vec{E}(\omega) \rightarrow \vec{E}(\omega) + \vec{E}_{\text{LF}}(\omega) = \vec{E}(\omega) + L_{\text{LF}}\vec{P} \quad (2.6)$$

where  $\vec{E}_{\text{LF}}(\omega)$  denotes the local field created inside the structure by the dipoles,  $L_{\text{LF}}$  is a constant known as the local field parameter, and  $\vec{P}$  is the polarization of the material.

**Excitation induced dephasing** (EID) is brought about by exciton-exciton collisions, and only depends on the total density of particles, not their spin. As such, it can couple spin-up and spin-down systems. EID can be inserted into a few-level model phenomenologically by expanding the dephasing rate of the polarization ( $\gamma$ ) in a power series in carrier density, such that:

$$\gamma(N_e) = \gamma_0 + N_e \frac{\partial \gamma}{\partial N_e} + \dots \approx \gamma_0 + N_T(\rho_{bb} - \rho_{aa}) \frac{\partial \gamma}{\partial N_e} \quad (2.7)$$

where  $N_e = N_T(\rho_{bb} - \rho_{aa})$  is the total exciton density,  $N_T$  is the total number of excited oscillators,  $\rho_{bb/aa}$  are the diagonal-density matrix elements, giving the probability of a particle being in state  $a$  or  $b$ , and  $\gamma_0$  is the initial dephasing rate of the system.

**Biexciton effects** include both exciton exciton scattering [see Fig. 2.6(b)] and bound biexcitons [see Fig. 2.6(a)]. Excitons of opposite spin can form bound biexcitons, while scattering states are independent of spin. As such these

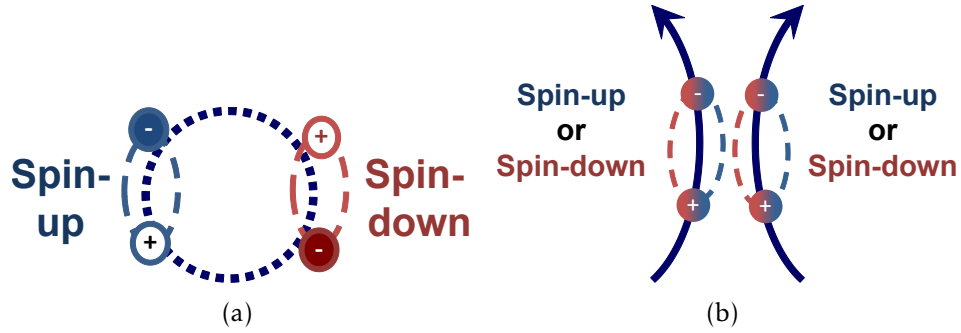


Figure 2.6: Schematic of bound (a) and unbound (b) biexciton states.

effects can couple both spin-systems. Biexciton effects are included in a few-level model through inclusion of additional levels in the system (beyond the simple two-level system described in Appendix A.4). For an example, see Ref. [30].

In the absence of these later two effects (biexciton effects or EID), and if higher lying transitions like the light hole can be ignored, the two independent two-level system model is accurate.

These many body effects influence the absorption and index of the materials, and depend nonlinearly on the incident light fields. When the multiple fields are incident on the material, the interference of fields inside the structure can give rise to *gratings* in index and absorption inside the material, known as four-wave-mixing effects. To briefly look at these four-wave-mixing effects, it is helpful to write the field incident on the material as:

$$E = E_1 e^{i(\omega_1 t - k_1 z)} + c.c. + E_2 e^{i(\omega_2 t - k_2 z)} + c.c. \quad (2.8)$$

where  $E_{1,2}$  is the amplitude of field one or two respectively, traveling with wavevector  $k_{1,2}$  and frequency  $\omega_{1,2}$ , and  $c.c$  is the complex conjugate of the

preceding term. The intensity of the field,  $I$ , then has the form

$$\begin{aligned}
I \propto |E|^2 &= |E_1|^2 + |E_2|^2 + |E_1^*|^2 + |E_2^*|^2 \\
&+ E_1 E_1^* e^{i[2\omega_1 t - 2k_1 z]} + c.c. \\
&+ E_2 E_2^* e^{i[2\omega_2 t - 2k_2 z]} + c.c. \\
&+ E_1 E_2^* e^{i[(\omega_1 - \omega_2)t - (k_1 - k_2)z]} + c.c. \\
&+ E_1 E_2 e^{i[(\omega_1 + \omega_2)t - (k_1 + k_2)z]} + c.c.
\end{aligned} \tag{2.9}$$

To incorporate this into Maxwell's equations, it is useful to write the complex *nonlinear* index of refraction,  $n$ , such that  $n \rightarrow n_0 + n_{\text{NL}}$ , where  $n_0$  is the linear component, and  $n_{\text{NL}}$  the nonlinear component.  $n_{\text{NL}}$  may arise from the terms described above such as Hartree-Fock effects of Pauli-blocking. Approximating  $n_{\text{NL}}$  as  $n_{\text{NL}} = n_2 I$ , intensity gratings in the material lead to gratings in refractive index and absorption:

$$n = n_0 + n_2 (E_1(z, t) E_2^*(z, t) e^{i[(\omega_1 - \omega_2)t - (k_1 - k_2)z]} + \dots) \tag{2.10}$$

In  $\chi^{(3)}$  processes, a field can scatter off this grating sending energy in new directions, or the grating can introduce a phase shift, redistributing energy within a pulse.

## 2.5 Fabrication of Bragg-spaced quantum wells

BSQWs are MQW structures in which a periodic spacing has been introduced such that the inter-well spacing,  $a \approx c\pi/n_b\omega_B = \lambda_B/2n_b$  (see Fig. 2.7), where  $c$  is the speed of light in a vacuum,  $n_b$  is the background index of refraction in the material and  $\omega_B$  (in wavelength space,  $\lambda_B$ ) is the Bragg frequency which describes the periodicity of the wells. In the Bragg reflectors or anti-reflection coatings discussed earlier the index contrast between the bulk materials is responsible for the photonic band structure. By contrast, in BSQWs the index contrast is brought about by the presence of the  $hh$ -exciton in the quantum wells. The photonic band structure of the material is due to the periodic array of exciton resonances, and as such, changes to the resonance change the fundamental photonic structure of the

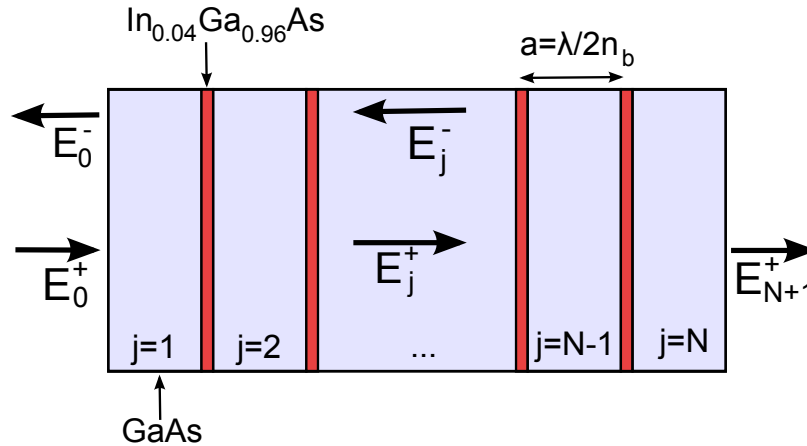


Figure 2.7: Schematic of a BSQWs. The light shaded (blue) areas represent barriers made of GaAs, and the dark shaded (red) ones  $\text{In}_{0.04}\text{Ga}_{0.96}\text{As}$  layers. The spacing between the wells,  $a$ , determines the Bragg resonance,  $\omega_B$ . Electric fields used in calculating the transfer matrix (see Section 2.6) between individual layers are also shown.

material.

Fabricating BSQWs using MBE presents several unique difficulties. First, the structures are extremely sensitive to detuning of the exciton resonance ( $\omega_X$ ) from the Bragg resonance ( $\omega_B$ ) [34]. As an example, in the InGaAs quantum wells being discussed here, a distortion in barrier width of only 0.5% (enough to distort the photonic band structure significantly) corresponds to two monolayers of the 1060Å wide barriers. While MBE can be precise (the degree to which a particular layer thickness can be repeated) to a single monolayer, the accuracy (difference from the desired layer thickness) can deviate by a few percent. This can be due to deviations in growth rates over time, strain which can cause a particular monolayer to have a different width than expected, and other factors.

To account for this lack of accuracy, it is simplest to introduce some tunability into the structure so that it can be adjusted to meet Bragg periodicity ( $\omega_B = \omega_X$ ). Two techniques for introducing this are temperature tuning and growth of wedged structures. Exciton energies shift with temperature because the fundamental

bandgaps of semiconductors change with temperature. These changes come about mostly through electron-phonon interactions which can have profound effects on the bonding of electrons between different lattice sites [35]. Temperature tuning of the quantum well resonance involves the creation of more phonons in the structures, and as such it is not always desirable.

In contrast, wedged structures provide tunability by varying the amount of material deposited across the surface of the structure. This can be accomplished by holding the substrate material stationary during growth. Substrates are usually rotated during growth to even out variations in material flux on the substrate. By not rotating, barrier and well widths can differ across the surface of the sample by as much as 10%, resulting in a slight wedge [34]. While both the well materials and barrier materials will experience some difference in thickness, the Bragg resonance depends on the thickness of the barrier to first order. By contrast, the majority of the exciton energy comes from the bandgap of the well material ( $\approx 1.505\text{eV}$  in this example), while the confinement energy contributes only to the total energy of the exciton in second order ( $\approx 5\text{meV}$  in this example). Since the thickness of the well layer only affects this confinement energy, variations in thickness have a smaller affect on the exciton resonance than they do on the Bragg resonance. As an example, a 10% variation in barrier and well thickness for a structure with a quantum well resonance at  $1.5\text{eV}$ , and in a background index  $n_b = 3.5$  leads to a range of barrier thicknesses ranging from  $104\text{nm}$  to  $115\text{nm}$  and subsequent energies ( $\hbar\omega_B$ ) ranging from  $1.43\text{eV}$  to  $1.58\text{eV}$ . The same 10% variation in well thickness ( $8.075\text{nm}$  to  $8.925\text{nm}$ ) results in exciton energies ranging from  $1.4995\text{eV}$  to  $1.5006\text{eV}$ . Similar tuning methods have been previously reported when looking at the normal modes of resonances confined in an optical cavity [36].

A second problem with the fabrication of BSQWs is that the growths can be extremely long. At a typical growth rate of  $\approx 0.5\text{ ml/sec}$ , the growth of an

N=200 quantum well Bragg structure can take nearly 48 hours. During this time period, instabilities in the system can cause small but significant deviations in the deposition rates of materials. To decrease growth time, the simplest solution is to grow structures at faster rates. Instead of the typical  $\approx 0.5$  ml/sec, growth rates may be increased (by increasing the material's sublimation rate) to around 1 ml/sec, bringing the total growth time down to approximately one day.

System instabilities can be corrected for using recalibration during growth. Reflection high energy electron diffraction (RHEED) measurements provide one means of doing this. In RHEED a beam of high energy electrons is reflected off the top monolayer of the structure and imaged onto a 2D camera. A series of diffraction spots are detected whose intensity is a maximum when the monolayer is complete, and a minimum when it is half formed. By measuring the frequency with which the intensity changes over the growth of several monolayers, an accurate determination of the growth rate can be determined and corrected for through cell temperature adjustments.

These techniques along with others listed in Ref. [34] can be used to speed up and improve the quality of BSQWs being grown by MBE. Even with this enhanced stability, growth times are still on the order of a day. While it's possible to extend such growth to a two day period, longer growth periods run further the risk of mechanical failures or instabilities in the system.

## 2.6 Using a transfer matrix to model optical properties of layered structures

The optical properties of a layered structure such as BSQWs can be theoretically modeled using the transfer matrix method, which has been outlined in detail in many publications (see Refs. [37, 38, 39], and [40] for more details). A brief derivation of a transfer matrix formalism using both linear indices of refraction and including a resonant contributions to the susceptibility is given in

## Appendix A.

To begin with, we consider only phenomenon in non-resonant material. Maxwell's equations then relate the plane waves on each side of a single unit cell and traveling in each direction (see Appendix A.2). Matching boundary conditions in each layer of the material, the transfer matrix for propagation across a layer of thickness  $a_j$  and index  $n_j$  into a second layer of index  $n_{j+1}$  is given by:

$$\begin{bmatrix} E_{j+1}^- \\ E_{j+1}^+ \end{bmatrix} = \underbrace{\begin{bmatrix} \frac{n_j+n_{j+1}}{2n_{j+1}} & \frac{n_j-n_{j+1}}{2n_{j+1}} \\ \frac{n_j-n_{j+1}}{2n_{j+1}} & \frac{n_j+n_{j+1}}{2n_{j+1}} \end{bmatrix}}_{\text{Boundary}} \underbrace{\begin{bmatrix} e^{-ik_j a_j} & 0 \\ 0 & e^{ik_j a_j} \end{bmatrix}}_{\text{Layer}} \begin{bmatrix} E_j^- \\ E_j^+ \end{bmatrix} \quad (2.11)$$

Here the  $j$  subscripts are integers numbering the layers in the material, and we have assumed normal incidence.  $E_j^\pm$  represents the waves traveling in both the left (+) and right (-) directions at the left edge of the  $j^{\text{th}}$  layer. The rightmost matrix arises from propagation across a layer, and hence imparts a phase shift of  $k_j a_j$  upon the beam where  $k_j = n_j \omega / c$  is the wave vector of the field in the layer, and  $\omega$  is the frequency of the light. The leftmost matrix arises from propagation across the interface into the next layer, and depends on the index contrast between the two layers. Writing this total transfer matrix for one unit cell as:

$$\mathcal{M}_j = \begin{bmatrix} \frac{n_j+n_{j+1}}{2n_{j+1}} & \frac{n_j-n_{j+1}}{2n_{j+1}} \\ \frac{n_j-n_{j+1}}{2n_{j+1}} & \frac{n_j+n_{j+1}}{2n_{j+1}} \end{bmatrix} \begin{bmatrix} e^{-ik_j a_j} & 0 \\ 0 & e^{ik_j a_j} \end{bmatrix} \quad (2.12)$$

propagation across another boundary and through a second layer is then accounted for by second matrix. The electric fields on the right and left sides of a complex layered structure can then be written as the product of a series of such matrices:

$$\begin{bmatrix} E_{N+1}^- \\ E_{N+1}^+ \end{bmatrix} = \left( \prod_{j=N}^1 \mathcal{M}_j \right) \underbrace{\begin{bmatrix} \frac{n_0+n_1}{2n_1} & \frac{n_0-n_1}{2n_1} \\ \frac{n_0-n_1}{2n_1} & \frac{n_0+n_1}{2n_1} \end{bmatrix}}_{\text{Initial Boundary}} \begin{bmatrix} E_0^- \\ E_0^+ \end{bmatrix} = \mathcal{M} \begin{bmatrix} E_0^- \\ E_0^+ \end{bmatrix} = \begin{bmatrix} m_{11} & m_{12} \\ m_{21} & m_{22} \end{bmatrix} \begin{bmatrix} E_0^- \\ E_0^+ \end{bmatrix} \quad (2.13)$$

where the total transfer matrix across the entire structure has now been rewritten

as a matrix  $\mathcal{M}$  with components  $m_{11}$ ,  $m_{12}$ ,  $m_{21}$ , and  $m_{22}$ , and an additional matrix to take into account the initial boundary. Assuming there are no fields traveling to the left after the sample, this reduces to two equations and three unknowns:

$$\begin{aligned} 0 &= m_{11}E_0^- + m_{12}E_0^+ \\ E_{N+1}^+ &= m_{21}E_0^- + m_{22}E_0^+ \end{aligned} \quad (2.14)$$

After a bit of algebra, this gives the reflection, and transmission:

$$\begin{aligned} R &= \left| \frac{E_0^-}{E_0^+} \right|^2 = \left| \frac{-m_{12}}{m_{11}} \right|^2 \\ T &= \left| \frac{E_{N+1}^+}{E_0^+} \right|^2 = \left| m_{22} - \frac{m_{21}m_{12}}{m_{11}} \right|^2 \\ A &= 1 - R - T \end{aligned} \quad (2.15)$$

As an example, imagine a continuous wave beam normally incident on an interface from air ( $n_{\text{air}} = 1$ ) into an infinite slab of glass ( $n_{\text{glass}} = 1.5$ ), with a single layer anti-reflection (AR) coating on its surface (as described in Sec. 1). In this case, the transfer matrix must take into account propagation across the interface from the incident medium into the coating (Air/AR boundary), propagation through the coating layer (AR layer), and then propagation across another interface into the substrate (AR/Glass boundary):

$$\begin{bmatrix} 0 \\ E_{\text{glass}}^+ \end{bmatrix} = \underbrace{\begin{bmatrix} \frac{n_{\text{glass}}+n_1}{2n_{\text{glass}}} & \frac{n_{\text{glass}}-n_1}{2n_{\text{glass}}} \\ \frac{n_{\text{glass}}-n_1}{2n_{\text{glass}}} & \frac{n_{\text{glass}}+n_1}{2n_{\text{glass}}} \end{bmatrix}}_{\text{AR/Glass Boundary}} \underbrace{\begin{bmatrix} e^{-ika} & 0 \\ 0 & e^{ika} \end{bmatrix}}_{\text{AR Layer}} \underbrace{\begin{bmatrix} \frac{n_1+n_{\text{air}}}{2n_1} & \frac{n_1-n_{\text{air}}}{2n_1} \\ \frac{n_1-n_{\text{air}}}{2n_1} & \frac{n_1+n_{\text{air}}}{2n_1} \end{bmatrix}}_{\text{Air/AR Boundary}} \begin{bmatrix} E_{\text{air}}^- \\ E_{\text{air}}^+ \end{bmatrix} \quad (2.16)$$

Multiplying these matrices and solving for the reflection from the material, one finds:

$$R = \frac{(n_{\text{glass}}n_1 - n_{\text{air}}n_1)^2 \cos^2(ka) + (n_1^2 - n_{\text{air}}n_{\text{glass}})^2 \sin^2(ka)}{(n_{\text{glass}}n_1 + n_{\text{air}}n_1)^2 \cos^2(ka) + (n_1^2 + n_{\text{air}}n_{\text{glass}})^2 \sin^2(ka)} \quad (2.17)$$

The cosine terms in this equation reach a maximum when  $ka = \omega n_j a/c = n\pi$ . At these wavevectors the sine terms are similarly equal to zero, and the reflection from the structure is equal to the bare reflection of the glass/air interface (i.e. it has not changed from the value it would have if no AR coating was present). When  $ka = (2n+1)\pi/2$ , the cosine terms drop to zero, while the sine terms determine the reflection from the structure. The reflection at this value of  $k$  ( $\omega$ ) can be tuned

by changing the index of refraction of the AR-Coating material (however, large values can require materials with indices of refraction approaching infinity). For a particular  $R_{\text{Goal}}$  value, the index should be equal to:

$$n_1 = \sqrt{n_{\text{glass}} n_{\text{air}} \frac{1 + R_{\text{Goal}}^2}{1 - R_{\text{Goal}}^2}} \quad (2.18)$$

For the simple case of bringing the reflection from the structure near to zero, a value for  $n_1 = \sqrt{n_{\text{air}} n_{\text{glass}}}$  is required. The reflection will oscillate between the maximum and minimum values gives above, producing an effect known as Fabry Perot fringing. Shown in Fig. 2.8 is the reflection from an infinite glass slab

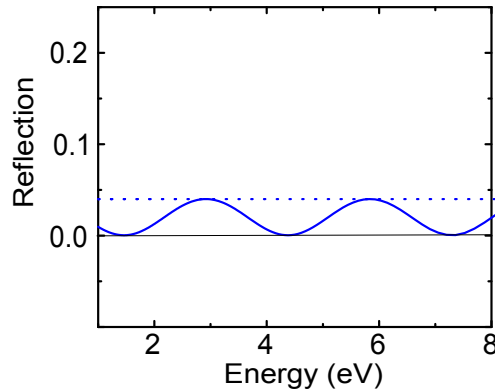


Figure 2.8: Reflection from glass with (solid) and without (dotted) an anti-reflection coating. The anti-reflection coating has a width is equal to  $\lambda/4n_1$  where  $\lambda = 1.5$  eV and  $n_1$  (the refractive index of the layer) is 1.225.

with (solid lines) and without (dotted lines) an anti-reflection coating on its surface of index  $n_1 = \sqrt{n_{\text{air}} n_{\text{glass}}} = 1.225$ . At the design energy ( $\approx 1.5$  eV) the reflection decreases to nearly zero.

## 2.7 Linear properties of Bragg-spaced quantum wells

To model the linear properties of quantum wells, and specifically BSQWs, the transfer matrix must take into account changes to the complex index of refraction due to the quantum well exciton resonance. This involves introducing a resonance

polarization component,  $P_{\text{res}}$  to Maxwell's Equations.

For the structures used here (and all BSQWs that have been fabricated to date) low- $x$   $\text{In}_x\text{Ga}_{1-x}\text{As}/\text{GaAs}$  quantum wells are used. They were chosen for the increased  $hh/lh$  splitting brought about by the strain between the In and GaAs [41, 42, 43], and because the index contrast between low- $x$   $\text{In}_x\text{Ga}_{1-x}\text{As}$  and GaAs is negligible. In addition, because these are type-I quantum wells, the exciton resonance is below the fundamental bandgap of the GaAs barrier layers, and as such, the barriers and GaAs substrate the quantum wells were grown on are (for the most part) transparent to light at these wavelengths. Because the wells are thin with respect to the envelope of the field, propagation through the quantum well can be ignored and instead accounted for entirely by the polarization introduced by the well. In this case, the transfer matrix of a single barrier-well unit cell in the system can be rewritten in terms of the susceptibility of the well (see Appendix A.3):

$$\mathcal{M} = \begin{bmatrix} e^{iqa}(1 + \beta) & e^{-iqa}\beta \\ e^{iqa}\beta & e^{-iqa}(1 - \beta) \end{bmatrix} \quad (2.19)$$

where  $q = n_b\omega/c$  is the wave vector of the photon (assumed here to be in the  $z$ -direction),  $a$  is the width of a single quantum well/barrier unit (this contains the Bragg frequency  $a = c\pi/n_b\omega_B$ ), and  $\beta = i\omega\chi^{2D}(\omega)/2n_b c$ ,  $\chi^{2D}(\omega) = \frac{|\tilde{\phi}^{2D}(0)|^2\varphi^2}{\epsilon_0\hbar} \frac{1}{\omega - \omega_X - i\gamma}$  is the 2D-susceptibility of the exciton. In this expression for the susceptibility,  $\tilde{\phi}^{2D}(\vec{r} = 0)$  is the 2D-exciton wavefunction, where  $\vec{r}$  designates the separation between electrons and hole wave functions,  $\epsilon_0$  is the permittivity of free space,  $\varphi$  is the component of the dipole moment of the exciton along  $\vec{E}$ ,  $n_b$  is the background refractive index of the system, and  $\gamma$  is the polarization non-radiative dephasing rate of the system. Note that this can also be written using a complex, frequency dependent index of refraction in Eq. 2.11.

As is described in Appendix A and Sec. 2.6, the total transfer matrix for a complex system can be written in terms of a product of individual transfer

matrices for each layer in the system. Since all the unit cells in the crystal are the same (a thick barrier followed by a thin, resonant quantum well layer), they all share the same transfer matrix for transfer across a layer. As such, for a system with  $N$  identical quantum wells and barriers, the total transfer matrix is:

$$\begin{bmatrix} E_N^+ \\ E_N^- \end{bmatrix} = \underbrace{\mathcal{M}^N}_{\text{Initial Boundary}} \begin{bmatrix} \frac{n_0+n_b}{2n_b} & \frac{n_0-n_b}{2n_b} \\ \frac{n_0-n_b}{2n_b} & \frac{n_0+n_b}{2n_b} \end{bmatrix} \begin{bmatrix} E_0^+ \\ E_0^- \end{bmatrix} \quad (2.20)$$

where  $n_0$  represents the index of the incident medium, and  $n_b$  the index of the barrier material.

When light is inside the material it can become coupled to the exciton dipoles inside resulting in a coupled state of the exciton and photon, known as an exciton-polariton. Solving Eq. 2.19 for eigenvalues (see Appendix B) a polariton dispersion relation for the material can be written:

$$\cos(ka) = \cos(qa) + \frac{\Gamma}{(\omega + i\gamma) - \omega_X} \left( \frac{\omega}{\omega_X} \right) \sin(qa) \quad (2.21)$$

where  $\Gamma = \frac{|\bar{\phi}^{2D}(0)|^2 |\phi|^2 \omega_X}{2\epsilon_0 n_b \hbar c}$  is the radiative decay rate of the resonance and  $k$  is the polariton wavevector for light traveling inside the structure.

Finding the reflectivity and transmission coefficients requires calculating  $\mathcal{M}^N$ . This can be done using these eigenvalues and the associated eigenvectors of the transfer matrix (see Appendix B). An early analysis of this system [44] found that at Bragg periodicity ( $\omega_B = \omega_X$ ) the reflection could be written in the following form:

$$r_N(\omega) = \frac{-iN\Gamma}{\hbar(\omega_X - \omega - i(\gamma + N\Gamma))} \quad (2.22)$$

where  $N$  is the number of quantum wells in the sample. The presence of the  $N\Gamma$  term here originally led to the conclusion that compared with non-Bragg-spaced MQWs these materials demonstrated an enhanced decay rate. While this enhanced decay rate has been observed [45], this description of the reflection becomes inaccurate when the number of quantum wells is large [46, 47].

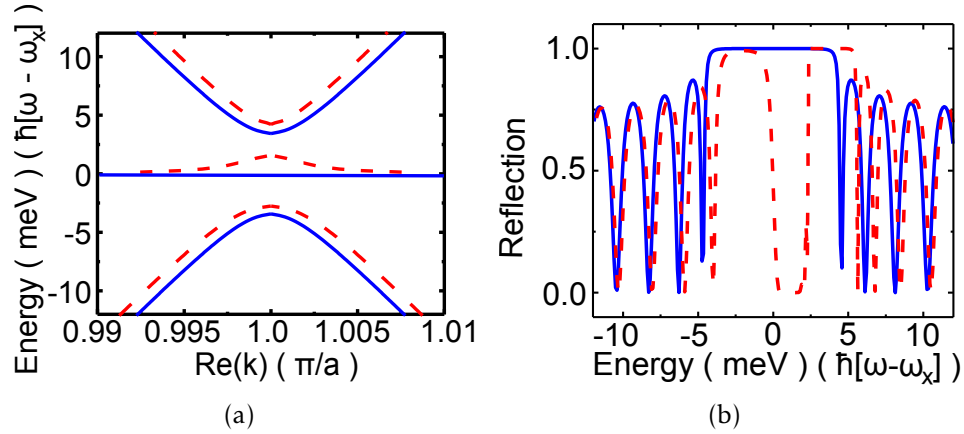


Figure 2.9: Photonic bandstructure of Bragg-spaced quantum wells. (a) Calculated photonic band structure using Eq. 2.21. Solid blue lines show the band structure when  $\omega_B = \omega_X$  and the dotted red lines show the band structure when  $1.001\omega_B = \omega_X$ . (b) A calculation of the reflection from BSQWs when  $\omega_B = \omega_X$  (blue, solid) and  $\omega_B \neq \omega_X$  (red, dashed).

The real part of  $k$  in Eq. 2.21 is plotted in Fig. 2.9(a) for a range of energies near the Bragg resonance, and for two detunings of  $\omega_B$  and  $\omega_X$ . Fig. 2.9(b) shows the reflection from a simulated BSQW structure using similar material properties. Note, this photonic band structure looks similar to the electronic band structure talked about earlier in semiconductor materials (Fig. 2.2), except in this case rather than describing *electron energy* versus wave vector it describes *polariton energy* versus wave vector. For energies far from  $\omega_B$  or  $\omega_X$ , the sine term in the right hand of Eq. 2.21 is small and the dispersion relation is linear ( $qa = ka$ ). When  $\omega \approx \omega_B \approx \omega_X$  the second term blows up forcing  $q$  to take on imaginary values. Because there are no states available for polaritons at these wavelengths, they are not able to exist in the structure. As a result the structure efficiently reflects light with frequencies in this bandgap.

In contrast to the electronic bandgaps described earlier, a nearly flat intermediate band with width  $\omega_B - \omega_x$  lies halfway between the two band edges. Shown as the solid, blue lines in Fig. 2.9(a) and Fig. 2.9(b) is the situation when  $\omega_B = \omega_X$ . In

this case the intermediate band is flat and pulses with energies resonant with the band can not propagate through the structure (i.e. pulses at these energies have zero velocity inside the material). When  $\omega_B$  and  $\omega_X$  are slightly detuned from one another [red, dashed line in Fig. 2.9(a) and Fig. 2.9(b)] the intermediate band broadens to cover the area between the two resonances, and appears as a window in the simulated reflection stopgap.

## 2.8 History of studying nonlinearities in photonic crystals

As mentioned, resonant photonic bandgap structures (RPBGs) differ from non-resonant ones in that the imaginary part of the materials susceptibility is modulated along with the real part. The presence of an absorption resonance means excitation of carriers is resonantly enhanced, and can be achieved with relatively weak electro-magnetic fields. These real or virtual excited carriers can change the index and absorption of the resonance, and as such alter the photonic band structure of the material.

Much of the research on nonlinearities in Bragg structures to date has been focused on inducing nonlinearities in fiber Bragg gratings. They have been used to demonstrate optical pulse generation from continuous wave beams [48], pulse compression [49, 50], and slow light [51, 52, 53]. Specifically, there has been some interest in creating temporal solitons inside photonic bandgap structures. Solitons in bulk media are formed when nonlinearities generate a dispersion that exactly counteracts the linear dispersion [54], and provide an interesting medium for storing and trapping optical pulses [55, 56]. While there has been work done looking for gap solitons in BSQWs, it is only mentioned here because of its historical significance.

Many of these experiments in Bragg-fibers have focused on using Kerr nonlinearities (nonlinearities written generally in the form  $n = n_0 + 2n_2|E(\omega)|^2$ )

where  $n_0$  is the linear index of the material,  $n_2$  is the second order change in the index). The resonances present in fiber Bragg gratings are typically far from the wavelengths of light propagating through the fibers [57, 49]. Quantum well Bragg structures provide an interesting alternative, as the proximity of the resonance to the frequency of the light allows nonlinearities to be excited with lower fluences per unit length:  $\text{MW}/\text{cm}^2$  in a material that is  $\mu\text{m}$  in length as opposed to 10s of  $\text{GW}/\text{cm}^2$  in fiber gratings that are 10s of cm long [51, 58]. These size and power advantages make RPBGs appealing for applications such as slowing and switching optical signals in high speed communications networks.

## 2.9 Applications of Bragg-spaced quantum wells in modern communication systems

To see how optical logic devices such as all-optical switches or optical buffers could be useful, some background on modern communications systems is necessary. Modern communication networks have come to rely on large optical transport layers (i.e. optical fibers working in conjunction with the old electronic network) to send signals from one switching station to another. Optical fibers are advantageous for this because of their large optical bandwidth (around 1 Terabyte per second). This amounts to around 1/2 billion telephone calls or 300,000 high definition television stations being supported by a single fiber simultaneously [59].

Unfortunately because electronic components typically rely on the transport of electrons they are not able to process data at these rates. Starting with the first ‘web boom’ in the late 1990’s the need for devices capable of fast processing has risen. Though some solutions have been implemented (i.e. slow optical switching solutions are in place to route signals, and perform wavelength conversion), components with the ability to control individual bits at these rates are still not commercially available [60, 61]. The desired optical logic components include AND, OR, XOR, NOT, NOR, etc. gates, with the goal being to perform logic on individual bits

within a signal or header stream.

For instance, to check if two headers match, one would want to cross correlate two pulse streams and look for matches between the two (stream 1  $\equiv$  stream 2). Because the time to resend signals that are read incorrectly can pose a major bottleneck in system performance, it is desirable to have large signal to noise ratios (low bit error rates) [62], and have them work fast enough to resolve an optical stream at the same rate that it is encoded (i.e. on picoseconds time scales)<sup>1</sup>.

Individual bits within a header signal can contain information about the payload behind it. For instance, it is common in synchronous networks (i.e. networks where packets arrive at set intervals, and where every packet is encoded at the same bit rate) to have single bits in the header which describe the payload. Fast optical switching techniques could be used to read these with single bit granularity without imposing any slowdown in the network.

Optical buffers capable of storing a train of pulses are also needed. This can include situations where a signal needs to synchronize with a network, situations where a header cannot be processed quickly enough, or situations where a switching fabric cannot be reconfigured fast enough. Optical buffers are used to store the payload while other processes happen, and then release it when the system is ready.

Fast optical switches can also be used to help manage different of optical networks. As an example, imagine a stream of information from some electronic source. Because most of the signals traveling across communications networks originate from electronic devices, this signal may be at a fairly low bit rate (100 ps/bit or 1 Gb/sec). An optical switch can be used to temporally filter this signal down to a set of bits that are temporally shorter for temporal multiplexing. By

---

<sup>1</sup>While optical pulses can be created that are much shorter than 1ps, the desire for wavelength division multiplexing in many optical communication systems limits the spectral bandwidth available to each signal. As such, time-bandwidth products force pulses to a minimum temporal width.

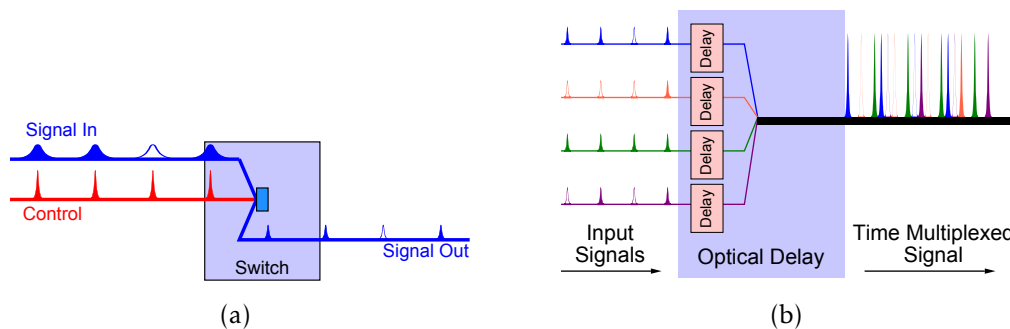


Figure 2.10: Applications of Bragg-spaced quantum wells. (a) An example of using an optical switch to temporally filter a long signal. (b) Using optical delay lines to synchronize and time division multiplex several signals.

switching the signal with a series of short control pulses, a cross correlation of the two is performed, and a copy of the signal stream (with the same bit rate, but shorter individual bits) can be made (see Fig. 2.10(a)).

A large number of these signals can then be brought together and temporally multiplexed on a single fiber optic cable, however it is important that no two pulses travel through the fiber at the same time and wavelength. If a temporal or wavelength node on a fiber is unavailable when the signal arrives, the network is said to be “blocked”, and signals often have to be discarded and resent later. Tunable delay lines allow storing a pulse until the network is available, or to keep a signal in sync with the network clock (see Fig 2.10(b)).

Similar techniques can be used to demultiplex the signal when it reaches its destination. In addition other potential applications exist in areas such as optical header processing [63, 64], avionics [65], and chip-to-chip communications [66, 67]. The desire to find small yet reliable components has grown significantly in the past 10 years, and will continue to grow as bandwidth demands increase.

## 2.10 All-optical switching

The desire for increasing bandwidth has driven interest in ultra-fast all-optical switches to perform logic with, and modulation of optical signals. All-optical switching is a general term describing any process whereby the amplitude of an optical signal pulse is modulated by a second optical control pulse through the nonlinear optical response of a material [68]. In the *off* state many optical switches, a signal pulse is incident on the sample, and the reflected or transmitted beam is detected. A stronger control pulse induces changes to the reflectivity (or transmissivity in transmission switches) of the device through nonlinear absorption or refractive index changes. These changes modulate the intensity of the signal pulse, and that change is detected as a switching signal (see Fig. 2.11).

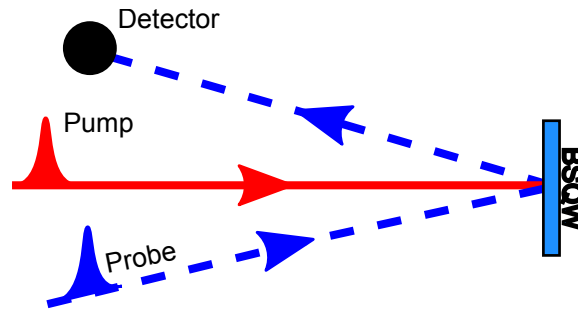


Figure 2.11: Setup of an amplitude optical switching experiment. The pump pulse (red solid) induces a nonlinearity in the structure, the changes the reflection of a signal pulse (blue dashed). Those changes are detected as switching signals.

Switch performance can be characterized by several figures of merit including:

**Contrast ratio (CR)** (or modulation ratio), defined by:

$$\text{CR} = \frac{T^{\text{on}}}{T^{\text{off}}} \text{ or } \frac{R^{\text{on}}}{R^{\text{off}}} \quad (2.23)$$

where  $T^{\text{on/off}}$  and  $R^{\text{on/off}}$  are the fraction of light transmitted or reflected in the on and off states of the switch. Frequently contrast ratio is written in

units of decibels (dB), given by:

$$CR_{\text{dB}} = 10\log(CR) \quad (2.24)$$

**Throughput (TP)** (or insertion loss) defines the percent of incident light that reflects from or transmits through the material in its on state. Typically this is the same as the numerator in contrast ratio expressions ( $T^{\text{on}}$  and  $R^{\text{on}}$ ). Similarly to CR, TP is often expressed in units of dB:

$$TP_{\text{dB}} = 10\log(T^{\text{on}}) \text{ or } 10\log(R^{\text{on}}) \quad (2.25)$$

Because contrast ratio is a ratio of on and off-state throughput ( $R^{\text{off}}$  and  $T^{\text{off}}$ ), high contrast ratio switching can be achieved in low throughput devices by decreasing the switch's off-state.

**Switching time** can include both the rate at which the switch turns on (turn-on or risetime), the rate at which it turns off (turn-off or fall-time). Ideally, turn-on and turn-off times are limited by the temporal characteristics of the control pulses used for switching. Material parameters often come into play and ultimately limit the rate at which a switch can turn on or off.

**Recovery time** (a.k.a. data transfer rate) is the maximum rate at which the material can recover from a switching operation, and as such the time until a second switching event can occur. Again, this would ideally be infinitely fast. In practice, materials often can *not* recover at the rate of all-optical communications systems operate (THz or ps), ultimately limiting the information throughput of the switch.

**Bandwidth** is the range of frequencies over which the switch operates. Ideally, switches will operate over a large bandwidth, because that allows control both of pulses with different frequencies, as well as pulses that are temporally short (spectrally broad). However, it is often easiest to generate large changes in reflection or transmission (and as such large changes in CR and

TP) in very narrow wavelength regions (i.e. shifting a sharp resonance a small amount generates a large change in absorption and index over a very narrow range of wavelengths).

**Size** generally indicates the width or length of the device. Smaller size devices generally cost less to produce and provide more convenient methods of integration than large scale devices.

**Switching fluence** is the fluence required to switch the signal. Low switching power is desirable for efficiency, scalability, and cost.

**Wavelength of operation** includes the general input wavelengths at which the device operates. For integration into today's optical communication networks this would ideally fall into the 1.53-1.57 $\mu\text{m}$  range, with the hope of extending that to 1.30-1.65 $\mu\text{m}$  in the next decade. Most of the devices discussed in this dissertation are built on GaAs/AlGaAs or GaAs/InGaAs platforms, and operate near 830nm, although a few MQW switches have been demonstrated in InGaAs(P)/InGaAsP providing resonances nearer to communications wavelengths [69, 70].

### 2.10.1 Amplitude switching

Some of the first examples of optical switching were amplitude switches. An enormous body of research exists studying different types of amplitude switches implemented via a variety of techniques. In general though, such switches operate by modulating the amplitude of the electric field transmitted or reflected from a material. MQW materials, in particular, are useful for such switches because the 1s-hh exciton resonance allows the excitation of large nonlinearities with fairly weak control pulses when compared to bulk semiconductor materials.

Many of the earliest examples of optoelectronic amplitude switches using

MQW materials were based on the quantum-confined Stark effect (QCSE). A MQW material is placed in an electric field oriented perpendicular to the quantum well layers. When an exciton is excited in the well layers, the electron and hole comprising the exciton are pulled apart due to the applied field. However, the presence of the quantum well walls inhibits the total ionization of the exciton (i.e. neither electron nor hole has enough energy to escape into the barrier layers), and as a result the exciton absorption resonance is shifted to lower energies rather than destroyed entirely. A similar effect known as Wannier-Stark localization can occur in semiconductor superlattice structures, where electron and hole wavefunctions can become localized in individual sets of wells due to the imposition of an electric field [71, 72]. This shift of the absorption resonance in the material can then be used to construct an amplitude switch. Several examples of these types of optoelectronic switches have been demonstrated to date [73, 74], with typical contrast ratios of around 10:1 (10dB), and switching times in the range of 100s of ps to ns. Faster ( $\approx 33$ ps) switching is attainable by use of narrower barrier widths in these materials, effectively reducing the RC time constant of the material [75].

All-optical counterparts of these electro-optic switches have also been investigated, using optically generated carriers to screen the static electric field placed across the wells [76, 77]. In this case, the turn-on rate for switching is generally controlled by the rate that carriers can escape the wells and travel time to the p/n nodes of the device, and in general can take from 1-100 ps. Turn-off time is enhanced in these materials due to "giant ambipolar diffusion" (i.e. the spatially separated electrons and holes experience an enhanced Coulomb repulsion) [78]. Switches of this type have demonstrated contrast ratios of 2:1 and insertion losses of 2dB, for switching energy of  $\approx 0.5\mu\text{J}/\text{cm}^2$  and over an optical bandwidth of 16 meV [79].

One alternative method for further improving these switches involves the use

of asymmetric Fabre-Perot etalon structures. In such structures, a resonant cavity is created with a resonance placed inside. By tailoring the cavity and resonance, structures with very low off-state reflectivity can be designed. For example, using the simple transfer matrix techniques described in Sec. 2.6, a cavity with front and back reflectors can be modeled. If the reflection from the front  $R_f$  and back  $R_b$  reflectors are tailored such that  $R_f = R_b e^{-2\alpha d}$  where  $\alpha$  is the absorption of the cavity material, and  $d = \lambda_{\text{ASFP}} j / 2n$  where  $n$  is the index of the cavity material,  $\lambda_{\text{ASFP}}$  is the wavelength of interest and  $j$  is an integer denoting the mode index, the reflection coefficient in the off state of the switch can be set (theoretically) to exactly zero. If the resonance is shifted somewhat via the QCSE [80] or many-body interactions [81, 82, 83, 84, 85], only a small amount of light may be reflected (i.e. low throughput), but the overall contrast ratio of the device ( $R^{\text{on}}/R^{\text{off}}$ ) may be infinite. Material parameters have limited this technique, however modulators with contrast ratios of  $> 60 : 1$  and throughputs of  $\approx 4.6 \text{ dB}$  have been demonstrated over a fairly narrow bandwidth [80].

BSQWs are interesting all-optical switching materials because the high reflectivity allows the pump to be near to the exciton resonance without experiencing significant absorption, thereby exciting large nonlinearities with fast recovery times. In addition, at the steep edges of the reflectivity stop band small shifts of that bandgap can result in large reflectivity changes, which in turn result in large contrast ratios for the switch. In BSQWs the first examples of all-optical amplitude switches were shown by Prineas et. al. in 2002 [86].

### 2.10.2 Polarization switching

Polarization switches operate by changing the overall polarization state of a pulse, rather than its amplitude. Such switches have previously been demonstrated in semiconductor materials based on uniaxial strain of quantum

well samples [87], quantum well etalons [88], and the photo-refractive effect [89]. The devices are constructed in the same manner as an amplitude switch, except the sample is placed between a crossed polarizer-analyzer pair (see Fig. 2.12). When no control pulse is present the signal pulse reflects from or transmits through the material and is blocked by the analyzer, so no signal is detected. When a control pulse is present, it interacts with the signal inside the material, and the transmitted (or reflected) signal's polarization state is changed. This allows some of it to pass the analyzer and be detected as the on-state for the switch.

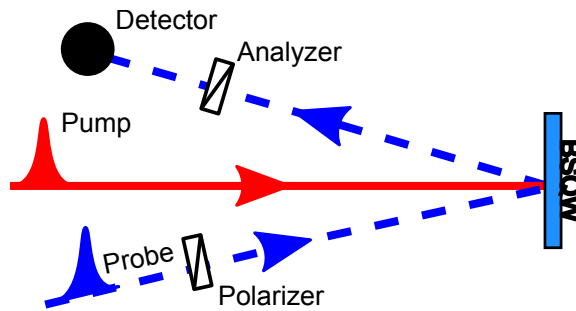


Figure 2.12: Setup of an all-optical polarization switching experiment. The circularly polarized pump pulse (red, solid) induces a nonlinearity in the structure for one circular polarization, creating a circular-dichroism and/or circular-birefringence. These cause the linearly polarized probe pulse's (blue, dashed) polarization to be rotated, and the changes are detected as switching signals.

The contrast ratio of such a switch can be written in terms of the properties of the polarization optics, and the response of the material. To begin, we consider a signal pulse of the form:

$$\vec{E}(z, t) = \vec{\mathcal{E}}e^{i(kz - \omega t)} + c.c. \quad (2.26)$$

where  $k$  is the wavevector of the pulse,  $\omega$  its frequency, and  $\vec{\mathcal{E}}$  the field amplitude. For a general elliptically polarized pulse, this field amplitude can be written in the form [90]:

$$\vec{\mathcal{E}}(\omega) = \mathcal{A} \begin{bmatrix} \cos(\theta_{\text{sig}}(\omega)) \cos(\epsilon(\omega)) - \iota \sin(\theta_{\text{sig}}(\omega)) \sin(\epsilon(\omega)) \\ \sin(\theta_{\text{sig}}(\omega)) \cos(\epsilon(\omega)) - \iota \cos(\theta_{\text{sig}}(\omega)) \sin(\epsilon(\omega)) \end{bmatrix}^T \begin{bmatrix} \hat{x} \\ \hat{y} \end{bmatrix} \quad (2.27)$$

where  $\mathcal{A}$  is defined in terms of the half-lengths of the major (a) and minor (b) axis of a polarization ellipse ( $\mathcal{A} = \sqrt{a^2 + b^2}$ ),  $T$  represents the transpose of a matrix or vector,  $\theta_{\text{sig}}(\omega)$  represents the fields orientation, and  $\epsilon(\omega)$  its ellipticity. In general, ultrafast pulses can have spectral widths over which  $\theta_{\text{sig}}$  and  $\epsilon$  can vary dramatically, and as such the orientation and ellipticity have been written as a function of  $\omega$ , and the orientation and ellipticity of each individual wavelength kept track of as they propagate through the switch.

In this coordinate system, the Jones matrices for a polarizer aligned along the y-axis can be written in the form:

$$J_{\text{pol}}^y = \begin{bmatrix} \eta & 0 \\ 0 & 1 \end{bmatrix} \quad (2.28)$$

where  $\eta$  represents the extinction ratio of the polarizer. When the transmitted (or reflected) field from the switch passes through the analyzer, the resulting field ( $\vec{E}_T(\omega)$ ) has a form:

$$\vec{E}_T(z, t) = J_{\text{pol}} \vec{E}(z, t) \quad (2.29)$$

and the reflected/transmitted intensity:

$$I_T(\omega) \propto |\vec{E}_T(\omega)|^2 = |\mathcal{A}|^2 \frac{t}{2} (1 - \eta) \left[ 1 - \cos(2\theta_{\text{sig}}(\omega)) \cos(2\epsilon(\omega)) \right] + \eta t |\mathcal{A}|^2 \quad (2.30)$$

where  $t$  (although  $r$  could be used for a reflection geometry) is a real constant modifying the amplitude of the transmitted (reflected) field. Assuming the incident field is perfectly linearly polarized ( $\theta_{\text{sig}} \approx \epsilon \approx 0$ , and normalizing out the incident field strength,  $|\mathcal{A}|^2$ , we find the throughput:

$$\text{TP}_T^{\text{on}}(\omega) = \left[ \frac{1}{2} (1 - \eta) \left( 1 - \cos(2\theta_{\text{sig}}(\omega)) \cos(2\epsilon(\omega)) \right) + \eta \right] t^{\text{on}} \quad (2.31)$$

where the on/off superscripts denote the on/off state of the switch. The contrast ratio can also be written:

$$\text{CR}_T(\omega) = \frac{\text{TP}_T^{\text{on}}(\omega)}{\text{TP}_T^{\text{off}}(\omega)} \quad (2.32)$$

If, in the off-state of the switch, no polarization state changes occur ( $\epsilon^{\text{off}} = \theta_{\text{sig}}^{\text{off}} = 0$ , the off-state throughput reduces to  $\text{TP}_T^{\text{off}} = t^{\text{off}} \eta$ , and the contrast ratio can be

written by definition as:

$$\text{CR}_T(t) = \left[ \frac{1}{2\eta} (1 - \eta) (1 - \cos(2\theta_{\text{sig}}(\omega)) \cos(2\epsilon(\omega))) + 1 \right] \frac{t^{\text{on}}}{t^{\text{off}}} \quad (2.33)$$

High quality polarizers commercially available today can block nearly 100% of off-axis light passing through them, allowing the *off* state of such switches to be extremely low. As an example, if amplitude modulations in the material are small (i.e.  $\frac{T^{\text{on}}}{T^{\text{off}}} \approx 1$ ), and only a small modulation of the pulse orientation occurs (i.e.  $\theta_{\text{sig}}^{\text{on}} \approx 6^\circ$  and  $\epsilon^{\text{on}} = 0$ ), a polarizer with an extinction ratio  $\eta \approx 10^{-5}$  can achieve a contrast ratio of over 1000:1. The caveat is that system throughput is typically very small. In this example, sample absorption has been ignored and the throughput is still a relatively weak  $\approx 1\%$ .

MQW all-optical polarization switches typically operate with control and signal pulses tuned near the exciton resonance or above the fundamental band-edge. This allows the switch to utilize the nonlinearities associated with carrier generation in these structures. These "resonant polarization switches" have been previously demonstrated in a number of materials. For example, the photorefractive effect has been used to generate energy transfer from a pump beam into a probe beam [89]. Exciting the sample with multiple pulses results in the formation of index gratings in the material. Light incident on this grating is scattered into new directions. The crossed analyzer after the sample blocks much of the light transmitted in the switches off state, and as such large contrast ratios have been recorded ( $< 10,000 : 1$ ). However, the gratings produced live for a long time in the structure, resulting in slow turn off times (100s of ps) and slow recovery of the sample.

Anisotropic materials have also been used to demonstrate polarization switching. In these materials, a difference in absorption and index occurs naturally for x- and y-polarized light, given by  $\alpha_{x/y}$ . A control pulse can excite changes in these absorption coefficients such that  $\alpha_{x/y}^{\text{on}} = \alpha_{x/y}^{\text{off}} + \Delta\alpha_{x/y}$ , and the resulting signal

pulses experience a change in their orientation ( $\theta_{\text{sig}}$ ). Since III-V semiconductor MQW materials grown in the [001] direction do not possess an intrinsic in-plane anisotropy, demonstrations of polarization switching in these materials have typically relied on uniaxial strain to induce an anisotropy [87] or unconventional growth and excitation conditions [91]. Both bleaching of the absorption resonance due to many-body effects, and shifts of the resonance due to the QCSE have been used to demonstrate all-optical polarization switches in these types of materials.

Resonant *spin* switches operate by generating an anisotropy in a material via the injection of spin-polarized populations of carriers. The introduction of a spin-polarized population induces a circular dichroism and birefringence in the material (i.e., a difference in absorption coefficient and index of refraction, respectively, for right and left circularly polarized light). In III-V semiconductor quantum wells (and hence BSQWs) this dichroism/birefringence can be induced via the circular selection rules for the *hh*-exciton mentioned earlier (Sec. 2.3) [92]. A pump excites nonlinearities in the spin-up system but not the spin-down system, causing the right and left circular components of a linearly polarized signal pulse to be reflected differently. This circular anisotropy changes the polarization state of a linearly polarized signal pulse. The change in the signal polarization is subsequently converted to a modulation of the signal amplitude by using additional polarization sensitive elements. The circular dichroism and birefringence induced by the control pulse will persist as long as the spin-polarized carrier population is present.

All-optical polarization switches that make use of spin-polarized carriers in semiconductor multiple quantum wells have demonstrated high contrast (i.e., large on-off ratios) [88, 69, 70, 84, 93] and have the potential for high-speed performance. [84, 94]. In ultrafast resonant spin polarization switching using MQW structures, switch turn off time is limited by the spin-relaxation time of the

sample, and switch recovery time by the time it takes for carriers to recombine or be swept out. For resonant excitation, the carrier lifetime is often longer than the spin relaxation time. Even though the turn-off time of the switch is determined by the carrier spin relaxation time, the sample will not fully recover until the carriers recombine or are swept out of the active region. Thus, the repetition rate of the device can ultimately be limited by carrier accumulation.

More recently, polarization switches have been reported [95, 94, 96] in which nonlinearities are excited by non-resonant excitation of a material. These carriers exist only while the pump is present, resulting in an enhanced turn-on, turn-off, and recovery times of the material. This comes at the cost of large pump energies required to excite nonlinearities with below resonance excitation.

In MQW samples, spin-polarized populations of virtual carriers can also be created by tuning the a circularly polarized control below resonance. In the absence of any real carrier generation or dephasing (i.e. collisions between carriers which remove their coherence with the applied field), the virtual carrier population follows the control pulse envelope, and both switching and recovery times are control pulse width limited. Non-resonance MQW switches utilizing bleaching [97], the QCSE [98], and coherent-many-body effects [94] have demonstrated contrast ratios of  $\approx 300 : 1$  ( $\approx 25\text{dB}$ ) and switching times of  $\approx 350$  fs (control pulse width limited) over bandwidths near  $\approx 1$  THz ( $\approx 5$  meV); however, these results still required large switching energies  $\approx 350$  MW/cm<sup>2</sup>, and demonstrated large insertion losses  $\approx 21$  dB corresponding to a throughput (i.e., transmission in the on state) of  $\approx 1\%$ .

## CHAPTER 3 RESEARCH

This research shall describe the unique linear and nonlinear optical properties of BSQWs [86], along with applications of those nonlinearities in an all-optical polarization switch [1, 3] and as a medium for slow light [2, 38, 99, 4]. In addition, the underlying nonlinear processes in BSQW are looked at, and the underlying physical mechanisms responsible for these nonlinearities examined.

The switches take advantage of the properties of a BSQW structure that is grown such that its fundamental Bragg frequency  $\omega_B$  ( $\omega_B = \pi c/n_B \omega_B$ , where  $n_B$  is the background index and  $\omega_B$  the spacing of the quantum wells) is approximately equal to the heavy hole (hh) exciton frequency  $\omega_x$  of the quantum well. When these two frequencies are approximately equal, the photonic bandstructure includes a forbidden gap (and an associated reflection stopgap) with both resonance frequencies located within the gap [2, 38, 99]. Incident frequencies within this stopgap are efficiently reflected by the sample. Such BSQWs have been shown [86, 1] to exhibit large optical nonlinearities and sub-ps recovery times at 10K when a spectrally narrow control (or pump) pulse is tuned within the forbidden gap.

### 3.1 All-optical polarization switching in Bragg-spaced quantum wells<sup>1</sup>

As was mentioned in Sec. 2.10.2, spin-based polarization switches using circular, optically-induced anisotropies in semiconductor multiple quantum wells have been previously shown to exhibit large contrast ratios, usually at the expense of throughput [94, 93, 100, 101]. Here a polarization switch is demonstrated that exhibits a dramatically improved throughput ( $\approx 40\%$  or 3dB), an increased contrast ratio ( $\approx 10,000 : 1$  or  $\approx 40$  dB), and a reduced switching energy ( $\approx 14$

---

<sup>1</sup>Much of this section is reproduced with permission from Ref. [95] and Ref. [96].

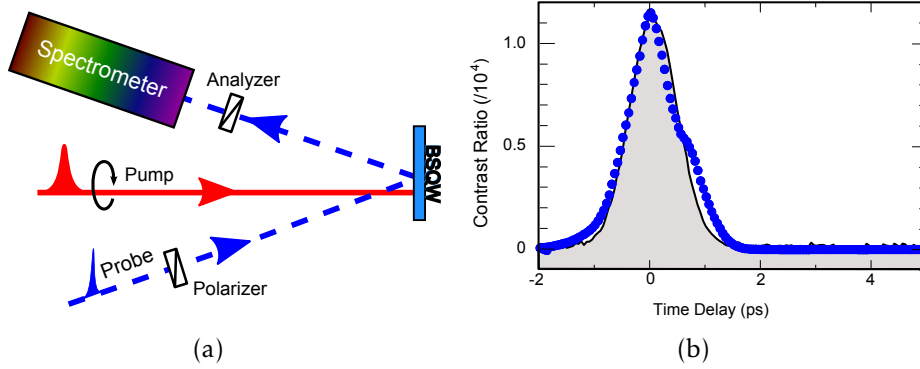


Figure 3.1: All-optical switching in Bragg-spaced quantum wells. (a) Setup for switching experiments with the probe pulse spectrally resolved after the switching material. (b) Contrast ratio (solid circles) as a function of control-signal delay ( $\tau$ ) for a  $14 \mu\text{J}/\text{cm}^2$ , 1 ps control pulse, and a 650 fs signal pulse spectrally positioned as shown in Fig 3.2. The temporally resolved control pulse (solid line) is shown for comparison.

---

Reproduced with permission from Ref. [1].

$\mu\text{J}/\text{cm}^2$ ), while maintaining  $\approx 1$  ps switching time and exhibiting no apparent carrier accumulation.

This switch takes advantage of the properties of a BSQW structure grown via an MBE process similar to the once described in Sec. 2.5. Previous investigations of the same sample have shown large optical nonlinearities and sub-ps recovery times when a spectrally narrow control pulse is tuned within the forbidden gap [86, 102]. Here, we use these properties to construct polarization switch that is based on the spin-dependent selection rules for the BSQW photonic band gap.

### 3.1.1 10K All-optical polarization switch

The sample consists of 200 periods of 8.5 nm wide  $\text{In}_{.04}\text{Ga}_{.96}\text{As}$  quantum wells separated by GaAs barriers such that the period,  $a$ , is equal to one-half the excitonic wavelength in the material ( $a = c/\omega_x n_b$ , where  $n_b$  is the background index of GaAs at  $\omega_x$ ). The switch is constructed by placing the sample between

crossed polarizers in a reflection geometry (see Fig. 3.1(a)). A  $14 \mu\text{J}/\text{cm}^2$ , spectrally narrowed [1 ps, 1.3 meV full width at half maximum (FWHM)] circularly polarized control pulse, and (for these initial low-temperature measurements) a spectrally broadband (650 fs, 2.5 meV, FWHM) linearly polarized signal pulse are both generated by external shaping of 80 fs pulses from a mode-locked Ti:Sapphire laser and are tuned near the low-energy edge of the reflectivity stop band of the BSQW, as indicated in Fig. 3.2. The sample was mounted in a cryostat that was cooled to 10 K.

The contrast ratio of the switch as a function of time delay ( $\tau$ ) between the signal and control is shown in Fig. 3.1(b). The time-resolved control pulse is shown for comparison. A maximum contrast ratio of  $\approx 11100 : 1$  (40.4 dB), a throughput of  $\approx 40\%$  (3 dB), and a control-pulse-width-limited switching time ( $\approx 1$  ps) are observed.

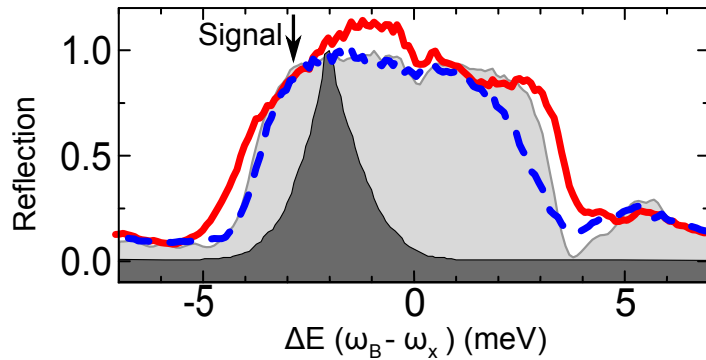


Figure 3.2: The reflectivity stop band of the 200 period BSQW when excited by a right circularly polarized  $\sigma_+$ ,  $14 \mu\text{J}/\text{cm}^2$ , 1 ps control pulse (spectrum of the control pulse indicated by the shaded dark gray area) as measured by a broadband signal pulse (21 meV, spectrally centered at the position of the arrow) having the same circular polarization,  $\sigma_+$ , (solid red line) and the opposite circular polarization,  $\sigma_-$ , (dashed blue line). The measured reflectivity stop bands without the control for both  $\sigma_+$  and  $\sigma_-$  polarizations are indicated by the light gray shaded area.

The basic switch operation can be understood in terms of a circular dichroism and birefringence that is induced in the BSQW sample by the circularly polarized control pulse as illustrated in Fig. 3.2. For these measurements, the analyzer shown in Fig. 3.1(b) is removed, and the polarizer replaced by the quarter wave plate. The change in the reflection stop band that is induced by the right circularly polarized ( $\sigma+$ ) control pulse is spectrally resolved *after* the switch using a broadband probe pulse that has either the same ( $\sigma+$ ) or opposite ( $\sigma-$ ) circular polarization. As 0ps signal-control delay ( $\tau = 0$ ), the change in reflectivity over the spectral range of the signal pulse (centered on the arrow in Fig. 3.2) is clearly much larger for a  $\sigma+$  polarized pulse than for a  $\sigma-$  polarized pulse. Consequently, the  $\sigma+$  component of the linearly polarized signal pulse used in Fig. 3.1(b) is reflected with a different amplitude and phase than the  $\sigma-$  component. As a result, the polarization state of the reflected light changes (i.e. the orientation and ellipticity of the pulse may change as was shown in Sec. 2.10.2), and some of it is transmitted by the polarizer (i.e., the switch is turned on).

The origin of the circular dichroism and birefringence in the reflectivity of the stop band illustrated in Fig. 3.2 can be understood heuristically in terms of the circular selection rules for the  $1s-hh$  excitonic transition in III-V semiconductor quantum wells, as described in Sec. 2.3. Right (left) circularly polarized light  $\sigma+(\sigma-)$  couples to the “spin-down” (“spin-up”) transition. When the frequency spectrum is restricted sufficiently close to the  $hh$  resonance, transitions to other excited states can be ignored.

The photonic band structure in BSQW (and, therefore, the reflectivity stop band) can be attributed to the periodically spaced  $hh$  excitonic resonances. As such, the band structures for the two circular polarization components ( $\sigma\pm$ ) are effectively decoupled (in the absence of many-body effects), and in this regime, the  $\sigma-$  polarized control pulse would be expected to couple to (and to distort) the

spin-down stop band, but not the spin-up band. This simplified description seems to work well for excitation frequencies below the  $hh$  resonance; however, for the frequencies above  $\omega_x$ , the data shows coupling between the two bands.

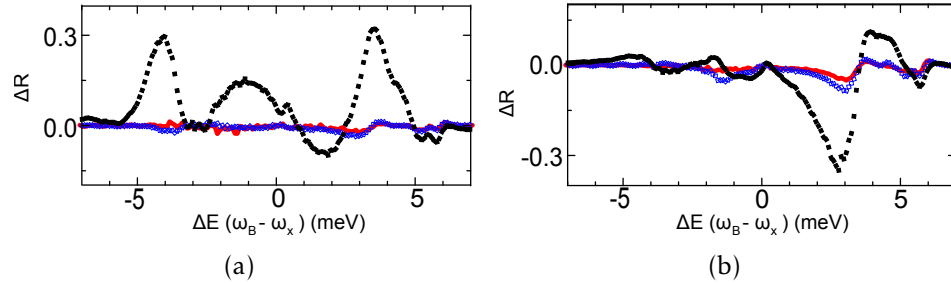


Figure 3.3: The differential reflectivity for control and signal pulses with same (a) and opposite (b) circular polarizations, for signal-control time delays of  $\tau = 0$  ps (solid, black squares),  $\tau = +10$  ps (solid, red line), and  $\tau = -10$  ps, (dashed, blue line). All energies are plotted relative to the  $hh$  exciton resonance,  $E_x = 1.4994$  eV.

---

Reproduced with permission from Ref. [1]

The complete recovery of the reflectivity stop band (and, therefore, of the switch) is illustrated by the differential reflection spectra at  $\tau = \pm 10$  ps in Fig. 3.3. The differential reflectivity for both  $\sigma+$  and  $\sigma-$  is zero for both  $\tau = \pm 10$  ps, indicating the complete recovery of the reflectivity stop band on these timescales. It is tempting to reach this conclusion from an inspection of the pulse-width-limited switching speed shown in Fig. 3.1(b); however, the complete recovery of the contrast ratio does not necessarily imply complete recovery of the stop band. For example, the decay of the induced circular birefringence and dichroism adiabatically could follow the control pulse, but leave identical, but significant, reflectivity changes for both  $\sigma+$  and  $\sigma-$  induced by real carriers induced by either virtual carriers scattered into real states through exciton-phonon processes or real carriers generated through two photon processes. Such a scenario would result in a pulse-width-limited switching time, but a persistent reflectivity change for each

circular polarization. The data in Fig. 3.3 demonstrate that this is not the case.

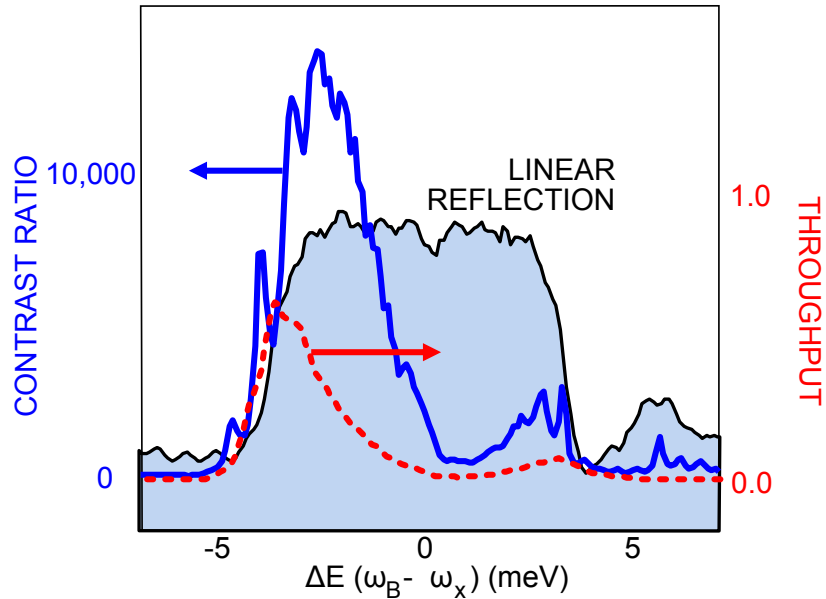


Figure 3.4: Spectrally resolved contrast ratio (solid blue line) and throughput (dashed red line) for the  $14 \mu\text{J}/\text{cm}^2$  1 ps control pulse used in Fig. 3.1(b) and 3.3 and shown in Fig. 3.2 at  $\tau = 0\text{ps}$ . Spectra were taken using the experimental geometry shown in the inset to Fig. 3.1(b)(inset) and a spectrally broad signal pulse (21 meV). The linear reflectivity stop band is shown for reference (shaded area).

---

Reproduced with permission from Ref. [1]

Finally, an optical bandwidth of  $\approx 2.5$  meV (FWHM of the throughput) is measured for the switch shown in Fig. 3.4 by spectrally resolving the contrast ratio and throughput using a spectrally broad (21 meV) signal pulse.

### 3.1.2 80K All-optical polarization switch

While all-optical switching performance in BSQWs at 10K is impressive, technological applications are ultimately limited by its low temperature operation. Ideally this temperature would be raised to room temperature operation. However, absorption in the substrate materials used for these BSQWs at room

temperature makes such experiments difficult. As such, these experiments have been performed to investigate changes to switch performance that occur when raising the BSQW sample temperature from 0K to 80K.

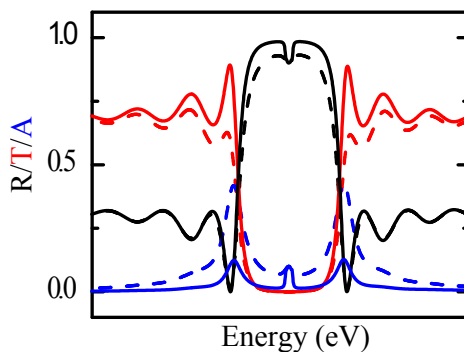


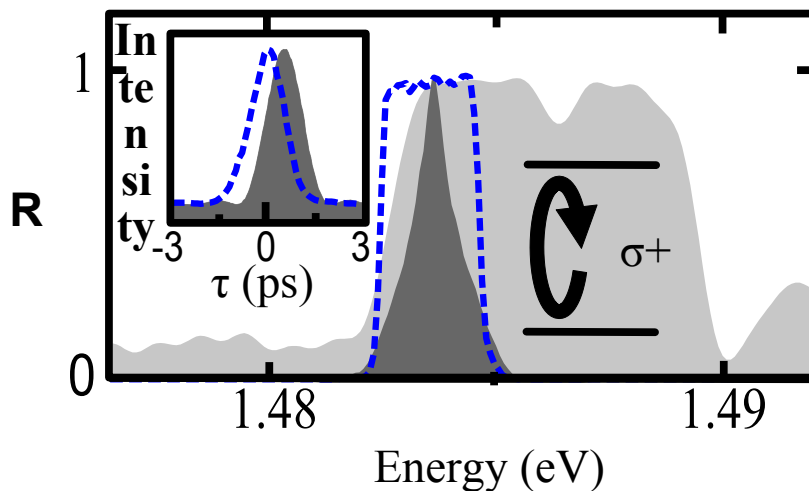
Figure 3.5: Simulated reflection (black), absorption (blue), and transmission (red) from a BSQW with two different exciton dephasing rates (0.1 meV solid, 0.5 meV dashed) (see Ref. [2]).

---

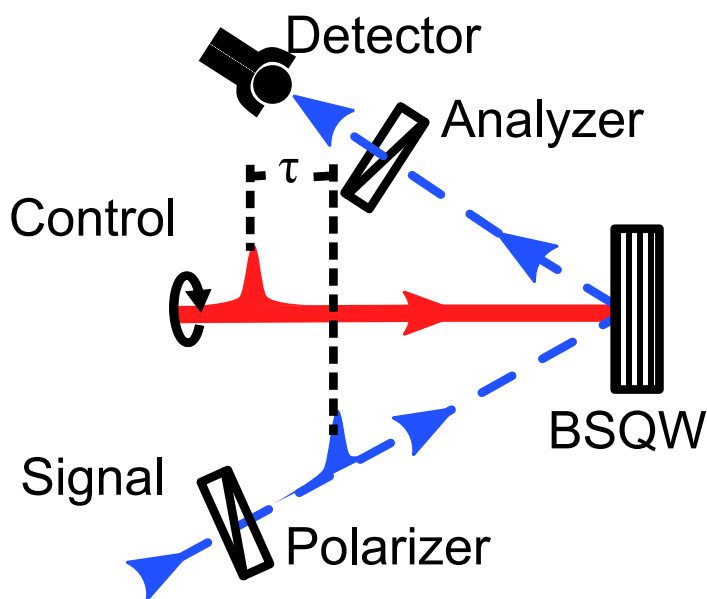
Reproduced with permission from Ref. [3]

Raising the temperature of the structure from 10 K [1] to 80 K should result in increased dephasing due to exciton-phonon interactions, which will round the photonic bandgap and increases the absorption near its edges (compare solid to dashed lines in Figs. 3.5). [34] This behavior is a consequence of increased homogeneous broadening of the underlying exciton resonance with increased temperature, extending the exciton absorption tail outside the photonic bandgap.

Here, polarization switching is demonstrated using the same 200-period  $\text{In}_{0.04}\text{Ga}_{0.96}\text{As}/\text{GaAs}$  sample used to display switching at 10 K, [1] this time cooled to 80 K in a closed cycle cryostat. In addition, whereas the previous switching measurements used broadband signal pulses spectrally resolved after the sample, in these experiments the signal pulse is spectrally shaped to  $\approx 1\text{ps}$  bandwidth before the sample (see Fig. 3.6(a)), and an integrating detector was used to determine the contrast ratio and throughput after the sample. This



(a)



(b)

Figure 3.6: Setup for all-optical switching in Bragg-spaced quantum wells at 80K. (a) Linear reflection (light gray shading) of the reflection stopgap. Dark gray shading shows the spectral position of the control used for high temperature switching measurements. Spectral shape of the signal is shown by the blue dashed line. Inset shows the temporally resolved signal (blue dashed line) and control (dark gray shaded) pulses with an 80 fs gating pulse. (b) Experimental setup for high temperature switching.

should produce results that simulate more accurately the actual environment of a switching device.

The control [ $8 \mu\text{J}/\text{cm}^2$ , 1.3 meV, 1.2 ps (full-width at half maximum, FWHM)] and signal [ $15 \text{ nJ}/\text{cm}^2$ , 2.3 meV, 1.2 ps (FWHM)] pulses are obtained by splitting and separately shaping pulses [80 fs (FWHM)] from a mode-locked Ti:Sapphire laser (see Fig 3.6(a)). The two pulses are spatially overlapped on the sample's surface and a controllable time delay ( $\tau$ ) is introduced between them (see Fig.3.6(b)).

Prior to investigating the switch performance, the spectral position of the control pulse is optimized by measuring the distortion of the reflection stopgap as a pump pulse is tuned across the band, as shown in Fig. 3.7. For these measurements, an unshaped, broadband probe pulse [ $88 \text{ nJ}/\text{cm}^2$ , 27 meV, 80 fs (FWHM)] with the same circular polarization ( $\sigma+$ ) as the pump is spectrally resolved after the sample to investigate changes seen in the reflection direction (i.e. the pulse shaper, polarizer, and analyzer in Fig. 3.6(b) were removed). The results for selected pump-probe delays ( $\tau = -10, 0, +10$  ps) are shown in Fig. 3.7. The distortions of the bandgap (i.e., the nonlinearities) are smallest when the control is tuned below the stop band, and become larger as it is tuned higher in the band. However, as the control is moved to higher energies, the sample recovery becomes slower and/or less complete (as shown by comparison of the reflection at  $\pm 10$  ps). Consequently, Fig. 3.7 suggests that contrast ratio can be traded for sample recovery, and vice versa. In addition, control pulses placed further within the bandgap, but not above it, seem to produce smaller nonlinearities. This is mostly likely due to high reflectivity of the structure reducing the coupling of the pump pulse into the structure. For the switching measurements, we choose the pump position as shown in Fig. 3.7(c). This detuning produces a large distortion of the stop band, but also allows a high degree of sample recovery.

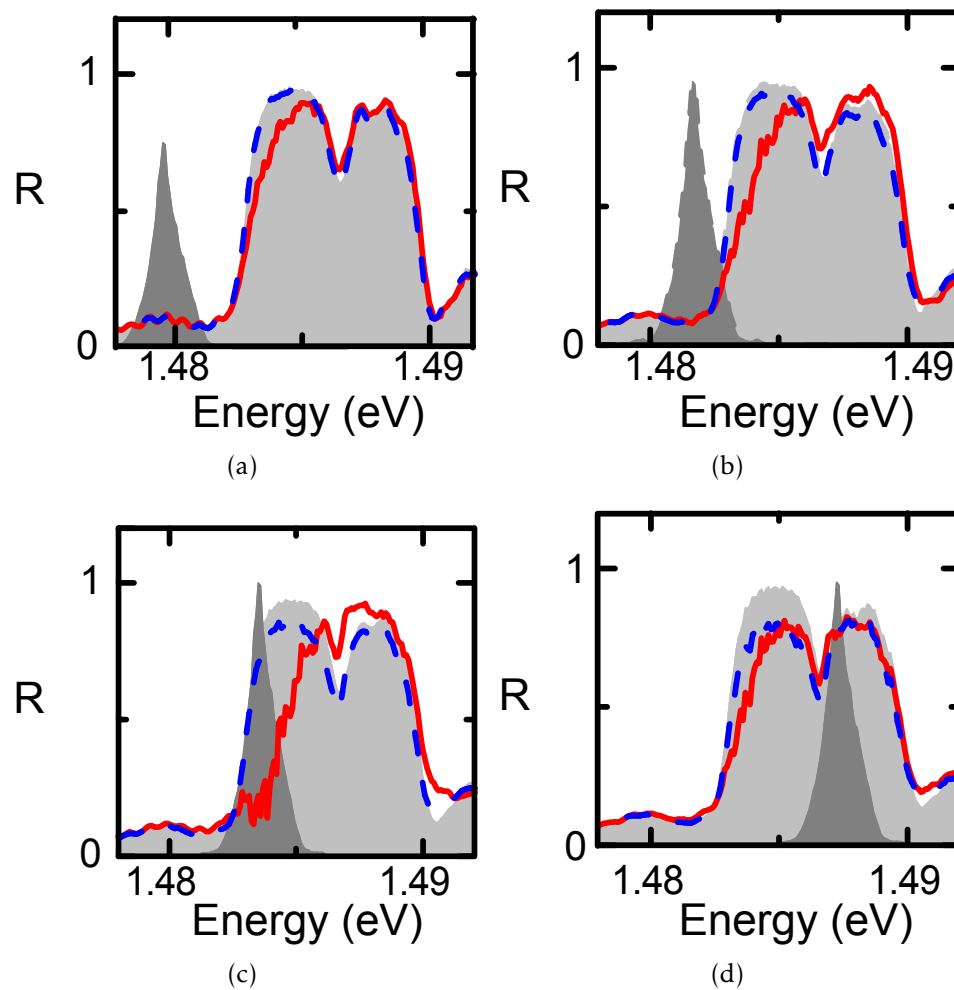


Figure 3.7: Reflection of a broadband,  $\sigma^+$  polarized probe pulse (27 meV, 80 fs) as a function of  $\sigma^+$  pump spectral position (dark shaded area, 1.3 meV, 1.2 ps). Reflection was measured at pump-probe delays of  $-10$  ps (light shading),  $0$  ps (red, solid) and  $+10$  ps (blue, dashed) in each case.

Reproduced with permission from Ref. [3]

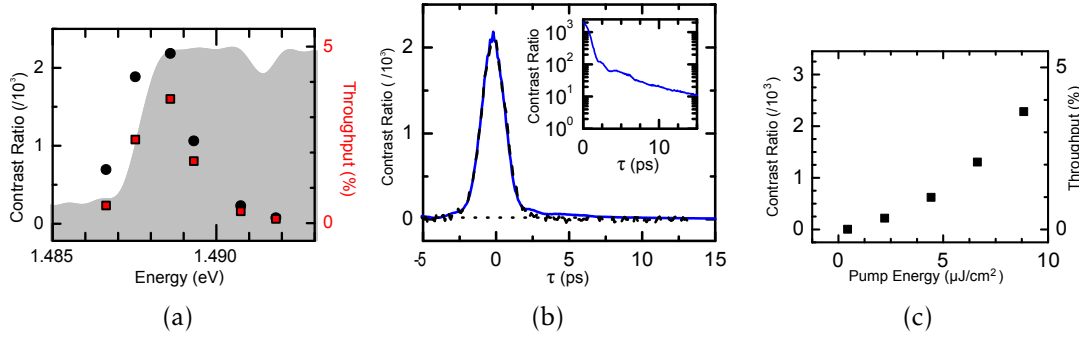


Figure 3.8: Performance of all-optical switching in Bragg-spaced quantum wells at 80K. (a) Maximum recorded contrast ratio (solid circles) and throughput (red squares) as a function of center signal frequency. Linear reflection from the BSQW is shown in light shading. (b) Measured contrast ratio vs. control-signal time delay (blue, solid) and control fluence (c) at the spectral position showing maximum contrast ratio in (a). The dotted line in (b) indicates a contrast ratio of 1 (switch off). Control-signal cross correlation is shown in (b) for reference (black, dashed). Inset in (b) shows the contrast ratio plotted on a logarithmic scale. (c) also lists the corresponding throughput for each control fluence.

---

Reproduced with permission from Ref. [3].

The switch performance is summarized in Fig. 3.8. Figure 3.8(a) shows the contrast ratio and throughput of the switch as the signal pulse is spectrally stepped across the low energy edge of the bandgap. A maximum contrast ratio of 2200 : 1 (33 dB) is measured, with a corresponding throughput of  $\approx 4\%$ , and an optical bandwidth of 0.6 THz. As shown in Fig. 3.8(b), the switch signal closely follows the signal-control cross correlation, indicating a control-pulse-width-limited response; however, a small residual circular anisotropy remains after the control pulse exits the sample, as shown in the inset. The fluence dependence of the contrast ratio and throughput are plotted in Fig. 3.8(c). No saturation is observed, and the quadratic increase in throughput and contrast ratio with increasing control fluence is consistent with the quadratic dependency one expects for a  $\chi^{(3)}$  response.

To investigate the recovery of the switch, the analyzer and polarizer in

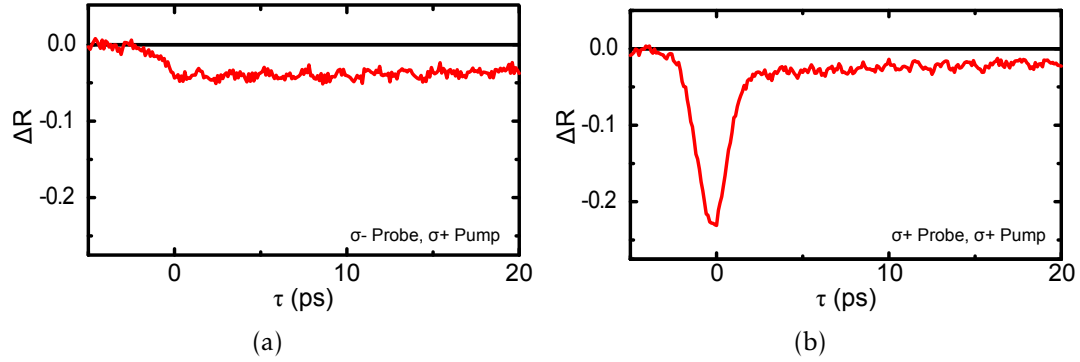


Figure 3.9: Differential reflection vs. pump-probe time delay for the spectrally narrow probe pulse shown in Fig. 3.7. Probe with the opposite (same) circular polarization as the pump is shown in part (a) (part (b)).

---

Reproduced with permission from Ref. [3]

Fig. 3.2 are removed, and time-resolved differential reflection measurements are performed using probe pulses with the same ( $\sigma^+$ ) and opposite ( $\sigma^-$ ) circular polarizations as the pump pulse ( $\sigma^+$ ). The spectral characteristics of the pump and probe (bandwidth and central frequency) are the same as used for peak switching in Fig. 3.8. The results are shown in Fig. 3.9. As expected, during the pump pulse, the reflection changes induced in the spin-down band (which are interrogated by  $\sigma^+$ ) are much larger than those induced in the spin-up band (interrogated by  $\sigma^-$ ). At positive delays, the sample recovers substantially, but not completely, due to residual carriers that remain. While residual carriers have lost interband coherence, they typically retain spin coherence for tens of picoseconds in these materials [103]. As a result, a small circular anisotropy also persists which results in incomplete switch turn off[93], as we also observe in the inset to Fig. 3.8(b).

Summarizing, we have constructed a spin-based polarization switch from a degenerate BSQW structure in which the Bragg resonance is approximately equal to the excitonic resonance, and investigated two temperature regimes. At 10K the switch demonstrates a high contrast ratio (40 dB or higher), pulse width-limited

switching times (into the ps regime) and complete pulse width-limited sample recovery, while dramatically increasing throughput (from 1% to 40% in one case, to 7.5% in the other), significantly reducing switching energies (from  $100 \mu\text{J}/\text{cm}^2$  to  $14 \mu\text{J}/\text{cm}^2$ ) over previous switching materials.

At 80K, switch performance is decreased [1], but still exhibits the same large optical bandwidth, large contrast ratio, modest throughput, and fast switching times with relatively low control fluences. The contrast ratio shows no indication of having saturated. Control intensity could be raised to further improve the contrast ratio and throughput, but at the cost of increased carrier generation. In addition, complete recovery of the sample is possible at 80K if the control is moved below the band edge, although with decreased contrast ratio and throughput.

Ideally this temperature would be raised to room temperature operation. While both of these demonstrations point the way towards a room temperature switch, the degradation in performance seen at 80K will likely be more pronounced. Additional issues with creating room temperature structures are discussed in Sec. 4.2.

### 3.2 Slow light and optical buffers using Bragg-spaced quantum wells<sup>2</sup>

Materials engineered to have small, tunable group velocities ( $v_g = \frac{\partial\omega}{\partial k} = \frac{c}{n_{\text{group}}}$ ,  $n_{\text{group}} = n + \omega_0 \frac{\partial n}{\partial \omega}$ ) are attractive for applications that require pulses or pulse packets to be spatially compressed and stored for a continuously variable time (e.g., optical buffers). In this section, passive tuning of slow light is demonstrated in  $\text{In}_{0.025}\text{Ga}_{0.975}\text{As}/\text{GaAs}$  BSQWs. BSQWs are attractive for slow light applications because they can be fabricated from technologically important semiconductor materials [34], making them compact and potentially integrable with optoelectronic systems. In addition, schemes have been proposed for

---

<sup>2</sup>Much of this section is reproduced with permission from Ref. [99].

stopping, storing and releasing light pulses using BSQWs [38, 2].

As was previously discussed in Sec. 2.7, the presence of two characteristic frequencies that are approximately equal to one another in BSQWs breaks the photonic bandstructure into three bands, as illustrated in Fig. 3.10. The photonic band structure (shown in Fig. 2.9(a) and in Fig. 3.10(b)) was previously shown to have the analytic form (Eq. 3.1 [38]):

$$\cos(ka) = \cos(qa) + \frac{\Gamma}{(\omega + i\gamma) - \omega_X} \left( \frac{\omega}{\omega_X} \right) \sin(qa) \quad (3.1)$$

where  $\Gamma = \frac{|\tilde{\phi}(0)|^2 |\wp|^2 \omega_X}{2\epsilon_0 n_b \hbar c}$  is the radiative decay rate of the transition,  $\tilde{\phi}(\vec{r} = 0)$  is the exciton wavefunction, with electron and hole separation given by  $\vec{r}$ ,  $\wp$  the dipole moment,  $n_b$  the background index of the BSQW material,  $\omega(k)$  is the polariton angular frequency (wavevector),  $q = n_b \omega / c$  is the wave vector of the photon (assumed here to be in the z-direction), and  $\gamma$  the dephasing decay rate. The simulation in Fig. 3.10 uses material parameters appropriate for an  $\text{In}_{0.025}\text{Ga}_{0.975}\text{As}/\text{GaAs}$  BSQW [34]:  $\hbar\omega_B = 1.491$  eV,  $\hbar\omega_x = 1.494$  eV,  $\Gamma = 30\mu\text{eV}$ ,  $\gamma = 0.15$  meV, and  $n_b = 3.61$ .

The width of the intermediate band (IB),  $\Delta\omega_{\text{IB}}$ , and the  $v_g$  associated with it are each proportional to the relative detuning  $|\omega_B - \omega_x|$  [2, 38]. Thus, the speed of light in a BSQW can be varied and controlled either by engineering the photonic bandstructure (e.g., controlling the well width or spacing during growth) to produce a given  $|\omega_B - \omega_x|$  or by shifting  $\omega_B$  and/or  $\omega_x$  externally following growth.

Expanding Eq. 3.1 for  $\omega_B \approx \omega_x$ , an expression for  $\omega(k)$  and the group velocity,  $v_g$ , can be written [4]:

$$\omega - \omega_B = \frac{1 + \cos(ka)}{1 + \cos(ka) + \pi\Gamma/\omega_X} [\omega_x - i\gamma - \omega_B] \quad (3.2)$$

$$v_g = \frac{\partial\omega}{\partial k} = \left| \frac{\pi\Gamma\omega_X \sin(ka)}{(1 + \cos(ka) + \pi\Gamma/\omega_X)^2} (\omega_x - \omega_B) a \right| \quad (3.3)$$

In addition, using values of  $k = 0$  and  $\pi$  in Eq. 3.2, one finds the width of the

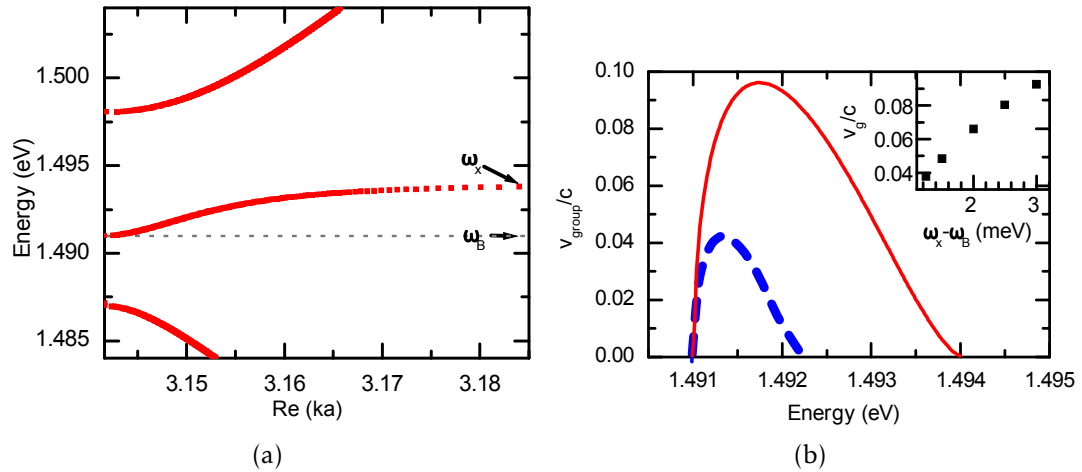


Figure 3.10: Simulations of slow light in Bragg-spaced quantum wells. (a) Simulated bandstructure of a detuned ( $\Delta\omega = \omega_B - \omega_x = -3.0$  meV), Bragg-spaced quantum well structure with unit cell parameters chosen to match those of  $\text{In}_{0.025}\text{Ga}_{0.975}\text{As}/\text{GaAs}$  quantum wells:  $\omega_B = 1.491$  eV,  $\omega_x = 1.494$  eV,  $\Gamma = 30\mu$  eV the radiative damping rate,  $\gamma = 0.15$  meV the dephasing rate, and  $n_b = 3.61$ . (b) Simulated group velocity of a Bragg-spaced quantum well structure at two detunings,  $\Delta\omega = \omega_B - \omega_x = -3.0$  meV (red, solid) and  $\Delta\omega = -1.25$  meV (blue, dashed). By varying the detuning  $\Delta\omega$ , the group velocity of the pulse is continuously tunable (inset).

---

Reproduced with permission from Ref. [4].

intermediate band:

$$\Delta\omega_{\text{IB}} = \frac{2}{2 + \pi\Gamma\omega_X}(\omega_X - \gamma - \omega_B) \quad (3.4)$$

In the limit of small  $\varphi$  and  $\gamma$  then, this reduces to  $\Delta\omega_{\text{IB}} = |\omega_B - \omega_X|$ , and  $v_g \propto \Delta\omega_{\text{IB}}$ . Figure 3.10 shows  $v_g$  as a function of photon energy for two  $\Delta\omega_{\text{IB}}$ :  $-3.0$  meV (corresponding to the IB in Fig. 3.10) and  $-1.25$  meV. The inset shows the variation of the maximum  $v_g$  versus  $\Delta\omega_{\text{IB}}$ .

Clearly, the group velocity can be made arbitrarily small by narrowing the IB. In fact, when  $\Delta\omega_{\text{IB}} = 0$  and  $\gamma = 0$ , the IB is flat,  $v_g = 0$  and no propagation is allowed. Of course, if the IB is narrowed to a bandwidth less than that of the incident pulse, spectral narrowing (temporal broadening) of the transmitted pulse will occur. The time delay  $\tau_{\text{delay}}$  that is possible without spectrally narrowing the input pulse can be readily estimated using the approximate expression given for the maximum  $v_g$  in Ref. [38]:

$$\tau_{\text{bit}} \equiv \tau_{\text{delay}}/\delta t \cong \frac{8N}{9} \sqrt{\frac{3\Gamma}{2\pi\omega_X}} \quad (3.5)$$

where  $N$  is the number of quantum wells in the BSQW and where we have assumed that the full width half maximum (FWHM) temporal width  $\delta t$  of the input pulse is inversely proportional to the intermediate bandwidth ( $1/\Delta\omega_{\text{IB}} = \delta t/2\pi$ ). The bit delay depends only on the oscillator strength and number of wells. Using parameters appropriate for GaAs ( $\Gamma/\omega_X \approx 2 \times 10^{-5}$ ) and the number of wells in the samples described below ( $N = 210$ ), one would expect  $\tau_{\text{bit}} = 0.6$ .

To illustrate slowing of light in BSQWs, we use an  $N = 210$   $\text{In}_{0.025}\text{Ga}_{0.975}\text{As}/\text{GaAs}$  BSQW grown by MBE. The layer thicknesses were systematically wedged by not spinning the sample during growth as described in Sec. 2.5.

Figures 3.11(a) and 3.11(b) show, respectively, the simulated and measured reflection ( $R$ ), transmission ( $T$ ), and absorption ( $A = 1 - R - T$ ) of the BSQW for a detuning  $\Delta\omega = -3.3$  meV. Experimentally, detuning is determined by mapping layer thicknesses, measured directly by x-ray diffraction, as a function

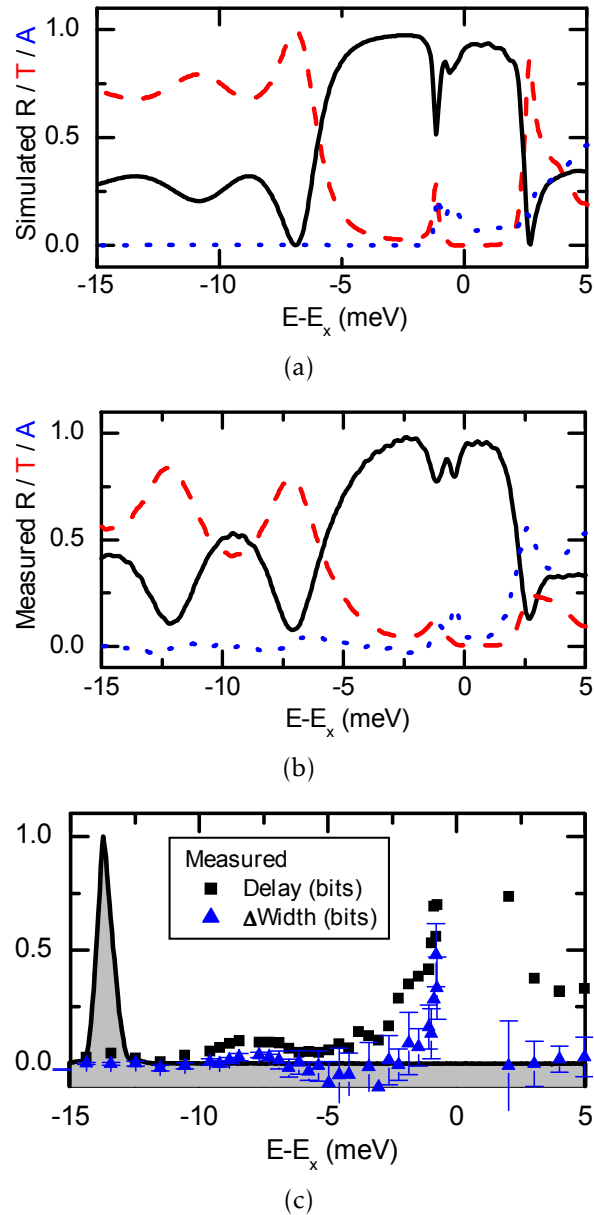


Figure 3.11: Spectrally resolved slow light in Bragg-spaced quantum wells. (a) Simulated reflection (black, solid) from, transmission (red, dashed) through, and absorption (blue, dotted) by an  $N = 210$  Bragg-spaced  $\text{In}_{0.025}\text{Ga}_{0.975}\text{As}/\text{GaAs}$  quantum well structure. (b) Low temperature measurements (10K) on the corresponding experimental structure. (c) Measured relative delay (black, square) and pulse broadening (blue, triangle) of a 0.67 meV (3.5 ps) pulse, shown for reference in black/gray fill.

Reproduced with permission from Ref. [4].

of position on the sample surface, and confirmed with numerical simulations of the spectra. Measurements are performed with the sample mounted in a cryostat cooled to 10K. Simulations are performed using a transfer matrix method. Good quantitative agreement can be seen between simulations in Fig. 3.11(a) and experiment in Fig. 3.11(b). Deviations can be explained by disorder in the quantum well periodicity [4].

Both experiment (Fig. 3.11(b)) and simulation (Fig. 3.11(a)) show an  $\approx 8$  meV-wide high reflectivity stop band associated with the forbidden photonic bandgap. The IB is visible in the middle of the stop band and has a bandwidth approximately equal to the detuning  $\Delta\omega = -3.3$  meV. However, the reflectivity (transmission) decrease (increase) is small, and oscillations in the reflectivity appear within the IB. These non-ideal features are caused by Fresnel reflections at the front surface associated with the effective index of the BSQWs, resulting in poor coupling efficiency of the light into the IB and an incomplete reduction in the reflectivity, rather than a well-defined allowed transmission window. In addition, Fresnel reflections at the air/BSQW and BSQW/substrate interfaces lead to Fabry-Perot fringing, and account for the reflectivity oscillations seen within the IB.

The group velocity and group velocity dispersion of pulses propagating through the BSQW shown in Figs. 3.11(a) and 3.11(b) are investigated by measuring the delay and broadening of a weak ( $88 \text{ nJ/cm}^2$ ) 3.5 ps pulse transmitted through the sample. The incident pulses are obtained by using a pulse shaper to spectrally narrow (to 0.67 meV) pulses from a mode locked Ti:Sapphire laser, and attenuating the pulse intensity to ensure linear transmission through the material. The time delay and width of each transmitted pulse are measured by cross correlating the transmitted pulse with an 80 fs reference pulse using second harmonic generation in a  $\beta$ -barium borate (BBO) crystal. This measurement is repeated as the frequency is tuned across the entire photonic band structure.

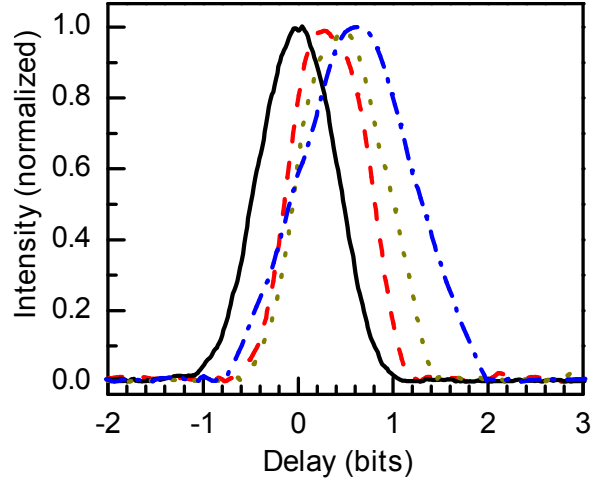


Figure 3.12: Measured temporally-resolved 0.67 meV, 3.5 ps pulses transmitted through the experimental structure of Fig. 3.11. Pulses were centered on photon energies  $E - E_x = -0.79$  meV,  $-1.08$  meV,  $-2.26$  meV,  $-11.51$  meV for the blue dash-dot line, the dark yellow dotted line, the red dashed line, and the black solid line, respectively. Delays are relative to the transmitted pulse at  $-11.51$  meV.

---

Reproduced with permission from Ref. [4].

The relative delay (compared to the delay of a pulse with center frequency below the reflectivity stop band) and broadening of each transmitted pulse are shown in Fig. 3.11(c). Near the low energy edge of the IB, time delays dramatically and continuously increase to  $\approx 0.4$  bits (1 bit=3.5 ps), corresponding to  $v_g \approx 0.067c$ , with little pulse broadening and  $\approx 10\%$  transmission. In this regime, the pulse delay can be continuously tuned either by tuning the wavelength of the incident pulse or actively shifting the position or width of the IB (not shown). From measurements in this region, we estimate the pulse time delay-bandwidth product to be  $\approx 0.2$ . This time delay-bandwidth product compares favorably with slow light reports in semiconductors based on other mechanisms such as coherent population oscillations ( $\approx 0.04$ ) [104, 105].

As the pulse is tuned closer to the excitonic resonance, the group velocity is further reduced, the transmission goes to zero, and the pulse broadening sharply

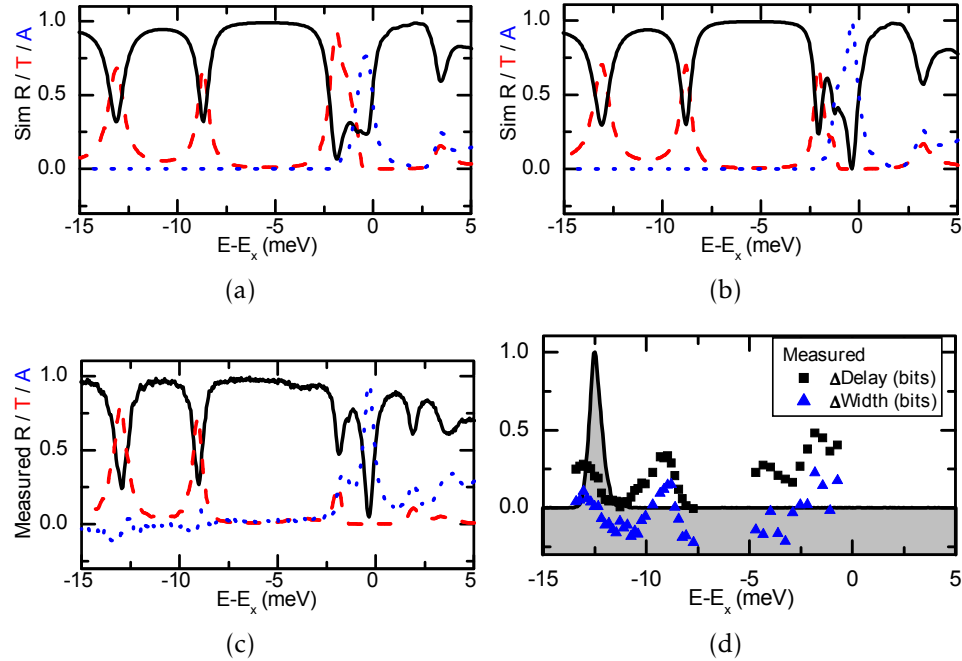


Figure 3.13: Simulation of a Bragg-spaced quantum well sample identical to Fig. 3.11 except with antireflection coatings on the front and exit interfaces designed for (a)  $\Delta\omega = -3.3$  meV and (b)  $\Delta\omega = 22$  meV, including reflection (black, solid), transmission (red, dashed), and absorption (blue, dotted). (c) Measured reflection, transmission, and absorption of an experimental sample with target structure of (a), but actual structure closer to (b). The percentage error in antireflection coating layer thicknesses equals 1.5%. (d) Measured relative delay (black, square) and pulse broadening (blue, triangle) of a 0.67 meV (3.5 ps) pulse, shown for reference in black/gray fill.

---

Reproduced with permission from Ref. [4].

increases. A maximum 0.7 bit delay, corresponding to a group velocity  $\approx 0.038c$ , is observed in the region near the upper edge of the IB band, but the pulse is broadened by  $\approx 0.5$  bit. The continuous tuning of the delay near the band edge and the onset of broadening as the excitonic resonance is approached are illustrated in Fig. 3.12, which shows selected temporally-resolved transmitted pulses centered at different photon energies in the IB.

The less than ideal performance of the BSQW used for the measurements shown in Fig. 3.11(b) can be attributed to the Fresnel reflections and Fabry-Perot

fringing discussed earlier, and in Refs. [38] and [106]. In an attempt to reduce these adverse effects, we grew an identical sample, except that an antireflection (AR) coating was grown on both incident and exit sides. The AR coating consists of 7.5 periods of quarter wave layers ( $l_{\text{Design}}/4n_b$  thick) of GaAs/Al<sub>0.33</sub>Ga<sub>0.67</sub>As, two available (but non-optimal) materials, grown both between the air/BSQW interface and the BSQW/substrate interface. The design wavelength ( $l_{\text{Design}}$ ) was chosen to be close to  $\lambda_B (= 2\pi n_b c/\omega_B)$ , where the group velocity (and group index) is fairly flat (e.g., see Fig. 3.10). Figure 3.13(a) shows simulations of R, T, and A of the target BSQW detuned to  $\Delta\omega = \omega_B - \omega_x = -3.3\text{meV}$ . The simulation shows reduced Fabry-Perot fringing and improved coupling to the IB, i.e. less reflection across the IB.

Figure 3.13(c) (solid lines) shows measurements of R, T, and A of the corresponding experimental structure performed at low temperature (10K). The coupling of light clearly is improved in the AR coated BSQW compared to the non-AR coated structure (Fig. 3.11(b)), with minimum reflection close to zero; however, Fabry-Perot fringing is more pronounced than in the simulated target structure in Fig. 3.13(a). We speculate that the difference between the simulated and grown AR coated BSQW may be due to small errors in the thicknesses of the layers in the AR coating. This sensitivity to errors in the layer thickness is illustrated by the simulation shown in Fig. 3.13(b), where an error in the layer thicknesses of 1.5% has been assumed and which produces significantly better agreement with the experimental result. Improved designs that are less sensitive to small errors in the layer thicknesses can be constructed from materials with more optimal indices of refraction.

The delay and broadening of a 3.5 ps pulse transmitted through the AR coated BSQW using the same procedure as that used to obtain Fig. 3.11(c) are shown in Fig. 3.13(d). While the AR coating improved the coupling and reduced

the fringing of the BSQW, it did not improve the slow light performance. Near the lower edge of the IB, there is a spectral region where the delay is significant ( $\approx 0.25$  bits) and broadening is negligible. Closer to the excitonic resonance, a maximum bit delay of 0.5 is observed, but at the expense of increased broadening of the pulse width ( $\approx 0.2$  bit) and greatly reduced transmission ( $\approx 1\%$ ).

Slow light features are observed in the AR coated BSQW that are not present in the uncoated sample. Below the reflectivity stop band, the AR coating acts like an ordinary Fabry-Perot cavity, i.e., two mirrors separated by the thickness of BSQW structure. Regularly spaced modes of the cavity can be seen to the low energy side of the high reflectivity photonic stop band in Fig. 3.13(c). As expected, the laser pulses are also slowed and broadened by the dispersion associated with the bare cavity modes.

The negative changes in pulse width shown in Fig. 3.13(d) suggest that the pulse is temporally compressed at some photon energies (e.g., midway between cavity modes). This compression of the nearly transform-limited pulses is reproduced by linear transfer matrix calculations, which show that the compression is due to a spectral reshaping of the pulse. When positioned midway between cavity modes, the spectral tails of the pulse are enhanced, while the center of the pulse is attenuated, resulting in a pulse with a spectrally broader and temporally narrower width.

Optimization of the AR coating used in these experiments was not attempted. In particular, Ref. [106] discusses an optimization scheme. In an ideal case of bulk material, AR coatings can be designed using the simple methods described in Sec. 2.6. For a general AR coating consisting of  $N$  layers of width  $\lambda/(2n_j)$  where  $\lambda$  is a particular wavelength of interest, and  $n_j$  is the index of refraction of the  $j^{\text{th}}$

layer, reflection is minimized at  $\lambda$  if [106]:

$$n_0 n_f^{-1^{N+1}} \sum_{j=1}^N n_j^{-2^j} = 1 \quad (3.6)$$

where  $n_0$  ( $n_f$ ) is the index of the incident (substrate) medium.

For BSQW materials,  $n_f$  for the material is not well defined. However, the transfer matrix for light propagation into the wells can be rewritten into a form similar to the transmittance of light into a bulk material (i.e Eq. A.8) [106]:

$$\begin{bmatrix} E_j^+ \\ E_j^- \end{bmatrix} = \begin{bmatrix} \frac{n_{\text{BSQW}}(\omega) + n_{\text{in}}}{2n_{\text{in}}} & \frac{n_{\text{BSQW}}^*(\omega) - n_{\text{in}}}{2n_{\text{in}}} \\ \frac{n_{\text{BSQW}}(\omega) - n_{\text{in}}}{2n_{\text{in}}} & \frac{n_{\text{BSQW}}^*(\omega) + n_{\text{in}}}{2n_{\text{in}}} \end{bmatrix} \begin{bmatrix} E_{j+1}^+ \\ E_{j+1}^- \end{bmatrix} \quad (3.7)$$

where  $n_{\text{in}}$  is the index of the incident medium, and  $n_{\text{BSQW}}(\omega)$  is the effective index of the BSQW system. Using appropriate values for the Bloch function, an effective index for the BSQW material can be found. Far away from the photonic bandgap in these structures, this produces an index  $n_{\text{eff}}/n_b \approx 1$ . However, near to the bandedge, this index begins to blow up and at both the low and high bandedge  $n_{\text{eff}} \rightarrow \infty$ . Inside the intermediate bandgap,  $q$  takes on imaginary values, and there is no effective index describing the material. However, along the intermediate band, real values of  $n_{\text{eff}}$  are small but finite. Using appropriate values for these structures, Yang et. al. predicted  $n_{\text{eff}}/n_b \approx 0.04$ .

In summary, we have measured the slowing and broadening by group velocity dispersion of picosecond pulses propagating in the IB of two  $\text{In}_{0.025}\text{Ga}_{0.975}\text{As}/\text{GaAs}$  BSQWs: one non-AR coated and the other AR coated. Continuously tunable delays from 0 to  $\approx 0.4$  bit were measured with negligible broadening for the non-AR BSQW. Unoptimized AR coatings were shown to improve the coupling of light into the structure. AR coatings fabricated from GaAs and AlGaAs were also found to be sensitive to small errors (1.5%) in the AR coating layer thicknesses. Improved AR coatings using materials with larger differences in their indices of refraction should allow the production of samples with performance nearer the theoretical

limit.

### 3.3 Nonlinearities in Bragg-spaced quantum wells

The potential switching applications of BSQWs presented in Sec. 3.1 rely on the nonlinear optical response of BSQWs, as do the tuning techniques proposed for slow light in BSQWs presented in Ref. [38]. As such, an understanding of the physical processes behind these nonlinearities should be helpful in understanding and optimizing the operation of these devices, as well as providing information about the nonlinear optical response of photonic materials in general. While some research has been done using orthogonal linear pulses to study nonlinearities in BSQWs [86, 102], here pulses with both the same and opposite circular polarizations are used to study the spin-dependent nonlinearities which in particular have been used to demonstrate polarization switching.

#### 3.3.1 Broadband measurements of the nonlinear response

The same  $N=200$   $\text{In}_{0.03}\text{Ga}_{0.97}\text{As}/\text{GaAs}$  BSQW sample used for experiments in Sec. 3.1 is again used here, tuned such that  $\omega_B \approx \omega_x$ , as shown in the linear reflection spectrum in Fig. 3.14(a), and mounted in a closed-cycle He cryostat cooled to 10 K. Pulses from a mode-locked Ti:Sapphire laser were split into pump and probe pulses. The pump pulse was spectrally shaped [1.3 meV, 1 ps, dark shaded area in Fig. 3.14(a)], right-circularly polarized ( $\sigma+$ ) and focused near normal incidence onto the sample. Initially, a spectrally broadband probe pulse was used for these experiments [although similar measurements with a narrowband probe (i.e. spectrally resolved before the sample) will be shown in Sec. 3.3.2]. The weak ( $140 \text{ nJ}/\text{cm}^2$ ) broadband (27 meV FWHM, 80 fs FWHM, spanning the entire reflection bandgap) probe pulse [black dotted line Fig. 3.14(a)] was arranged to be incident at a small angle ( $\approx 10^\circ$ ) with respect to the surface normal of the sample. A quarter wave plate before the sample allowed

measurements to be performed with probe pulses having either the same ( $\sigma+$ ,  $++$  configuration) or opposite ( $\sigma-$ ,  $+ -$  configuration) circular polarization as the pump. The time delay ( $\tau$ ) between the pump and probe pulses was varied, and the signals in the reflection direction [see Fig. 3.14(b)] were spectrally resolved at each pump-probe delay.

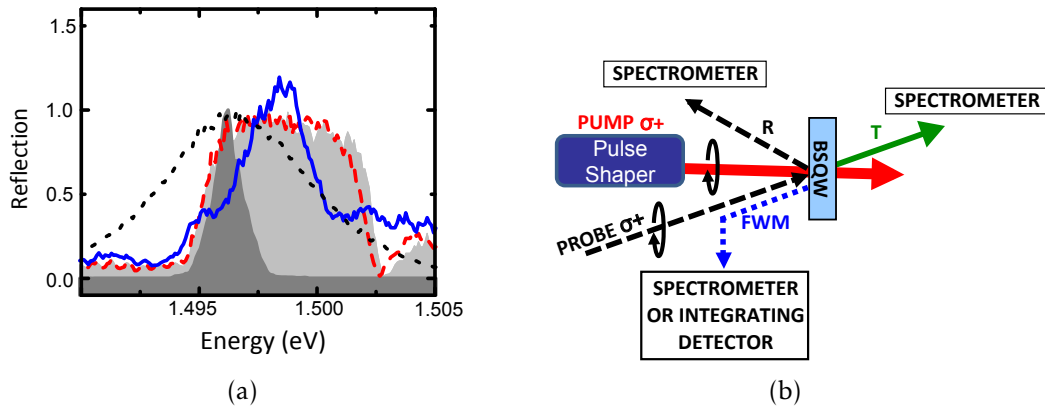


Figure 3.14: Setup for nonlinear measurements. (a) Reflection spectrum of a  $\sigma+$  (blue, solid) and  $\sigma-$  (red, dashed) polarized probe at  $\tau = 0$  ps pump-probe delay for a  $\sigma+$  polarized pump. The linear reflection from the structure is shown in the light shaded area. The pump (dark shaded) and incident probe (black, dotted) spectrums are shown for reference. (b) Schematic experimental setup for nonlinear measurements. A strong  $\sigma+$  polarized spectrally shaped pump (red solid), and weak  $\sigma+$  or  $\sigma-$  polarized probe (black dashed) are incident on the BSQW structure. Signals in both the reflected (R, black dashed line); the backwards probe, background-free four-wave mixing (FWM, blue dotted line); and in the transmission direction (T, green solid line) directions are detected.

Fig. 3.14(a) shows typical reflection measured for both the  $++$  (blue solid), and  $+ -$  configurations (red, dashed) at  $\tau = 0$  ps. While the  $++$  configuration shows a significant distortion of the reflection stopband by the co-polarized pump, the  $+ -$  reflection shows almost no change.

These results have been explained in terms of a simplified model based on the circular selection rules for the  $hh$ -exciton, consisting of two independent

stop bands coupled to  $\sigma_+$  and to  $\sigma_-$  polarized light, respectively (see Sec. 2.3 or Ref. [1]). Namely, a two independent two-level systems model is only valid if higher lying transitions (such as the light hole), and many body effects that couple the systems can be ignored. Many body effects (discussed in Sec. 2.4) can include Hartree-Fock local field corrections and Pauli-blocking, neither of which will couple the two independent spin systems, as well as excitation induced dephasing and biexciton effects, which can couple the two spins. On the low energy edge of the bandgap, because very few changes are seen for the  $+-$  configuration, and large changes occur for the  $++$  configuration (Fig. 3.14(a)), the independent spin-up and spin-down bandgap model seems to hold. On the high energy edge of the bandgap, changes do occur to the spin-down bandgap, and higher lying transitions (such as the light hole) or many body effects (such as bound biexcitons or exciton-exciton scattering) couple the systems.

An expanded view of the reflection vs. pump-probe delay around  $\tau = 0$  is shown as a contour plot in Fig. 3.15 ( $++$  configuration) and Fig. 3.16 ( $+-$  configuration). At negative delays, data taken in the  $++$  configuration in the reflection direction [bottom in Fig. 3.15] shows transient spectral gain [red areas in Fig. 3.15], i.e. reflection  $> 1$ . The gain initially appears on the low energy edge of the photonic bandgap, giving a peak reflection of  $R \approx 1.5$  at  $\tau \approx -1.2$  ps. At the same time, distortions appear in the bandgap, eating out holes in reflection along both its low and high energy edges. As the time delay between the pump and probe decreases, the peak of the gain sweeps toward the middle of the photonic bandgap until it mostly disappears at  $\tau = 0$  ps.

In the  $+-$  configuration (Fig. 3.16), very few changes are seen in reflection. Some small distortions do occur along the high energy edge. These distortions, as mentioned earlier, can be attributed to higher order many body effects, such as bound or unbound biexciton states, and higher lying transitions such as the light

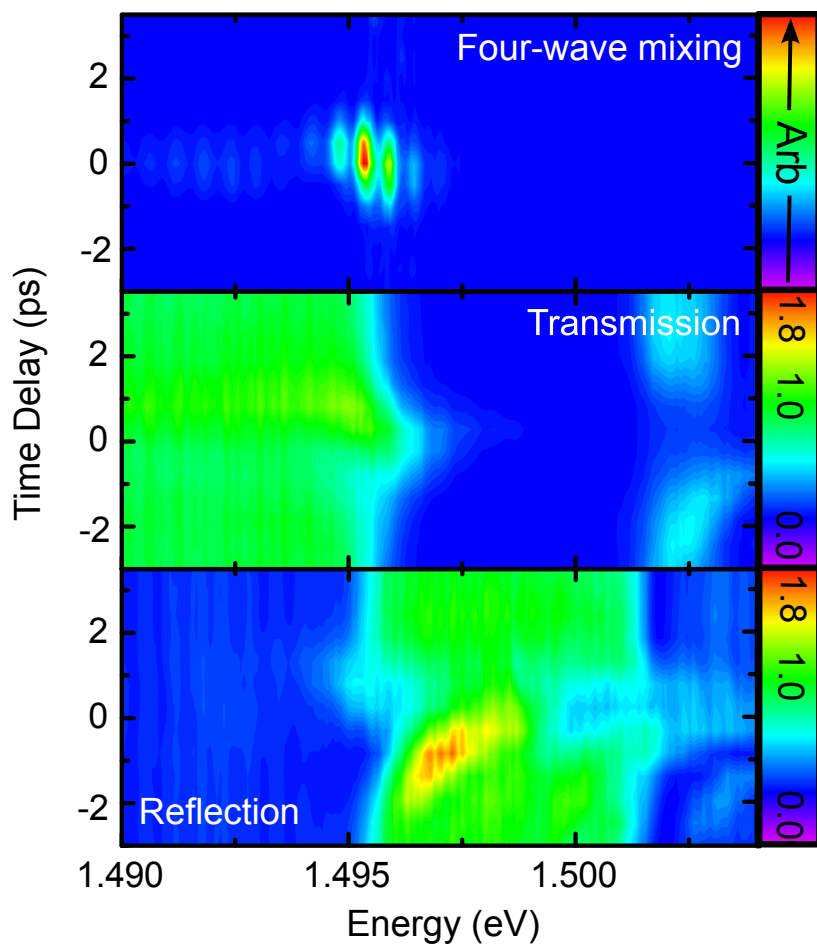


Figure 3.15: Spectrally resolved reflection, transmission and background free signals of a  $\sigma+$  polarized probe at time delays ranging from  $-3\text{ps}$  to  $+3\text{ps}$ .

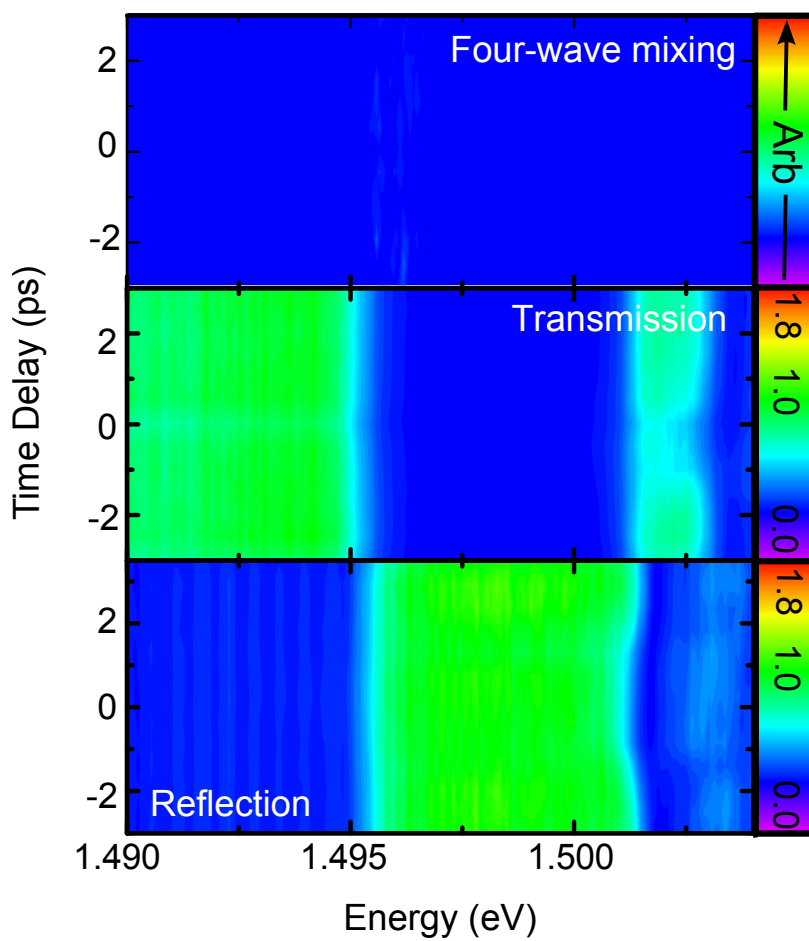


Figure 3.16: Spectrally resolved reflection, transmission and background free signals of a  $\sigma^-$  polarized probe as a function of time delay ( $-3$  ps to  $+3$  ps) with respect to a  $\sigma^+$  pump. Background-free signals are plotted in the same arbitrary units as the background-free signals in Fig. 3.15.

hole, which can weakly couple the spin-up and spin-down excitons.

Also shown in Figs. 3.15 and 3.16 are the spectrally resolved transmitted light as a function of pump-probe delay. In the transmission direction, for the ++ configuration, an increase in energy is seen inside the low energy edge of the bandgap following the temporal shape of the pump pulse. More surprisingly, some slight transient gain appears outside the gap (yellow area), on its low energy edge at positive delays. In the +- configuration, little change is seen in transmission, except along the high energy edge of the bandgap, where higher lying states and higher-order many body effects that couple the spin-up and spin-down transitions are expected to appear.

In addition, some four-wave-mixing (FWM) signals were also spectrally resolved. Recall from Sec. 2.4 that some third-order grating terms travel in the backwards probe, FWM direction, i.e., the induced polarization is proportional to  $|E|^3$ , and has terms of the form:

$$|E|^3 \propto E_{\text{probe}}^* E_{\text{pump}} E_{\text{pump}}^* e^{-i[(\omega_{\text{pump}} - \omega_{\text{probe}} + \omega_{\text{probe}})t + (k_{\text{pump}} - k_{\text{pump}} + k_{\text{probe}})z]} + \dots \quad (3.8)$$

$$= E_{\text{probe}}^* E_{\text{pump}} E_{\text{pump}}^* e^{-i(\omega_{\text{probe}}t + k_{\text{probe}}z)} + \dots \quad (3.9)$$

Because fields traveling in this direction only begin to appear in third order, they provide a simpler view of third order processes than, for instance, the reflection direction, where both first order and third order terms interfere. To investigate fields traveling in this direction, a beam splitter was inserted into the probe before the sample (see Fig. 3.14(b)), and the fields were both spectrally integrated (Fig. 3.17) and spectrally resolved (top in Fig. 3.15 and 3.16) as a function of pump-probe delay.

In the ++ configuration, a signal is seen in the FWM direction centered at  $\tau = 0$  ps pump-probe delay. This FWM is centered on the pump spectral position used for these experiments, likely because that is the position where gratings formed between the pump and probe pulses are moving their slowest (i.e.  $\omega_{\text{pump}} - \omega_{\text{probe}} \approx$

0), and the material response can most closely follow them. The fringing shown in Fig. 3.15 is due to the beam splitter used to pick off the background signal. No signals are seen traveling in the FWM direction in the  $+ -$  configuration.

The presence of transient spectral gain raises questions as to the processes responsible for its appearance. It has been recently proposed that BSQWs could act as amplifiers under some conditions due to polariton interactions beyond third order [107].

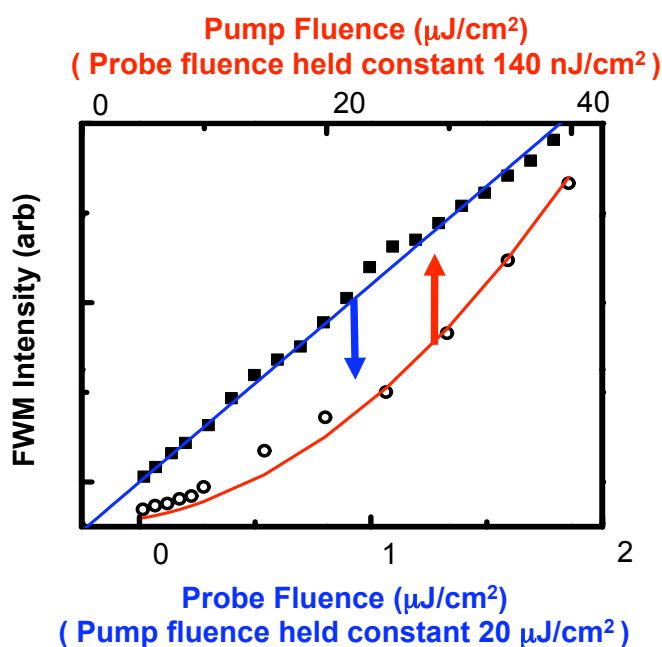


Figure 3.17: Intensity of the background-free four-wave-mixing (FWM) signal versus pump intensity (round, hollow), and probe intensity (square, solid). Fit lines (red, quadratic for the pump and blue, linear for the probe) are shown for reference.

Integrated FWM in Fig. 3.17 shows the dependence of the signal traveling in this background-free direction on both pump and probe fluence. The FWM signal shows a quadratic dependence on pump fluence (open circles) and a linear dependence on probe fluence (closed squares), indicating a nonlinear regime third order in the optical field as opposed to the (beyond third order) mechanism

proposed in Ref. [107]. The origin of the transient gain seen here is then likely a four-wave mixing process, and not due to polariton interactions beyond 3rd order.

To further investigate the transient gain, which appears in both reflection and transmission, it is helpful to examine what is being measured in these experiments. It is common to describe the linear properties of a material in terms of its reflection ( $R$ , fraction of the incident energy that is reflected from the material), transmission ( $T$ , fraction of the incident energy that is transmitted through the material), and absorption ( $A$ , fraction of the incident energy stored inside the material). Energy conservation requires that (in the absence of extreme scattering effects at the materials surface) the sum of these contributions account for all the incident energy (i.e.  $R + T + A = 1$ ).

In nonlinear interactions, this may not be the case. Energy conservation should still hold, but must now include the sum of all the optical energy traveling in:

1. the probe's reflection ( $E_{R,\text{probe}}$ ) and transmission ( $E_{T,\text{probe}}$ ) directions,
2. the pump's reflection ( $E_{R,\text{pump}}$ ) and transmission ( $E_{T,\text{pump}}$ ) directions,
3. four-wave mixing directions ( $E_{\text{FWM}}$ , typically small when compared to energy traveling in the reflection or transmission directions), and
4. any energy absorbed by the material ( $E_A$ ).

The total energy traveling in just (1) (the probe's reflection and transmission directions) may increase if energy is scattered from the pump beam into these directions.

When spectrally resolving the reflected and transmitted pulses, additional complications arise in this model. Namely, light scattered by the grating may have time dependent phase shift and thus see spectral redistribution. This will

result in more energy at a given wavelength than was present in the incident pulse. Spectrally integrated measurements avoid the complication of probe redistribution and thus provide a cleaner picture of the occurrence of transient energy transfer.

Numerically integrated differential reflection (blue, hollow circles) and differential transmission (red, solid squares) are shown in Fig. 3.18. These numerical integrations were calculated using an integral of the signals seen in the reflection/transmission direction divided by the integrated signal incident on the materials, and subtracting the normalized incident linear response (approximated by the material response to the probe 3 ps before the arrival of the pump).

$$\Delta R_{\text{probe}}(\tau) = R(\tau)_{\text{with pump}} - R(\tau)_{\text{without pump}} \quad (3.10)$$

$$= \frac{\int I_R(\omega, \tau) d\omega}{\int I_0(\omega) d\omega} - \frac{\int I_R(\omega, \tau = -3ps) d\omega}{\int I_0(\omega) d\omega} \quad (3.11)$$

$$\Delta T_{\text{probe}}(\tau) = T(\tau)_{\text{with pump}} - T(\tau)_{\text{without pump}} \quad (3.12)$$

$$= \frac{\int I_T(\omega, \tau) d\omega}{\int I_0(\omega) d\omega} - \frac{\int I_T(\omega, \tau = -3ps) d\omega}{\int I_0(\omega) d\omega} \quad (3.13)$$

The numerical integrations were performed over the range of measured wavelengths spanning  $\approx 1.495\text{eV}$  to  $\approx 1.505\text{eV}$ .

The integrated signals show changes to the total energy traveling in the reflected and transmitted probe directions at different pump-probe delays, peaking at  $\approx +15\%$  change in transmission and  $\approx -10\%$  change in reflection near  $\tau = 0ps$  delay. Interestingly, at  $\tau \approx -1ps$ , where transient gain in the reflection direction is at its peak, the total change in  $\Delta R$  is near a maximum. The sum of these contributions,  $\Delta S_{\text{probe}}$  gives the total change in normalized energy traveling in probe directions:

$$\Delta S_{\text{probe}} = \Delta R_{\text{probe}} + \Delta T_{\text{probe}} + \Delta A_{\text{probe}} \quad (3.14)$$

and is shown in black, hollow triangles in Fig 3.18). The result is small but positive and peaks at  $+7\%$  at a slightly negative delay, near to when the transient gain in reflection also peaked. The appearance of this net change in energy traveling in

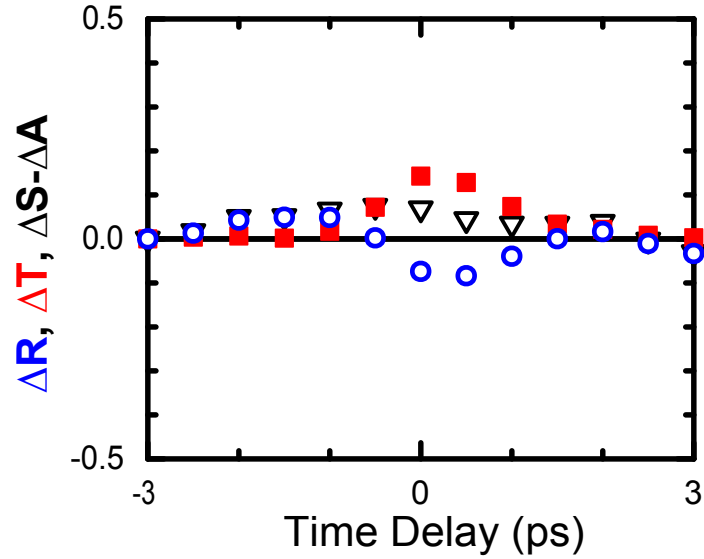


Figure 3.18: Numerically integrated differential reflection (blue, hollow circles) and transmission (red, filled squares) at different time delays. Also included is  $\Delta S - \Delta A = \Delta R + \Delta T$  at each time delay (black, hollow triangles).

both transmitted and reflected probe directions, and its temporal correlation to the appearance of transient gain in reflection seems to hint that the transient gain is due to energy transfer from the pump into the probe direction. However, it could also indicate a change in absorption (linear absorption is  $\approx 13\%$  for this probe spectral position and width) inside the structure (i.e. less probe energy absorbed would result in more probe energy traveling in the transmitted/reflected directions). As such, this data shows either that the increase in  $\Delta S_{\text{probe}} - \Delta A_{\text{probe}}$  is due either to energy transfer from the pump, or suppressed absorption of the probe. In either case, however, it is still possible that the transient spectral gain observed is due to redistribution of probe energy.

To further investigate this transient gain, measurements have been performed using *narrowband* co-circularly polarized pump and probe pulses. Use of narrowband pulses simplifies the experiment in the sense that it precludes nonlinear mixing of very different probe frequencies and the pump. For example, if the transient gain at the low energy band edge is due to transfer from the

high energy photonic band edge, then the transient gain should disappear for the narrowband data.

### 3.3.2 Measurement of nonlinearities in BSQWs using narrowband probe pulses

An additional pulse shaper was introduced into the probe arm before the sample (Fig. 3.19), and the resulting signal in the reflected direction was both spectrally integrated (Fig. 3.20) and spectrally resolved (Fig. 3.21). A probe with temporal and spectral width close to the pump's spectral/temporal width (1.5 meV spectral FWHM, 1.3ps temporal FWHM) was chosen to maximize the temporal overlap between the two.

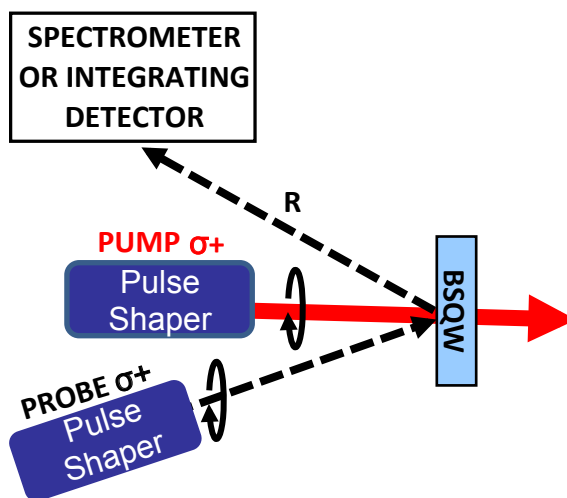


Figure 3.19: Experimental setup for narrowband measurements.

Spectrally *integrated* ++ pump-probe results of the narrowband probe were taken and are shown on the left in Fig. 3.20 and contrasted with measurements done using a broadband probe spectrally resolved after the sample on the right. No significant gain is seen by the narrowband probe. This appears to show that the transient gain seen in the broadband probe data has disappeared in the narrowband probe case, which is a somewhat surprising result. If the transient

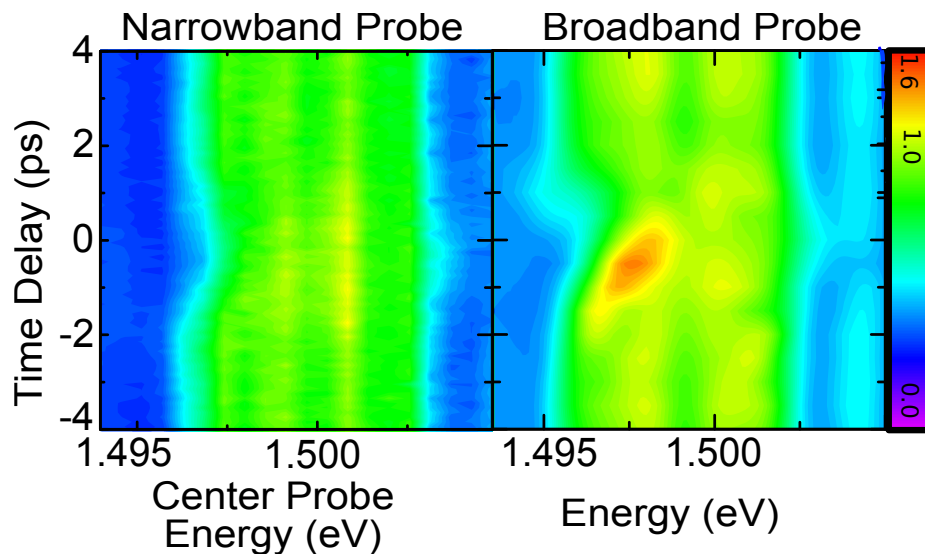


Figure 3.20: Spectrally resolved reflection as a function of pump-probe time delay. (left) Integrated measurements of the narrowband probe vs. pump-probe delay. Note that the x-axis in this case is the energy at the center of the probe pulse. (right) Similar results taken with a broadband probe. The x-axis in this case is the absolute energy being spectrally resolved.

gain is due to energy transfer from the pump, one might have expected the spectrally sharp transient gain seen in the broadband data (Fig. 3.15) to appear here as a convolution with the narrowband probe spectrum, i.e., washed out but still present.

To dig a little deeper, spectrally *resolved* measurements of the narrowband probe were taken and are shown in Fig. 3.21. Here, the linear reflection from the Bragg structure is shown in the light shaded area, and the pump in the dark shaded area for reference. Time delays ranging from  $-2.5\text{ps}$  to  $+2\text{ps}$  are shown from top to bottom.

The red dots in Fig. 3.21 show the normalized reflection for a probe pulse centered at each wavelength. At negative delays, large spectral gain is again seen, with reflection values well above 2, in agreement with what was previously seen in the broadband measurements. As the delay between the pump and probe pulses is brought towards  $\tau = 0\text{ps}$  the gain disappears. While only one set of these

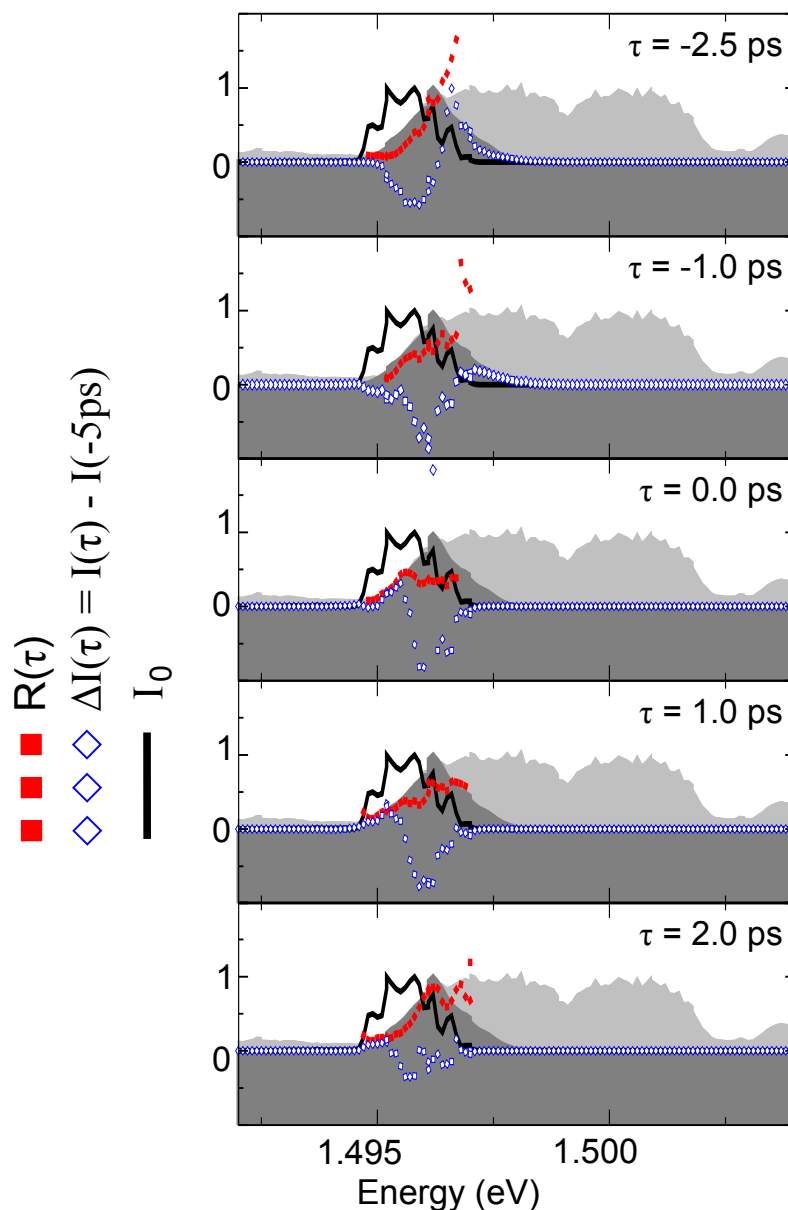


Figure 3.21: Spectrally resolved reflection (red filled squares) and differential intensity (blue open diamonds) of a narrowband probe (black solid line) co-circularly polarized with the pump vs. pump-probe delay. Rows show different time delays ranging from  $\tau = -2.5\text{ps}$  (top) to  $\tau = +2\text{ps}$  (bottom). The pump spectrum (dark shaded area) and linear reflection from the structure (light shaded area) are shown for reference.

measurements is shown here, for probe energies near to the pump, these results are fairly robust.

When the incident probe energy (black line) drops below the detection limit,

it is impossible to determine a reflection coefficient for light (i.e. the spectrally resolved reflection goes to infinity here since we are dividing by zero). To further examine these results then, it is helpful to look at the change in intensity  $\Delta I = I(\tau) - I(\tau = -5\text{ps})$  of the reflected probe (blue diamonds in Fig. 3.21), in order to remove these normalization problems. The intensity seen at  $\tau = -5\text{ps}$  is used as a base reference here rather than the intensity when no pump is present in order to remove possible changes due to shot to shot carrier accumulation in the sample. At negative delays,  $\Delta I$  shows probe energy in the range outside of the incident probe, where (as mentioned) the reflection can't be meaningfully normalized.

The narrowband measurements suggest the spectral gain is due to probe redistribution. First, integrating the energy traveling in the reflected probe direction after the sample shows no increase in the total energy present, suggesting that pump energy is transferred. When the signals are spectrally resolved after the sample, transient gain appears on the low energy edge of the bandgap and at negative pump-probe delays, as was seen in the broadband data. Furthermore, at negative pump-probe delays, the probe spectrum appears to be shifted, with energy depleted on the low energy side, and energy increasing on the high energy side.

### 3.3.3 Time delay dependence of the nonlinear response

In addition, some questions also remain regarding the pump-probe delay dependence of these features. The transient gain seen in the reflection direction appears at negative time delays and sweeps towards the middle of the bandgap as the delay is brought towards zero. At positive delays, only distortions of the bandgap are seen. Conversely, signals traveling in the transmitted probe direction show transient gain at only positive time delays. The maximum intensity scattered in the FWM direction is seen near  $\tau = 0\text{ps}$  pump-probe delay.

The transient gain appearing at negative delays, (i.e. the probe arrives before the pump) in the reflection direction is not surprising. Nonlinear responses that are skewed towards negative delays have previously been seen and explained in terms gratings formed in the materials. Maximum scattering can occur when the pump and probe overlap enough to form a strong grating in the structure, but where there is also significant time after this interaction for the stronger pump to interact with those gratings, as is the case at slight negative delays [89]. The transient gain appearing in transmission at positive delays is more surprising. In this case, the probe arrives after the pump pulse, and hence the pump-probe interaction is weak, as well as the amount of time the pump can interact with any gratings formed.

The origin of this difference is likely due to the wavelength dependent dispersion inside the structure. The wavelength dependent dispersion was discussed in some detail in Sec. 3.2, and can vary drastically across the bandgap. As such, it is possible that different pulse wavelengths that are transmitted/reflected from the structure experience varying interaction times in the structure, leading to variability in the magnitude of the gratings formed, and the amount of time available for the pump to interact with those gratings based on the spectral portion of the probe being investigated.

As an example, pulse wavelengths outside the low energy edge of the bandgap encounter almost no index difference between the barrier and well materials, and pass through the material with the speed given by the background index of GaAs. Probe wavelengths spectrally below the bandgap transmit through without significant slowing by the material, and encounter very little interaction with the pump itself. Hence, very few changes occur at negative pump-probe delays. When the probe enters at the same time or after the pump pulse, interaction time increases due to slowing of the pump on the low energy edge

of the BSQW bandgap.

Finally, looking at Fig. 3.16, the maximum distortion to the stopgap in reflection and transmission appears close to zero delay, as does the FWM signal, when temporal overlap of the pump and probe are at a maximum.

### 3.3.4 Preliminary theoretical analysis of the nonlinear response of BSQWs

To further examine these polarization-dependent optical nonlinearities, simulations have been started using a comprehensive microscopic theory based on a dynamics-controlled truncation scheme (DCT) capable of looking at nonlinearities to all order in the incident fields, and up to third order in the material polarization (i.e. susceptibility). The theory consists of a self-consistent time-dependent transfer matrix solution of Maxwell's equations for inter-well light propagation coupled to equations of the interband polarization induced in each quantum well [108]. The interband polarization is solved for using a microscopic treatment of spin-dependent exciton-exciton interactions. For (++) configurations, the interaction leads to an instantaneous Hartree-Fock repulsion, Pauli blocking, and retarded scattering correlations between pump and probe-induced excitons. For (+-) configurations, only retarded correlations including both scattering and (bound) biexciton correlations are obtained. In the DCT model, only coherent effects are considered. These assumptions lead to some interesting results, reviewed below, but the lack of non-radiative dephasing in the model, and the inclusions of terms higher order in the incident fields (Fig. 3.17 shows a distinct quadratic dependence in pump fluence for signals traveling in the FWM direction) leads to questions about the validity of comparisons between these theoretical results and the experimental ones presented in Sec. 3.3.1.

Results from a typical calculation of the reflectivity in the (++) configuration are shown in Fig. 3.22(b) and are compared with corresponding experimental

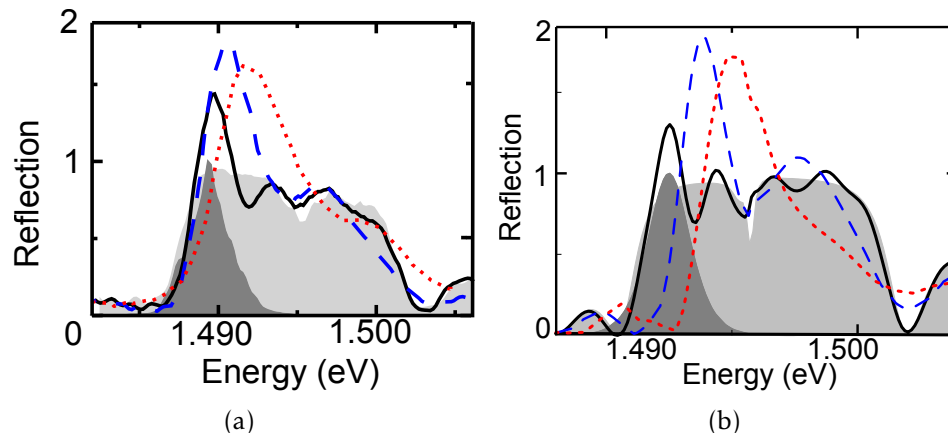


Figure 3.22: (a) Experimentally measured reflection at pump-probe delays of  $-1.5\text{ps}$  (black, solid),  $-1.0\text{ps}$  (blue, dashed) and  $-0.5\text{ps}$  (red, dotted). (b) Theoretically simulated reflection at  $-2.0\text{ ps}$  (black, solid),  $-1.0\text{ps}$  (blue, dashed) and  $-0.6\text{ps}$  (red, dotted). The pump (dark gray shaded area) and linear reflection (light gray shaded area) spectrum are shown for reference.

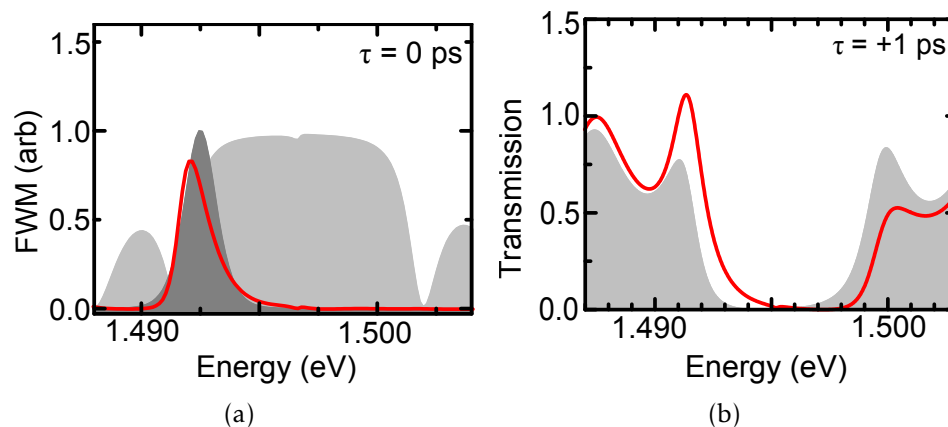


Figure 3.23: Simulated signals traveling in the backwards probe, background free direction, at  $\tau = 0\text{ps}$  pump-probe delay ((a)), and in the transmission direction at  $\tau = +1\text{ps}$  pump-probe delay ((b)). The pump (dark gray shaded area) and linear reflection (light gray shaded area) spectrum are shown for reference.

data in Fig. 3.22(a). The theory shows reflection  $> 1$  on the low energy edge of the bandgap that shifts to higher energies with time delay, in good qualitative agreement with experiment.

In addition, simulations have been done to examine the fields produced in

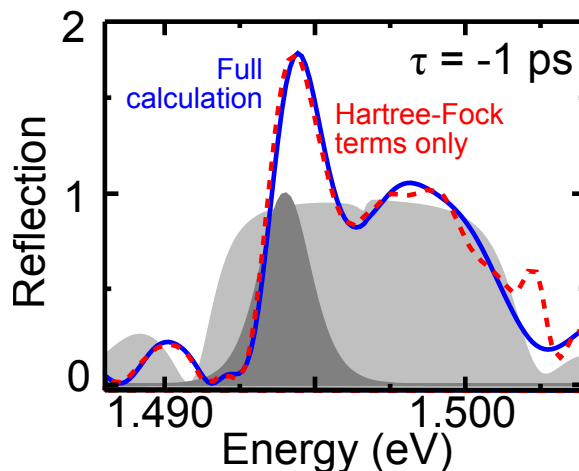


Figure 3.24: Theoretically modeled reflection with all many body effects (solid, blue) included to beyond third order, and only the Hartree-Fock interaction to third order (dashed, red) at a pump-probe delay of  $-1\text{ps}$ . In all figures the linear reflection is shown in the light shaded area, and the pump in the dark shaded area.

both the backwards probe direction, and in the transmission direction. These, again, show good qualitative agreement with the previously shown experimental data (Fig. 3.15). Light with frequencies near the pump, and on the low energy bandedge is scattered in the FWM direction [shown in Fig. 3.23(a)] at  $\tau = 0\text{ps}$  in good agreement with the experimental data (top in Fig. 3.15). Similarly, simulations of the transmitted light at  $\tau = +1\text{ps}$  are shown in Fig. 3.23(b). Transient gain is again seen on the low energy edge of the bandgap, slightly outside the band region, again similar to what is shown in the middle plot of Fig. 3.15.

By turning terms on and off in the theoretical model, the physical mechanisms driving the observed nonlinearities can be identified. Fig. 3.24 shows another full calculation of the reflection from the structure at  $\tau = -1\text{ps}$  and a separate calculation done only with a third-order Hartree-Fock term included (no exciton-exciton interactions or phase space filling effects). The results show the Hartree-Fock repulsion dominates at the lower band edge, yielding the transient gain and distortions seen there. Around the upper band edge and in the  $+-$

channel (not shown), biexciton effects and Pauli blocking terms are necessary for agreement with experiment.

The simulations produce good qualitative agreement with the experimental results shown earlier. However, as was also mentioned earlier, the simulations also include terms beyond third order in the optical field as a form of feedback in the nonlinear interaction, created by the interaction of the pump beams and the FWM fields introduced into the system [107]. Experimental measurements (Fig. 3.17) demonstrating the power dependence of the signals traveling in the FWM direction, showed a  $\chi^{(3)}$  dependence for the nonlinearities seen experimentally.

In addition, as detailed in Ref. [109], the DCT model used for these simulations assumes that all of the carriers created by the pulses are coherent (i.e. the non-radiative dephasing rate of carriers in the system,  $\gamma$ , is equal to or less than twice the radiative dephasing rate of the carriers). The inclusion of incoherent carriers in the DCT model through an ad-hoc approach changes the response of the materials dramatically. These unverified assumptions, and the lack of a comprehensive set of simulations makes it difficult to draw comparisons between the experiments and the theory shown here. Further simulations, done with either a more complete DCT model of the system including incoherent carriers, or using the discrete-level model detailed in Appendix A.4 or Ref. [109], are necessary.

### 3.3.5 Preliminary polarization state measurements

To further examine this transient gain, some initial investigations have begun using ellipsometric measurements. In particular, ellipsometric measurements provide information about the total electric field reflected from the structure, and hence more information about the underlying mechanisms behind these nonlinearities, and responsible for the operation of the all-optical switching demonstrated in Sec. 3.1.1.

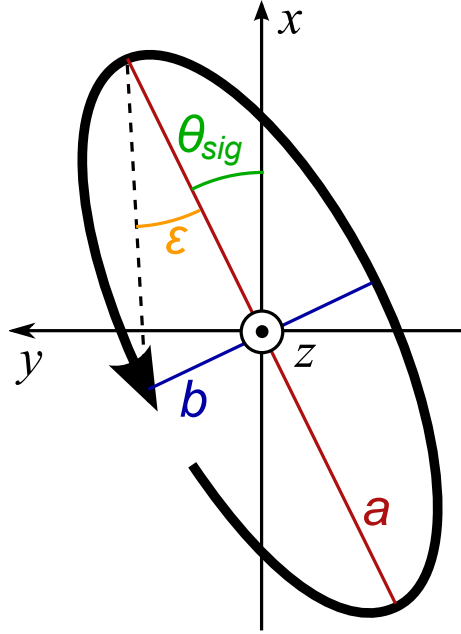


Figure 3.25: The polarization ellipse used for these measurements.  $P$ ,  $\theta_{\text{sig}}$  and  $\epsilon$  are shown, along with the major ( $a$ ) and minor ( $b$ ) axes of the ellipse.

In particular, Gansen et. al. [94] used ellipsometric measurements to explain the operation of an all-optical polarization switch based on multiple quantum wells in terms of optical nonlinear changes to the index of refraction and absorption of the quantum wells. For their analysis, Gansen et. al. [94] measured the total electric field of the transmitted pulse in terms of a polarization ellipse's orientation ( $\theta_{\text{sig}}$ ) and ellipticity ( $\epsilon$ ) (see Fig. 3.25). These measurements were then compared with a model for the transmitted field from the structure in order to identify changes induced during switching to both the polarization dependent absorption ( $\Delta\alpha = \delta\alpha_- - \delta\alpha_+$ , where  $\delta\alpha_{+/-} = \alpha_{+/-}^{\text{pump}} - \alpha_{+/-}^{\text{no pump}}$  represents absorption change for  $\sigma_+$  and  $\sigma_-$  polarized light with and without the pump present) and index ( $\Delta n = \delta n_- - \delta n_+$ , where  $\delta n_{+/-} = n_{+/-}^{\text{pump}} - n_{+/-}^{\text{no pump}}$  represents index changes for  $\sigma_+$  and  $\sigma_-$  polarized light). A definition for the ellipticity was derived in terms of changes in the material absorption:

$$\epsilon = \tan^{-1} \left( \frac{e^{(\Delta\alpha)l} - 1}{e^{(\Delta\alpha)l} + 1} \right) \quad (3.15)$$

and for the orientation of the field in terms of changes to the material's refractive index:

$$\theta_{\text{sig}} = \frac{\omega(\Delta n)l}{2c} \quad (3.16)$$

A similar technique could be used to identify the processes responsible for all-optical switching in BSQWs. Ellipsometric measurements can be used to identify the field reflected from the structures, and compared with a theoretical model of the reflection to identify the changes inside the structure responsible for switching, as well as the nonlinear effects giving rise to those changes (i.e. Pauli blocking or Hartree-Fock local field effects). However, this requires modeling the field reflected from the structure and, the equations used above are not valid for BSQW (i.e. these measurements were done in reflection rather than transmission, and even in transmission, Beer-Lambert's Law does not provide a perfect description of BSQWs).

In a simple model, the BSQWs could be considered a bulk material with wavelength dependent complex index, and the Fresnel equations for polarization dependent reflection of normally incident light used. Some effort has already been put into such a model in Ref. [106], where a wavelength dependent bulk effective index of refraction for BSQW is derived. By iteratively modifying the complex index to produce agreement between the model and the ellipsometric measurements information about the nonlinear response of the material can be determined.

A better solution would compare the reflected E-field from the structure with a full transfer matrix simulation of the nonlinear reflection from BSQWs, and then investigate how those changes correlate to changes in absorption and index on a per-well basis in the material.

To perform these measurements, the electric field of the pulse can be rewritten again in terms of Stokes parameters. To measure these, a quarter wave

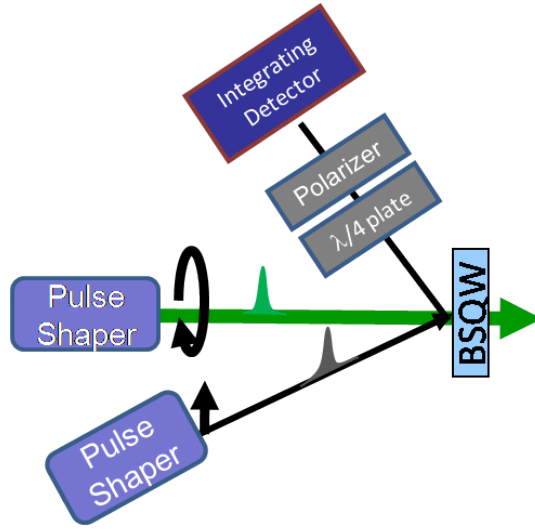


Figure 3.26: Experimental setup for measuring the polarization state of a pulse. A  $\lambda/4$  plate,  $\lambda/2$  plate and a polarizer are placed in the beam path after the sample. Different orientations of the three allow measuring the linear polarization along 4-axes and both circular polarization components.

plate, and polarizer may be placed after the sample as shown in Fig. 3.26, and the intensity of light polarized along the x- and y-axes, along with  $\pm 45^\circ$  with respect to those axes, and the  $\sigma_+$  and  $\sigma_-$  circularly polarized components of a pulse. With this information, all four Stokes parameters can be computed [110, 111]:

$$\begin{aligned}
 S_0 &= I_X + I_Y \\
 S_1 &= I_X - I_Y \\
 S_2 &= I_{+45} - I_{-45} \\
 S_3 &= I_{\sigma_+} - I_{\sigma_-}
 \end{aligned} \tag{3.17}$$

or written in terms of the pulse's degree of polarization ( $P$ ), orientation ( $\theta_{\text{sig}}$ ), and ellipticity ( $\epsilon$ ):

$$\begin{aligned}
 P &= \frac{\sqrt{S_1^2 + S_2^2 + S_3^2}}{S_0} \\
 \sin(2\theta_{\text{sig}}) &= \frac{S_2}{PS_0 \cos(2\epsilon)} \\
 \sin(2\epsilon) &= \frac{PS_3}{S_0}
 \end{aligned} \tag{3.18}$$

We have already begun some of these measurements. Fig 3.27 show the

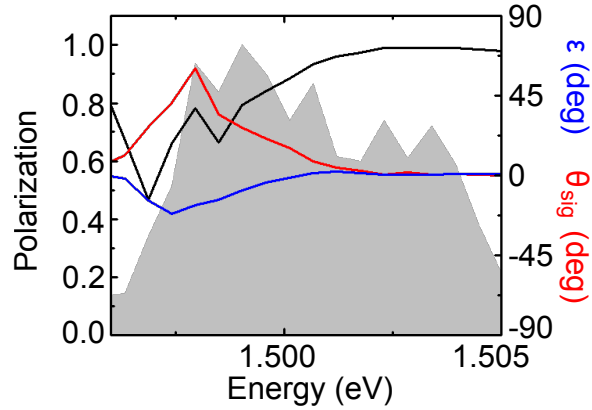


Figure 3.27: Preliminary measurements of the spectrally and temporally integrated polarization state of the probe pulse. The total polarization state (black), along with the orientation (red) and ellipticity (blue) of the pulse are shown at  $\tau = 0ps$  pump-probe delay.

temporally and spectrally integrated degree of polarization ( $P$ , black), orientation ( $\theta_{sig}$ , red) and ( $\epsilon$ , blue) of a narrowband probe pulse as a function of center probe frequency at pump-probe a time delay of  $\tau = 0ps$ . These preliminary results show large changes to the polarization state ( $\approx 50\%$  on the low energy edge of the bandgap) while the pump is present. Almost equal changes occur to both the orientation and ellipticity of the light ( $\delta\theta_{sig} \approx 45^\circ$  and  $\delta\epsilon \approx -20^\circ$ ), again at the low energy edge of the bandgap.

Measurements in MQW polarization switches have shown similar results for the change in polarization state of the light [94] (although with smaller changes in both orientation and ellipticity). The lack of a perfectly defined polarization state here (i.e.  $P \neq 1$ ) likely arises because the signals are being integrated both in frequency and time. Future experiments should repeat these measurements, but spectrally and temporally resolve the light after the sample.

### 3.3.6 Summary of nonlinear measurements of Bragg-spaced quantum wells

To summarize, we have looked at the nonlinear response of Bragg-spaced quantum well materials when excited by a narrowband pump pulse and probed with broadband pulses having the same and opposite circular polarizations. Very few changes were seen in the sample when examined with a probe having the opposite circular polarization as the pump, while large changes are seen when the pump and probe are co-circularly polarized. This has been explained using the spin-selection rules for the 1s-hh exciton. In the limit that higher lying transitions such as the light-hole and many body effects which couple the spin systems can be ignored, the system can be thought of as two independent two-level systems, one coupled to right circularly polarized light, and the other to left circularly polarized light. These two independent two-level systems give rise to two-independent reflection bandgaps, one coupled to right circularly polarized light and one to left. On the low energy edge of the bandgap (below the exciton resonance) this model appears to work well. The changes seen here are likely due to either Pauli blocking or Hartree-Fock local field effects, which do not couple the two spin-systems. On the high energy edge of the bandgap (above the exciton resonance), changes are seen by probe pulses having both the same and opposite circular polarization as the pump. This indicates that higher lying transitions or biexciton effects in the material are visible at these energies.

In addition, transient spectral gain appears in reflection at negative pump-probe time delays, and in transmission at positive pump-probe time delays. The origin of this feature was investigated by measuring signals traveling in the background-free, backwards-probe direction. The signals appear at the low energy edge of the bandgap, near where the pump pulse was located for these experiments, and display a quadratic dependence on pump fluence, and a linear dependence on probe fluence. As such, the nonlinearities investigated in these

experiments and leading to the transient gain seen in reflection and transmission are assumed to be due to a  $\chi^{(3)}$ , four-wave-mixing process in the material.

The  $\chi^{(3)}$  processes can give rise to such gain through two distinct methods, either transient energy transfer from the pump into the probe directions, or through redistribution of probe energy. We have begun some investigation into which is the causing the gain seen in these experiments. Integrating measurements performed with broadband probe pulses, the total energy traveling in both transmitted and reflected probe directions was investigated. A net increase was observed in the integrated sum of change in reflection and transmission. This seems to indicate that a transfer of energy from the pump direction, or a decrease in the amount of energy absorbed by the material is occurring, though neither explanation excludes the possibility of redistribution of probe energy.

Measurements were also performed with narrowband probe pulses in order to remove any effects that might be caused by broadband spectral redistribution (i.e. probe energy at the high energy edge of the bandgap moving to the low energy edge), looking in the reflected probe direction. These narrowband measurements show no net increase in reflection in the integrated probe measurements. Spectral resolving the probe shows the presence of spectral gain again, but is suggestive that it results due to probe redistribution.

Some questions still remain about the differences in time delay for the appearance of transient gain in the reflection, transmission and FWM directions. To further investigate these phenomenon, measurements temporally and spectrally resolving the polarization state of the reflected pulse were begun, along with time- and wavelength-integrated ellipsometric measurements. In addition, some preliminary theoretical simulations were also shown. These models seem to indicate that the transient gain on the low energy edge of the bandgap is due to Hartree-Fock, local field effects. However, the simulations include some nonlinear

effects that are beyond third order in the applied fields, and also neglect incoherent carriers in the materials. Comparison of experimental measurements with further simulations taking these things into account should provide information about changes to absorption and index of individual wells, as well as the underlying processes responsible for these changes.

## CHAPTER 4 FUTURE RESEARCH

Because BSQWs represent such unique photonic structures, there's a range of avenues for this research to continue in, from those dealing with applications of these structures in various optical communications systems, to those focused on the science of nonlinearities in resonant photonic materials. A few potential areas for future research are briefly reviewed here.

### 4.1 Pulse amplification

While some transient gain from BSQWs has been investigated here, theoretical investigations (mentioned previously in Sec. 3.3.6) have predicted even larger signal amplification (as much as 40 times gain in the reflection direction) [107]. The origin of these nonlinearities in the theoretical model is a feedback loop produced by signals traveling in the FWM and pump directions. Initially a temporally long pump pulse and temporally short probe pulse are simultaneously incident on the material. A polarization grating forms in the material due to the interference of the beams and light is scattered in different directions, including the background-free FWM direction discussed in Sec. 3.3.6. After the short probe pulse leaves the sample, the longer pump continues to interact with the polarization grating and the FWM fields produced by light scattered from this grating. This interaction produces new polarization gratings in the structure and light is again scattered off of these. The process feeds itself, and the scattered pump energy in the reflected direction exponentially rises. When the pump is removed, the polarization gratings decay and the gain disappears.

To experimentally verify these simulations, the reflected probe could be temporally resolved after the sample. The gain seen in reflection should continue after the probe pulse leaves the sample, but while the pump pulse is still present.

While we have produced pump pulses of longer temporal width (narrower spectral width) using pulse shapers in previous experiments, we do so at the loss of a significant amount energy, and as such excite smaller nonlinearities.

In addition, the theoretical simulations shown by Schumacher et. al. in Ref. [107] investigated samples with larger numbers of quantum wells than those presently available ( $N = 1000$  as opposed to the  $N=200$  well samples used in these experiments). While some theoretical investigations of this signal amplification in  $N = 200$  quantum well structures has been done, they predict significantly lower gain (approximately a factor of 3), nearer to what has already been demonstrated.

#### 4.2 All-optical switching

While ultrafast all-optical polarization switching in BSQWs has been demonstrated here, its performance is less than idea. One worth investigating is raising the temperature of operation for the device. While we have investigated switching at both 10K and 80K in this study, ideally such materials would require no active cooling and instead operate at room temperature. However, as the temperature of any quantum well structure is increased, there is a corresponding shift of the band edge energies, and broadening of line widths due to enhanced phonon-electron interactions in the materials. When the InGaAs/GaAs samples studied here are raised to 300K, the bandgaps in both the InGaAs and GaAs layers should shift by approximately equal amounts, but the broadening of the GaAs exciton line width will cause it to spectrally overlap with the  $1s-hh$  exciton resonance in the well layers. As such, the photonic bandgap is difficult to see at room temperature due to absorption in the barriers. Alternative media where this difficulty may be overcome are discussed in Sec. 4.4.

In addition, the switch demonstrated here operates at wavelengths outside of the range typically used in communications applications. Alternative BSQW materials using InGaAs/InP quantum wells with exciton resonances near 0.85eV

( $\approx 1.5\mu\text{m}$ ) have been recently investigated theoretically by Wang et. al [112]. The simulations predict a reduced contrast ratio (31dB) and decreased throughput ( $\approx 5\%$ ), at theoretical peak switching powers of  $\approx 30\text{MW}/\text{cm}^2$ . InGaAs/InP BSQW samples for experimental investigation do not exist as of yet.

### 4.3 Slow light

While slow light in BSQWs has been demonstrated here, the nonlinear transmission measurements revealed difficulty in opening an optical window in the bandgap using the AC Stark effect. As such, pulse trapping and releasing has been difficult to implement.

In order to realize tunable slow light in BSQWs, a different method of tuning the Bragg and exciton resonances in the wells must be developed. One potential solution involves tuning the resonances through the quantum confined Stark effect. Contacts placed on the structure would allow a voltage to be created perpendicular to the wells. This potential will pull apart the electrons and holes in the generated excitons. However in quantum wells the confinement due to the well keeps both particles contained in the well layer, and rather than destroying the exciton entirely, the electric field reduces the binding energy and shifts the exciton resonance to higher energies.

The advantage to this type of “nonlinear excitation” is that a pure shift should occur without the four-wave-mixing contributions seen in these optical experiments (i.e. no gratings are induced in the structure). As such, a clean opening and closing of the window within the photonic bandgap may be possible. While electro-optic switching techniques are often slower than their pure-optical counterparts, electronic speeds have increased dramatically in recent years. In addition, electro-optics techniques offer an ease of integration with existing technologies.

Slow-light in BSQWs is ultimately limited by the coherent decay of polaritons

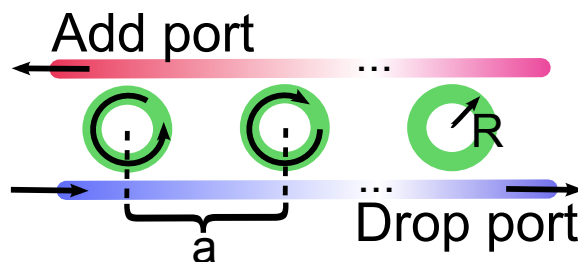


Figure 4.1: Schematic of a periodic ring resonator array. In this particular example, a series of ring resonators are arranged between two waveguides. The rings contain a resonance based on the radius of the ring and its material parameters (index, absorption, etc). By arranging them in periodic arrays separated by some distance ( $a$ ), the photonic properties of the rings can be altered. These and other photonic materials are candidates for next generation all-optical computing platforms and as mediums for tunable slow light.

trapped inside the wells. While one might guess that this decay rate would be around a factor of  $2\gamma$  (the polarization dephasing rate of the system, a few picoseconds in these materials) given in Eq. 3.1, the exact decay time depends on the spectral position of the pulse within the window (see Ref. [38]). If one looks at only a single narrow spectral position the decay rate can be many times greater than  $2\gamma$ . For applications such as the synchronization of pulses with a network clock, or the phase matching of pulses in telecom applications, this could provide enough delay to be useful. However, for applications where longer storage times are needed (for instance, storing pulses for hundreds of bits while a switching fabric is reconfigured) other slow light materials are being investigated.

#### 4.4 Alternative materials

Much of the research on slow light and all-optical switching has recently turned to RPBGs in other types of nano-fabricated materials [113, 114]. Some examples include microring resonators [115, 116, 117], cylinders arranged in periodic arrays [22], woodpile stacks [118], and other types of photonic structures [119, 120].

Microring resonators in particular have attracted a lot of attention for their ability to produce interesting nonlinear effects with relatively small pump fluences. Fig. 4.1 shows an example such structure, constructed by placing "ring" waveguides between two linear waveguides. Light traveling through the linear waveguides couples into the ring structures if a resonance condition is matched. The second wave guide on the far side of the ring couples light out. By placing a series of these rings [121] (or other photonic cavities [122]) separated by a spacing  $\omega_B$  (as shown in Fig. 4.1) the photonic bandstructure of the material becomes similar to the one seen in the BSQW case, with the ring's resonance replacing the exciton resonance.

Nonlinear excitation of such ring structures represents a separate field of research. Typically the Kerr nonlinearities used to induce changes to the refractive index of waveguide structures are small. However, in microring structure pulses are temporally compressed by the photonic band structure of the material and spend extended amounts of time in the ring. As such changes to the refractive index of the material can be introduced with much smaller incident energies. In ring structures, this means that the resonance can be changed dynamically, and pulses can be selectively coupled or uncoupled to the ring material. As an example, an add-drop filter is shown in Fig. 4.1. A strong pump pulse can be used to introduce a shift in the ring resonance and selectively couple light to the drop port [114].

While some optical switching has been demonstrated in photonic structures [115, 123], little research has been done looking at polarization switching. For an all-optical polarization switch to operate, the material needs to demonstrate a dichroism or birefringence which can be altered through nonlinear excitation. Chiral photonic materials which contain a birefringence when no control pulse is present have been produced [118, 124], but at the time of this writing, I am not

aware of any attempts to induce chirality through nonlinear excitation. It may be possible to do so using photonic structures with an embedded quantum well or other optical resonance [125].

## CHAPTER 5 CONCLUSIONS

To summarize, this research has focused on the nonlinear properties of Bragg-spaced quantum wells with large numbers of quantum wells ( $\approx 200$ ), along with applications of those nonlinearities as an all-optical polarization switch, and as a medium for slow light/optical buffers.

An ultra-fast all-optical polarization switch made from Bragg-spaced quantum wells based on the spin-selection rules for the  $hh$ -exciton has been demonstrated. The switch operates using an induced circular dichroism and birefringence due to the two nearly independent spin stopgaps in the structure and tied to the circular selection rules for the  $hh$ -exciton. The polarization switch has high throughput ( $> 40\%$ ), and large contrast ratios ( $> 40\text{dB}$ ) over approximately 0.6THz of bandwidth, At higher temperatures the switch performance decreases, and exhibits reduced switching and recovery times.

In addition, slow light and trapping of optical pulses in these materials was also investigated. The speed of light passing through these materials was measured, and a pulse delay of around 0.6 bits was shown for a single detuning of the bandgap. Dynamically changing this detuning through optical means has proven difficult and will require further investigation, most likely using non-optical methods.

Finally, polarization dependent ultrafast optical nonlinearities in BSQWs were investigated. When excited below resonance in the  $++$  polarization channel, BSQWs show large distortions of the  $\sigma_+$  photonic band structure, especially along the edges of the bandgap, while little change is seen in the  $\sigma_-$  photonic bandgap in the  $+ -$  polarization channel. This dichroism arises because of the spin-selection rules for the  $hh$ -exciton. In the absence of higher-lying levels or higher order

many body effects, the system behaves as two independent two-level systems, one coupled to right circularly polarized light, and the other to left circularly polarized light. The ultrafast recovery is a result of excitation below resonance. Because the excitation is done below resonance, only virtual carriers are created in the materials and the sample recovers its linear reflection and transmission properties when the pump pulse has left the sample.

At negative delays, transient spectral gain is seen in the ++ polarization channel in reflection directions, while at positive delays, transient gain appears in transmission directions. The presence of this transient gain raises questions as to the nonlinearities responsible for its origin. Signals traveling in the background-free backwards probe direction were also spectrally resolved and integrated, and found to have a power dependence consistent with a third-order four-wave-mixing process. Additional measurements were also performed using narrowband probe pulses and also show transient gain at negative delays. Integrated measurements of signals traveling in both the reflection and transmission directions show a net gain in energy traveling along probe directions. This hints that the transient gain is due in part to energy transfer from the pump into the probe direction, rather than a pure redistribution of probe energy.

Additional time-resolved ellipsometric measurements to identify the time dependence of the four-wave-mixing signals and transient gain signals were also proposed. Preliminary time- and spectrally-integrated measurements show large changes to both the orientation and ellipticity of the pulse, as well as a large unpolarized component (which is expected when the polarization state is changing quickly in wavelength and time).

Some preliminary theoretical simulations of the nonlinear response from BSQW were also shown, based on a time dependent transfer matrix solution for pulse propagation through the material, combined with simulations using

a microscopic theory for the evolution of the polarization of excitons in the quantum well. The theory shows a good agreement with experiment, reproducing the qualitative traits of the reflected, transmitted and four-wave-mixing signals. Current simulations suggest that distortions seen on the low energy edge of the bandgap are driven by Hartree-Fock, local field effects arising from arrays of aligned dipoles in the system. However, the dynamics controlled truncation model includes effects beyond third order in the applied field, and fails to take into account incoherent carriers in the system. Further theoretical simulations are necessary in order to make direct reliable with theory.

## APPENDIX A TRANSFER MATRIX DERIVATION

### A.1 Maxwell's equations

Beginning with Maxwell's equations [110]:

$$\begin{aligned}
 \nabla \cdot \vec{B} &= 0 \\
 \nabla \cdot \vec{D} &= \rho_{\text{free}} \\
 \nabla \times \vec{E} &= -\frac{\partial \vec{B}}{\partial t} \\
 \nabla \times \vec{H} &= \vec{J} + \frac{\partial \vec{D}}{\partial t}
 \end{aligned} \tag{A.1}$$

where  $\vec{B}$  is the applied magnetic field,  $\vec{H}$  is the magnetizing field containing the field produced by the medium. Likewise,  $\vec{E}$  is the applied electric field, and  $\vec{D}$  is the displacement field containing the field produced by the medium. For this model,  $\rho_{\text{free}}$  (free charges in the material) and currents inside the medium ( $\vec{J}$ ) are considered within  $\vec{D}$ , and the magnetic susceptibility is ignored ( $\vec{B} = \mu_0 \vec{H}$ ). The displacement electric field  $\vec{D}$  of the material is then rewritten in terms of the polarization of the material:

$$\vec{D} = \epsilon \vec{E} = \epsilon_0 \vec{E} (1 + \chi) = \epsilon_0 \vec{E} + \vec{P} \tag{A.2}$$

where we have defined the susceptibility of the material,  $\chi$ , and  $\vec{P} = \epsilon_0 \chi \vec{E}$ , the polarization of the material. Note that this susceptibility is not necessarily linear, and could be a function of the electronic field,  $\chi(\vec{E})$ . Maxwell's equations can then be combined using the vector identity  $\nabla \times (\nabla \times \vec{V}) = \nabla(\nabla \cdot \vec{V}) - \nabla^2 \vec{V}$  to produce a wave equation for propagation of light:

$$-\nabla^2 \vec{E} + \frac{1}{c^2} \frac{\partial^2 \vec{E}}{\partial t^2} = -\mu_0 \frac{\partial^2}{\partial t^2} (\vec{P}_{\text{res}} + \vec{P}_{\text{B}}) \tag{A.3}$$

where the polarization,  $\vec{P}$  has been separated into a complex resonant component,  $\vec{P}_{\text{res}}(\vec{r}, t)$  (which for BSQWs depends on the  $1s$ - $hh$  exciton), and a background component,  $\vec{P}_{\text{B}}(\vec{r}, t)$ , and speed of light has been identified  $c^2 = \frac{1}{\epsilon_0 \mu_0}$ . This background component can be rewritten in terms of a background index for the material by defining a background susceptibility,  $\vec{P}(\vec{r}, t) = \vec{P}_{\text{res}}(\vec{r}, t) + \vec{P}_{\text{B}}(\vec{r}, t) =$

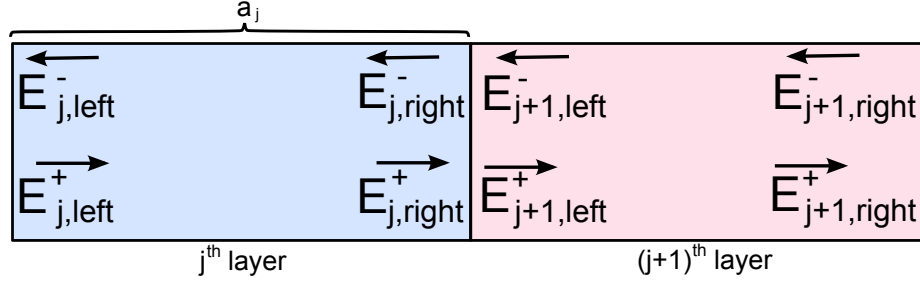


Figure A.1: Transfer matrix across an interface between two materials.

$\vec{P}_{\text{res}}(\vec{r}, t) + \epsilon_0 \chi_B(\vec{r}) E(\vec{r}, t)$ , and a background index  $n_b^2(\vec{r}) = 1 + \chi_B(\vec{r})$  of the medium.

If we only consider propagation in the  $z$ -direction and ignore any possible time dependence in the background index this simplifies to:

$$\left( \frac{\partial^2}{\partial z^2} - \frac{n_b(z)^2}{c^2} \frac{\partial^2}{\partial t^2} \right) E(z, t) = \frac{1}{\epsilon_0 c^2} \frac{\partial^2}{\partial t^2} P_{\text{res}}(z, t) \quad (\text{A.4})$$

## A.2 Transfer matrix for non-resonant media

The waves on each side of a boundary can be related by matching the tangential component of the electric field and its first derivative [40]. To begin with, we consider only phenomenon in non-resonant material and ignore the resonant polarization,  $P_{\text{res}} = 0$ .

Inside a bulk material (for instance, within a single barrier or well layer of a quantum well) the refractive index  $n_b(z)$ , is independent of position, and the solutions to Maxwell's equations are well known plane wave functions,  $E(z, t) = E_0 e^{-i(\omega t - kz)} + c.c.$ , where  $E_0$  denotes the electric field amplitude, and  $\omega$  ( $k = n\omega/c$ ) are its frequency (wave vectors).  $c.c.$  refers to the complex conjugate of the preceding term. In this case it is helpful to rewrite the field in layer  $j$  as:

$$E_j(t, z) = E_j^-(t + \frac{zn_b}{c}) + E_j^+(t - \frac{zn_b}{c}) \quad (\text{A.5})$$

where  $\pm$  denotes the direction the wave is traveling (see Fig. A.1)

Relating the fields on the left side of the layer ( $E_{\text{left}}^{\pm}$ ) to the right side ( $E_{\text{right}}^{\pm}$ )

$$\begin{bmatrix} E_{\text{right}}^- \\ E_{\text{right}}^+ \end{bmatrix} = \begin{bmatrix} e^{-ik_j a} & 0 \\ 0 & e^{ik_j a} \end{bmatrix} \begin{bmatrix} E_{\text{left}}^- \\ E_{\text{left}}^+ \end{bmatrix} \quad (\text{A.6})$$

At the boundary between two layers of different susceptibility, boundary conditions have to be taken into account. In this case, it is helpful to index fields by the layer that they are in such that fields at the right edge of the  $j^{\text{th}}$  layer have the form  $E_{j,\text{right}}^{\pm}$  and fields at the left edge in the  $(j+1)^{\text{th}}$  layer have the form  $E_{j+1,\text{left}}^{\pm}$  (see Fig. A.1). Using Maxwell's equations and matching the tangential and first derivatives of the field as boundary conditions gives:

$$\begin{aligned} E_{j,\text{right}}^- + E_{j,\text{right}}^+ &= E_{j+1,\text{left}}^- + E_{j+1,\text{left}}^+ \\ ik_j E_{j,\text{right}}^- - ik_j E_{j,\text{right}}^+ &= ik_{j+1} E_{j+1,\text{left}}^- - ik_{j+1} E_{j+1,\text{left}}^+ \end{aligned} \quad (\text{A.7})$$

Using  $k_j = n_j \omega / c$ , these two equations can be solved for  $E_j^+$  and  $E_j^-$  and the solution written as a second transfer matrix:

$$\begin{bmatrix} E_{j+1,\text{left}}^- \\ E_{j+1,\text{left}}^+ \end{bmatrix} = \begin{bmatrix} \frac{n_j + n_{j+1}}{2n_{j+1}} & \frac{n_j - n_{j+1}}{2n_{j+1}} \\ \frac{n_j - n_{j+1}}{2n_{j+1}} & \frac{n_j + n_{j+1}}{2n_{j+1}} \end{bmatrix} \begin{bmatrix} E_{j,\text{right}}^- \\ E_{j,\text{right}}^+ \end{bmatrix} \quad (\text{A.8})$$

where  $E_j^{\pm}$  represents the waves traveling in both the right (+) and left (-) directions on each side of an interface, and  $j$  is an integer numbering the layers in the material.

The total transfer matrix through a layer and then across a boundary into another layer can be written as a product of these two matrices. Dropping the left and right notation since all of these waves are on the left side of a layers now:

$$\begin{bmatrix} E_{j+1}^- \\ E_{j+1}^+ \end{bmatrix} = \underbrace{\begin{bmatrix} \frac{n_j + n_{j+1}}{2n_{j+1}} & \frac{n_j - n_{j+1}}{2n_{j+1}} \\ \frac{n_j - n_{j+1}}{2n_{j+1}} & \frac{n_j + n_{j+1}}{2n_{j+1}} \end{bmatrix}}_{\text{Interface}} \underbrace{\begin{bmatrix} e^{-ik_j a} & 0 \\ 0 & e^{ik_j a} \end{bmatrix}}_{\text{Layer}} \begin{bmatrix} E_j^- \\ E_j^+ \end{bmatrix} = \mathcal{M}_j \begin{bmatrix} E_j^- \\ E_j^+ \end{bmatrix} \quad (\text{A.9})$$

which is Eq. 2.11 in the text.

### A.3 Transfer matrix with quantum well susceptibility

When  $\vec{P}_{\text{res}}$  is non-zero, as is the case in BSQWs, boundary conditions must be reconsidered. This section will follow the treatment set out in Refs. [38] and [126].

In the bulk material the tangential component of the field has to be continuous.

Thus:

$$E_j^+(t - \frac{zn_b}{c}) + E_j^-(t + \frac{zn_b}{c}) = E_{j+1}^+(t - \frac{zn_b}{c}) + E_{j+1}^-(t + \frac{zn_b}{c}) \quad (\text{A.10})$$

remains the same.

Assuming the wells are thin compared to the envelope of the field, they can be considered as a  $\delta$ -function in space such that,  $P_{\text{res}} = \sum_j^N \delta(z - z_j) p_j(t)$  where  $P_{\text{res}}$  is the total polarization of the material,  $j$  indexes the quantum wells,  $z_j$  ( $p_j$ ) is the position (polarization) of the  $j^{\text{th}}$  quantum well in the system. Integrating Eq. A.4 from  $z - \epsilon$  (the left side of the quantum well) to  $z + \epsilon$  (the right side of the quantum well), and taking the limit as  $\epsilon \rightarrow 0$  we find:

$$\frac{\partial}{\partial z} \left[ E_{j+1}^+(t - \frac{zn_b}{c}) + E_{j+1}^-(t + \frac{zn_b}{c}) - E_j^+(t - \frac{zn_b}{c}) - E_j^-(t + \frac{zn_b}{c}) \right] = \frac{1}{\epsilon_0 c^2} \frac{\partial^2}{\partial t^2} p_j(t) \quad (\text{A.11})$$

Combining Eq. A.10 and Eq. A.11, and rewriting the left side in terms of time derivatives:

$$E_{j+1}^+(t - \frac{zn_b}{c}) = E_j^+(t - \frac{zn_b}{c}) - \frac{1}{2\epsilon_0 n_b c} \frac{\partial}{\partial t} p_j(t) \quad (\text{A.12})$$

$$E_{j+1}^-(t + \frac{zn_b}{c}) = E_j^-(t + \frac{zn_b}{c}) - \frac{1}{2\epsilon_0 n_b c} \frac{\partial}{\partial t} p_j(t) \quad (\text{A.13})$$

Further solutions of this equation require a model for the polarization of the well,  $p_j(t)$ . Appendix A.4 details a simple model. Taking just the linear  $\chi^{(1)}$  term from it, we can write:

$$\frac{\partial}{\partial t} p_m(t) = -i(\omega_x - i\gamma) p_m(t) + \frac{i|\tilde{\phi}^{2D}(0)|^2 |\varphi|^2}{\hbar} E(z_m, t) \quad (\text{A.14})$$

and

$$\chi^{(1,2D)}(\omega) = \frac{|\tilde{\phi}^{2D}(0)|^2 |\varphi|^2}{\epsilon_0 \hbar} \frac{1}{(\omega - \omega_x) - i\gamma} \quad (\text{A.15})$$

where  $\omega_x$  is the frequency of the resonance,  $\tilde{\phi}^{2D}(\vec{r} = 0)$  is the 2D-exciton wavefunction for electrons and holes separated by  $\vec{r}$ ,  $\varphi$  is the amount of the dipole aligned with the electric field, and  $\gamma$  is the non-radiating dephasing rate of the system. Using this expression in Eq. A.13, performing a Fourier transform and rewriting  $p_j(\omega) = \epsilon_0 \chi(\omega) E(\omega)$  where  $E(\omega)$  is defined in Eq. A.10 this can be written

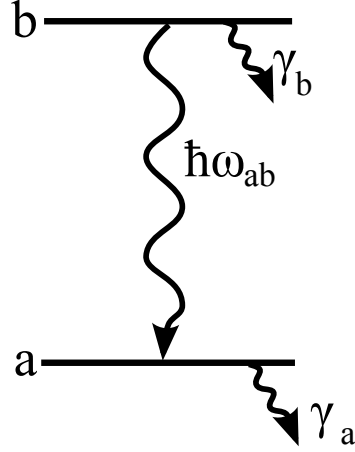


Figure A.2: A simple closed two level system with individual level decay rates,  $\gamma_{ab}$ .

in transfer matrix form:

$$\begin{bmatrix} E_{j+1}^- \\ E_{j+1}^+ \end{bmatrix} = \begin{bmatrix} 1 + \frac{i\omega}{2n_b c} \chi^{(1,2D)}(\omega) & \frac{i\omega}{2n_b c} \chi^{(1,2D)}(\omega) \\ -\frac{i\omega}{2n_b c} \chi^{(1,2D)}(\omega) & 1 - \frac{i\omega}{2n_b c} \chi^{(1,2D)}(\omega) \end{bmatrix} \begin{bmatrix} E_j^- \\ E_j^+ \end{bmatrix} \quad (\text{A.16})$$

Finally, this must be multiplied by the propagation matrix (Eq. A.6) to give Eq. 2.19.

#### A.4 Bloch Equations

When  $\vec{P}_{\text{res}}$  is non-zero, some method must be implemented to model it. A simple model is laid out here, while more complex ones are discussed in Ref. [126] and [127], To begin, we look at the  $m^{\text{th}}$  quantum well in the material, where, as earlier, we have written the polarization of the well as  $p_m(t)$  (the  $m$ 's will be dropped from here on out for conciseness).

Using a simple two level system like the one shown in Fig. A.2, we can write the evolution of the system in terms of Hamiltonian:

$$H = H_{0,aa/bb} + H_{\text{int}} + H_{\text{Coul}} \quad (\text{A.17})$$

where  $H_{0,aa/bb} = E_{a/b}$  denotes the atomic Hamiltonian,  $H_{\text{int}}$  denotes the interaction Hamiltonian of particles with electronic fields in the system in this semiclassical treatment, and  $H_{\text{Coul}}$  represents Coulomb interactions between particles in the system. To begin we will set this Coulomb term equal to zero. We can then use the

electric dipole approximation to describe the interaction part of the Hamiltonian:

$$H_{\text{int}} = -\wp E(t) \quad (\text{A.18})$$

where  $E(t)$  is the incident field,  $\wp$  is expectation value of the dipole moment matrix element  $\mu = -e\langle i|x|j\rangle$ ,  $i$  and  $j$  represent states for the particles in the system, and  $x$  is the position operator.

We also assume that the diagonal parts of the dipole moment operator are zero so that  $\mu_{aa} = \mu_{bb} = 0$  and hence  $H_{\text{int},aa} = H_{\text{int},bb} = 0$ . If the wave function for a particle in this system is expanded in terms of its "pure" states, a and b such that its wave vector,  $\Phi = c_a\phi_a + c_b\phi_b$ . The system can then be described by a density matrix given by:

$$\rho = \begin{bmatrix} \rho_{aa} & \rho_{ab} \\ \rho_{ba} & \rho_{bb} \end{bmatrix} \quad (\text{A.19})$$

where  $\rho_{ij} = c_i c_j$  and  $\rho_{ab} = \rho_{ba}^*$ . This density matrix has an equation of motion given by the Von Neuman equation:

$$i\hbar \frac{\partial \rho}{\partial t} = [H, \rho] \quad (\text{A.20})$$

where the right hand term denotes the commutator of the Hamiltonian and the density matrix. Solving for the equations of motions:

$$\dot{\rho}_{ba} = -i\omega_{ba}\rho_{ba} + \frac{1}{\hbar}\wp E(t)(\rho_{bb} - \rho_{aa}) \quad (\text{A.21})$$

$$\dot{\rho}_{bb} = \frac{1}{\hbar}(\wp E^*(t)\rho_{ab} - \rho_{ba}\wp E(t)) \quad (\text{A.22})$$

$$\dot{\rho}_{aa} = \frac{1}{\hbar}(\wp E(t)\rho_{bb} - \rho_{ab}\wp E^*(t)) \quad (\text{A.23})$$

Adding in the decay terms shown in Fig. A.2 phenomenologically, this becomes:

$$\dot{\rho}_{ba} = -(i\omega_{ba} + \gamma)\rho_{ba} - \frac{1}{\hbar}\wp E(t)(\rho_{bb} - \rho_{aa}) \quad (\text{A.24})$$

$$\dot{\rho}_{bb} = -\gamma_b\rho_{bb} - \frac{1}{\hbar}(\wp E^*(t)\rho_{ab} - \wp E(t)\rho_{ba}) \quad (\text{A.25})$$

$$\dot{\rho}_{aa} = \gamma_a\rho_{aa} + \frac{1}{\hbar}(\wp E(t)\rho_{ba} - \wp E^*(t)\rho_{ab}) \quad (\text{A.26})$$

In general, analytical solutions to Eq. A.24 - Eq. A.26 are not possible. However, solutions can be derived using conventional time-dependent perturbation theory. If  $\wp E^*(t)$  is small, we can expand the density matrix in powers of

perturbation such that:

$$\rho_{ba} = \rho_{ba}^{(0)} + \rho_{ba}^{(1)} + \rho_{ba}^{(2)} + \dots \quad (\text{A.27})$$

$$\rho_{bb} = \rho_{bb}^{(0)} + \rho_{bb}^{(1)} + \rho_{bb}^{(2)} + \dots \quad (\text{A.28})$$

$$\rho_{aa} = \rho_{aa}^{(0)} + \rho_{aa}^{(1)} + \rho_{aa}^{(2)} + \dots \quad (\text{A.29})$$

where the superscripts terms indicate the power of the incident field multiplying the term.

$$\dot{\rho}_{ba} = -(\imath\omega_{ba} + \gamma)\rho_{ba} - \frac{\imath}{\hbar}\wp E(t)(\rho_{bb} - \rho_{aa}) \quad (\text{A.30})$$

$$\dot{\rho}_{bb} = -\gamma_b\rho_{bb} - \frac{\imath}{\hbar}(\wp E^*(t)\rho_{ab} - \wp E(t)\rho_{ba}) \quad (\text{A.31})$$

$$\dot{\rho}_{aa} = \gamma_a\rho_{aa} + \frac{\imath}{\hbar}(\wp E(t)\rho_{ba} - \wp E^*(t)\rho_{ab}) \quad (\text{A.32})$$

To begin, we assume an initially unexcited system such that  $\rho_{aa}^{(0)} = 1$ ,  $\rho_{bb}^{(0)} = 0$ , and  $\rho_{ab}^{(0)} = 0$ . Substituting these back into the density matrix equations for terms where no field is multiplying the incident field, we find:

$$\dot{\rho}_{ba}^{(1)} = \frac{\imath}{\hbar}\wp E(t) \quad (\text{A.33})$$

$$\dot{\rho}_{bb}^{(1)} = -\gamma_b\rho_{bb}^{(1)} \quad (\text{A.34})$$

$$\dot{\rho}_{aa}^{(1)} = \gamma_a\rho_{aa}^{(1)} \quad (\text{A.35})$$

At this point, an expression for the input field is necessary in order to progress. Although one can use arbitrary fields and numerical integration techniques, we instead use the simple case of cw-fields propagating in the z-direction to continue here, such that  $E(t) = \frac{1}{2}(\mathcal{E}_S e^{i(\omega_S t - k_S z)} + c.c. + \mathcal{E}_C e^{i(\omega_C t - k_C z)} + c.c.)$ , where  $\mathcal{E}_S$  and  $\mathcal{E}_C$  represent the amplitudes of the signal and control fields, and  $\omega_{S,C}$  and  $k_{S,C}$  their respective amplitudes. Using these fields, the integrals can be formally solved and the first order solutions to the density matrix equations written:

$$\rho_{ba}^{(1)} = \frac{1}{\hbar} \frac{\wp E(t)}{(\omega_x + \omega_S) + \imath\gamma} \quad (\text{A.36})$$

$$\rho_{bb}^{(1)} = 0 \quad (\text{A.37})$$

$$\rho_{aa}^{(1)} = 0 \quad (\text{A.38})$$

The  $(\rho_{bb} - \rho_{aa})$  term in Eq. A.24 leads to the phase-space filling nonlinear

contributions referred to in the text (i.e. the populations of the levels interact to produce a nonlinear response).

When Coulomb effects are considered, they give rise to terms from the interaction of two different dipoles in the system. As such they are, in the exciton picture, two particles interactions (4 particles if holes and electrons are considered separately) and difficult to put into such a model. However, in the Hartree-Fock, local field approximation we can write these interactions in terms of an additional optical local field added to the system such that  $E(t) \rightarrow \tilde{E}(t) = E(t) + E_{\text{LF}}(t)$ .

The polarization of the individual well can then be found using Eq. A.39 and the optical fields applied by taking:

$$p_m^{2D}(t) = |\tilde{\phi}^{2D}(0)|^2 (\rho_{ab}\wp^* + \rho_{ba}\wp) \quad (\text{A.39})$$

Using the expression for  $\rho^{(1)}$  given in Eq. A.38 in Eq. A.39, and solving for  $p_m^{(1,2D)}(\omega) = \epsilon_0 \chi^{(1,2D)}(\omega) E(\omega)$ , one finds:

$$\chi^{(1,2D)}(\omega) = \frac{|\tilde{\phi}^{2D}(0)|^2 |\wp|^2}{\epsilon_0 \hbar} \frac{1}{(\omega - \omega_x) - i\gamma} \quad (\text{A.40})$$

for the first order susceptibility of a simple two-level resonance.

Higher order terms can be found by substituting this expression into the next higher order density matrix equations, and iterating to find the desired order. Local field effects can also be incorporated into the model by modifying the incident field such that:

$$\vec{E}(\omega) \rightarrow \vec{E}(\omega) + \vec{E}_{\text{LF}}(\omega) = \vec{E}(\omega) + L_{\text{LF}} \vec{P} \quad (\text{A.41})$$

where  $L_{\text{LF}}$  is a constant known as the local field parameter.

Similarly, EID effects can also be included through an additional EID parameter. Expanding the dephasing of the system in terms of the density of

excited excitons:

$$\gamma(N_e) = \gamma_0 + N_e \frac{\partial \gamma}{\partial N_e} + \dots \quad (\text{A.42})$$

$$\approx \gamma_0 + \tilde{\phi}(0) \frac{\partial \gamma}{\partial N_e} (\rho_{bb} - \rho_{aa}) \quad (\text{A.43})$$

$$= \gamma_0 + \frac{\eta}{2\hbar} (\rho_{bb} - \rho_{aa}) \quad (\text{A.44})$$

where  $\eta = 2\hbar\tilde{\phi}(0)(\partial\gamma/\partial N_e)$  is an adjustable parameter known as EID parameter.

The inclusion of these terms results in a red shift of the exciton resonance, even at linear excitation levels, as well as additional terms appearing in 2<sup>nd</sup> and 3<sup>rd</sup> order terms, multiplied by the local field parameter. For example, the third order polarization including these parameters can be written:

$$\rho_{ab}^{(3)} = \frac{i}{\hbar} \int_{-\infty}^t \wp \vec{E} (\rho_b^{(2)} b - \rho_a^{(2)} a) e^{i(\omega+\gamma)(t'-t)} dt' \quad (\text{A.45})$$

$$- \frac{i\xi}{\hbar} \int_{-\infty}^t \rho_{ab}^{(1)} (\rho_b^{(2)} b - \rho_a^{(2)} a) e^{i(\omega+\gamma)(t'-t)} dt' \quad (\text{A.46})$$

$$- \frac{\eta}{\hbar} \int_{-\infty}^t \rho_{ab}^{(1)} (\rho_b^{(2)} b + \rho_a^{(2)} a) e^{i(\omega+\gamma)(t'-t)} dt' \quad (\text{A.47})$$

where  $\xi = 2|\wp|^2\tilde{\phi}(0)L_{\text{LF}}$  is a modified version of the local field parameter.

A similar derivation of the Bloch equations for Semiconductor systems including excitons is given in Ref. [126], but is based on a microscopic formulation and allows particles with distinct wavevectors.

**APPENDIX B**  
**TRANSFER MATRIX SOLUTIONS FOR THE PHOTONIC BANDSTRUCTURE**  
**AND REFLECTIVITY OF BSQWS**

Continuing a review of derivation done by Yang et. al. in Ref. [38], starting with Eq. 2.19, the transfer matrix for a single quantum well unit cell:

$$\mathcal{M} = \begin{bmatrix} \alpha(1 + \beta) & \frac{1}{\alpha}\beta \\ \alpha\beta & \frac{1}{\alpha}(1 - \beta) \end{bmatrix} \quad (\text{B.48})$$

where  $\alpha = e^{ika}$ ,  $\beta = i\omega\chi^{2D}(\omega)/2n_b c$ ,  $\chi^{2D}(\omega) = \frac{|\tilde{\phi}^{2D}(0)|^2 \wp^2}{\epsilon_0 \hbar} \frac{1}{\omega - \omega_X - i\gamma}$  is the susceptibility of the exciton,  $k = n_b \omega / c$  is the wave vector of the photon (assumed here to be in the z-direction),  $a$  is the width of a single quantum well/barrier unit (this contains the Bragg frequency  $a = c\pi/n_b \omega_B$ ), and  $\omega_X$  is (in the case of BSQWs) the frequency of the exciton resonance. In this expression for the susceptibility,  $\wp$  is the dipole moment of the exciton,  $\tilde{\phi}^{2D}(\vec{r})$  is the 1s-exciton 2D-wavefunction at an electron-hole separation given by  $\vec{r}$ ,  $n_b$  is the background refractive index of the system, and  $\gamma$  is the polarization dephasing rate of the system. Eigenvalues of the system can be solved for:

$$\mathcal{M} \begin{bmatrix} E_N^+ \\ E_N^- \end{bmatrix} = \lambda_{\pm} \begin{bmatrix} E_N^+ \\ E_N^- \end{bmatrix}. \quad (\text{B.49})$$

Solving this equation gives:

$$\lambda_{\pm} = e^{ik_{\pm}a} = \frac{\alpha(1 + \beta) + (1/\alpha)(1 - \beta) \pm \sqrt{[\alpha(1 + \beta) + (1/\alpha)(1 - \beta)]^2 - 4}}{2} \quad (\text{B.50})$$

These two eigenvalues can then be combined to describe the dispersion relation for photons in the crystal:

$$\cos(ka) = \cos(qa) + \frac{\Gamma}{(\omega + i\gamma) - \omega_X} \left( \frac{\omega}{\omega_X} \right) \sin(qa) \quad (\text{B.51})$$

where  $\Gamma = \frac{|\tilde{\phi}(0)^{2D}|^2 |\wp|^2 \omega_X}{2n_b \epsilon_0 \hbar c}$  is the radiative decay rate of the transition.

Alternatively, expanding the transfer matrix equation in terms of these eigenvalues and their associated eigenvectors:

$$\begin{bmatrix} E_T \\ 0 \end{bmatrix} = \mathcal{M}^N \begin{bmatrix} E_0 \\ E_R \end{bmatrix} = \mathcal{M}^N [c_+ W_+ + c_- W_-] = c_+ \lambda_+^N \begin{bmatrix} v_+ \\ u_+ \end{bmatrix} + c_- \lambda_-^N \begin{bmatrix} v_- \\ u_- \end{bmatrix} \quad (\text{B.52})$$

where  $N$  is the number of wells present,  $W_{\pm}$  (with components  $v_{\pm}$  and  $u_{\pm}$ ) are the eigenvectors of the matrix, and  $c_{\pm}$  are the coefficients associated with each eigenvector. Setting  $E_N^+$  (no light is incident from the right), the coefficient can be simplified ( $c_-/c_+ = -\lambda_-^N v_+/\lambda_-^N v_-$ ).

Eigenvectors can be solved for directly, as was done originally by Kosbukin [128], or using a slightly more elegant formalism as done by Ivchenko [44]. In Ivchenko's solution the transfer matrix was rewritten in terms of Pauli matrices, and a generating function is used to find each power of  $\mathcal{M}$ . Solving for the eigenvalues, one can find an expression for  $\mathcal{M}^N$ . Ivchenko [44] and Yang et. al. [38] differ slightly in their definition of the transfer matrix, but the two are equivalent if the substitutions  $r = \frac{\beta}{1-\beta}$  and  $t = \frac{1}{1-\beta}$  are used. The reflection can then be written:

$$r_N = \frac{m_{12}}{m_{22}} = \frac{-N\beta}{1-N\beta} = \frac{-iN\Gamma}{\omega - \omega_X - i(\gamma + N\Gamma)} \quad (\text{B.53})$$

where  $N$  is the number of quantum wells in the system.

This expression for the reflection of the structure falls apart when the number of quantum wells grows large [46, 129]. The reasons for this lie further back in the analysis, when microscopic currents were incorporated into the susceptibility in Maxwell's equations. The microscopic quantities in Maxwell's equations were essentially averaged over an area that is "macroscopically small, but microscopically large" [129, 130]. In a non-local response theory, the currents and fields created by excited particles in the system are taken into account on a microscopic scale, and allowed to interact with other charges in the system. The result is typically a small shift and broadening of the resonance. However, in the case of BSQWs with large numbers of wells, both the shift and broadening take on a significant spectral dependence on  $\omega$ , resulting in the removal of what is typically called the "super-radiant" mode of the Bragg-structure, and its spectral evolution into a top-hat shape.

## REFERENCES

- [1] W. J. Johnston, M. Yildirim, J. P. Prineas, A. L. Smirl, H. M. Gibbs, and G. Khitrova. All-optical spin-dependent polarization switching in Bragg-spaced quantum well structures. *Appl. Phys. Lett.*, 87(10):101113, 2005.
- [2] Z. S. Yang, N. H. Kwong, R. Binder, and A. L. Smirl. Distortionless light pulse delay in quantum-well Bragg structures. *Opt. Lett.*, 30:2790, 2005.
- [3] W. J. Johnston, J. P. Prineas, and A. L. Smirl. Ultrafast all-optical polarization switching in Bragg-spaced quantum wells at 80 k. *J. Appl. Phys.*, 101(4):046101, 2007.
- [4] J. P. Prineas, W. J. Johnston, M. Yildirim, J. Zhao, and A. L. Smirl. Tunable slow light in Bragg-spaced quantum wells. *Appl. Phys. Lett.*, 89:241106, 2006.
- [5] A. Macleod. The early days of optical coatings. *J. Opt. A: Pure Appl. Opt.*, 1(S):779–783, 1999.
- [6] J. W. S. Rayleigh. On the remarkable phenomenon of crystalline reflexion described by Prof. Stokes. *Philos. Mag.*, 26:256–265, 1888.
- [7] Taylor H. D. *On the Adjustment and Testing of Telescopic Objectives*. York: T Cooke and Sons, 1891.
- [8] F. Hurn Constable. The cause of the colours shown during the oxidation of metallic copper. *Proc. R. Soc. London, Ser. A*, 115(772):570–588, August 1927.
- [9] P H Lissberger. Optical applications of dielectric thin films. *Rep. Prog. Phys.*, 33(1):197–268, 1970.
- [10] R. A. Denton. The manufacture of military optics at the Frankford Arsenal during W.W.II. *Opt. News*, 15(7):24, 1989.
- [11] M. Moss. *Range and Vision: The first 100 years of Barr & Stroud*. Mainstream Publishing Company (Edinburgh) Ltd., 1988.
- [12] H. Bach and D. Krause, editors. *Thin Films on Glass*. Springer-Verlag, 1997.
- [13] K. Iga. Surface-emitting laser — Its birth and generation of new optoelectronics field. *IEEE J. Quantum Electron.*, 6(6):1201, 2000.
- [14] P. Vukusic and J. R. Sambles. Photonic structures in biology. *Nature*, 424:852, 2003.
- [15] P. Vukusic. Natural photonics. *Phys. World*, page 3539, February 2004.

- [16] S. Kinoshita, S. Yoshioka, and K. Kawagoe. Mechanisms of structural colour in the Morpho butterfly: Cooperation of regularity and irregularity in an iridescent scale. *Proc. R. Soc. London, Ser. B*, 269(1499):14171421, 2002.
- [17] S. Yoshioka and S. Kinoshita. Effect of macroscopic structure in iridescent color of the peacock feathers. *Forma*, 17(2):169–181, 2002.
- [18] Yablonovitch E. Photonic crystals: Whats in a name? *Opt. Photonics News*, 18(3):12–13, March 2007.
- [19] E. Yablonovitch. Photonic band-gap structures. *J. Opt. Soc. Am. B: Opt. Phys.*, 10:283, 1993.
- [20] S. John. Strong localization of photons in certain disordered dielectric superlattices. *Phys. Rev. Lett.*, 58(23):2486–2489, June 1987.
- [21] J. M. Lourtioz, H. Benisty, V. Berger, J. M. Gerard, D. Maystre, and A. Tchelnokov. *Photonic Crystals: Towards Nanoscale Photonic Devices*. Springer, 1st edition, 2005. 430 pp.
- [22] M. F. Yanik, W. Suh, Z. Wang, and S. Fan. Stopping light in a waveguide with an all-optical analog of electromagnetically induced transparency. *Phys. Rev. Lett.*, 93(23):233903, Dec 2004.
- [23] G. Bastard. *Wave mechanics applied to semiconductor heterostructures*. Les éditions de physique, 1988.
- [24] P. Y. Yu and M Cardona. *Fundamentals of Semiconductors: Optical Properties I*, chapter 6, pages 243–343. Springer, 3rd edition, 2003.
- [25] W. Y. Liang. Excitons. *Phys. Educ.*, 5(4):226–228, 1970.
- [26] G. Grosso and G. P. Parravicini. *Solid State Physics*. Academic Press, 2003.
- [27] C. Weisbuch and B. Vinter. *Quantum Semiconductor Structures*. Academic Press Inc., 1991.
- [28] J. C. Maan, G. Belle, A. Fasolino, M. Altarelli, and K. Ploog. Magneto-optical determination of exciton binding energy in GaAs/Ga<sub>1-x</sub>Al<sub>x</sub>As quantum wells. *Phys. Rev. B: Condens. Matter*, 30(4):2253–2256, Aug 1984.
- [29] D. S. Chemla and D. A. B. Miller. Room-temperature excitonic nonlinear-optical effects in semiconductor quantum-well structures. *J. Opt. Soc. Am. B: Opt. Phys.*, 2(7):1155–1173, 1985.
- [30] Arthur L. Smirl. *Semiconductor Quantum Optoelectronics: From Quantum Physics to Smart Devices*, chapter Coherent exciton dynamics: time resolved polarimetry, pages 25–92. Taylor & Francis, 1st edition, January 1999.

- [31] Hartmut Haug and Stephan W. Koch. *Quantum Theory of the Optical and Electronic Properties of Semiconductors*. World Scientific Publishing Co. Pte. Ltd., 3rd edition, 1990. ISBN 9789810218645.
- [32] C. Ciuti, P. Schwendimann, B. Deveaud, and A. Quattropani. Theory of the angle-resonant polariton amplifier. *Phys. Rev. B: Condens. Matter*, 62(8): R4825–R4828, Aug 2000.
- [33] M. Wegener, D. S. Chemla, S. Schmitt-Rink, and W. Schäfer. Line shape of time-resolved four-wave mixing. *Phys. Rev. A: At. Mol. Opt. Phys.*, 42(9): 5675–5683, Nov 1990.
- [34] J. P. Prineas, C. Cao, M. Yildirim, W. Johnston, and M. Reddy. Resonant photonic band gap structures realized from molecular-beam-epitaxially grown InGaAs/GaAs Bragg-spaced quantum wells. *J. Appl. Phys.*, 100(6): 063101, 2006.
- [35] K. P. O'Donnell and X. Chen. Temperature dependence of semiconductor band gaps. *Appl. Phys. Lett.*, 58(25):2924–2926, 1991.
- [36] C. Weisbuch, M. Nishioka, A. Ishikawa, and Y. Arakawa. Observation of the coupled exciton-photon mode splitting in a semiconductor quantum microcavity. *Phys. Rev. Lett.*, 69:3314–3317, December 1992.
- [37] D. Perry. Low-loss multilayer dielectric mirrors. *Opt. Express*, 4:987, 1965.
- [38] Z. S. Yang, N. H. Kwong, R. Binder, and A. L. Smirl. Stopping, storing, and releasing light in quantum well Bragg structures. *J. Opt. Soc. Am. B: Opt. Phys.*, 22:2144, 2005.
- [39] L. I. Deych, M. V. Erementchouk, A. A. Lisyansky, E. L. Ivchenko, and M. M. Voronov. Exciton luminescence in one-dimensional resonant photonic crystals: A phenomenological approach. *Phys. Rev. B: Condens. Matter*, 76(7):075350, 2007.
- [40] E. Hecht. *Optics*. World Student Series. Addison-Wesley, Reading, Mass., 3rd edition, 1998.
- [41] S. Mogg, N. Chitica, R. Schatz, and M. Hammar. Properties of highly strained InGaAs/GaAs quantum wells for 1.2- $\mu\text{m}$  laser diodes. *Appl. Phys. Lett.*, 81(13):2334–2336, 2002.
- [42] J. C. Harmand, L. H. Li, G. Patriarche, and L. Travers. GaInAs/GaAs quantum-well growth assisted by Sb surfactant: Toward 1.3  $\mu\text{m}$  emission. *Appl. Phys. Lett.*, 84(20):3981–3983, 2004.
- [43] C. López, R. Mayoral, F. Meseguer, J. A. Porto, J. Sánchez-Dehesa, M. Leroux, N. Grandjean, C. Deparis, and J. Massies. Optical studies of highly strained InGaAs/GaAs quantum wells grown on vicinal surfaces. *J. Appl. Phys.*, 81(7):3281–3289, 1997.

- [44] E.L. Ivchenko, A. I. Nesvizhskii, and S. Jorda. Bragg reflection of light from quantum-well structures. *Phys. Solid State*, 36(7):1156–1161, July 1994.
- [45] D. Ammerlahn, J. Kuhl, B. Grote, S.W. Koch, G. Khitrova, H. Gibbs, R. Hey, and K.H. Ploog. Radiative coupling in single quantum wells and Bragg structures. *Phys. Status Solidi B*, 221(1):101–106, Oct 2000.
- [46] T. Ikawa and K. Cho. Fate of the superradiant mode in a resonant Bragg reflector. *Phys. Rev. B: Condens. Matter*, 66(8):085338, Aug 2002.
- [47] K. Cho. Nonlocal theory of radiation-matter interaction: Boundary-condition-less treatment of maxwell equations. *Prog. Theor. Phys., Supp.*, 106:225–233, 1991.
- [48] H. G. Winful, R. Zamir, and S. Feldman. Modulational instability in nonlinear periodic structures: Implications for “gap solitons”. *Appl. Phys. Lett.*, 58(10):1001–1003, 1991.
- [49] B. J. Eggleton, R. E. Slusher, C. M. de Sterke, P. A. Krug, and J. E. Sipe. Bragg grating solitons. *Phys. Rev. Lett.*, 76(10):1627–1630, Mar 1996.
- [50] H. G. Winful. Pulse compression in optical fiber filters. *Appl. Phys. Lett.*, 46(6):527–529, 1985.
- [51] D. Taverner, N. G. R. Broderick, D. J. Richardson, R. I. Laming, and M. Ibsen. Nonlinear self-switching and multiple gap-soliton formation in a fiber Bragg grating. *Opt. Lett.*, 23(5):328–330, 1998.
- [52] H. G. Winful and V. Perlin. Raman gap solitons. *Phys. Rev. Lett.*, 84(16):3586–3589, Apr 2000.
- [53] V. E. Perlin and H. G. Winful. Stimulated Raman scattering in nonlinear periodic structures. *Phys. Rev. A: At. Mol. Opt. Phys.*, 64(4):043804, Sep 2001.
- [54] R. Boyd. *Nonlinear Optics: Processes Resulting from the Intesity-Dependent Refractive Index*. Elsevier Science, 2nd edition, 2003. 569 pp.
- [55] W. Xiao, J. Zhou, and J. Prineas. Storage of ultrashort optical pulses in a resonantly absorbing Bragg reflector. *Opt. Express*, 11(24):3277–3283, 2003.
- [56] W. Chen and D. L. Mills. Gap solitons and the nonlinear optical response of superlattices. *Phys. Rev. Lett.*, 58(2):160–163, Jan 1987.
- [57] B. J. Eggleton and R. E. Slusher. *Nonlinear Photonic Crystals: Nonlinear Propagation in Fiber Gratings*, chapter 8, pages 33–60. Springer Publishing, 2003.
- [58] H. Lee and G. P. Agrawal. Nonlinear switching of optical pulses in fiber Bragg gratings. *IEEE J. Quantum Electron.*, 39(3):508–515, MAR 2003.

- [59] L. Thylen, G. Karlsson, and O. Nilsson. Switching technologies for future guided wave optical networks: potentials and limitations of photonics and electronics. *IEEE Commun. Mag.*, 34(2):106–113, Feb 1996.
- [60] T. S. El-Bawab. *Optical Switching*. Springer Science and Business Media Inc., 2006.
- [61] M. Maier and M. Reisslein. Trends in optical switching techniques: A short survey. *IEEE Network*, 22(6):42–47, November-December 2008.
- [62] Z. Ghassemlooy, W. P. Ng, and H. Le-Minh. Ber performance analysis of 100 and 200 gbit/s all-optical OTDM node using symmetric mach-zehnder switches. *Circuits, Devices and Systems, IEEE Proceedings*, 153(4):361–369, August 2006.
- [63] P.K.A. Wai, L.Y. Chan, L.F.K. Lui, Lixin Xu, H.Y. Tam, and M.S. Demokan. All-optical header processing using control signals generated by direct modulation of a DFB laser. *Opt. Commun.*, 242(1):155–161, November 2004.
- [64] N. Calabretta, H. de Waardt, G. D. Khoe, and H. J. S. Dorren. Ultrafast asynchronous multioutput all-optical header processor. *IEEE Photonics Technol. Lett.*, 16(4):1182–1184, April 2004.
- [65] I. Glesk, Y. K. Huang, C. S. Bres, and P. R. Prucnal. Design and demonstration of a novel optical CDMA platform for use in avionics applications. *Opt. Commun.*, 271(1):65–70, 2007.
- [66] S. K. Kang, T. W. Lee, and H. H. Park. 2.5 Gbit/s multifunctional CMOS transceiver for chip-to-chip optical link. *Electron. Lett.*, 42(7):410–412, March 2006.
- [67] In-Kui Cho, Seung Ho Ahn, Byung Sup Rho, Kyo Seung Chung, and Hyo-Hoon Park. Chip-to-chip optical link system using an optical wiring method. *IEEE Photonics Technol. Lett.*, 19(15):1151–1153, Aug.1, 2007.
- [68] S. D. Smith. Optical bistability, photonic logic, and optical computation. *Appl. Opt.*, 25(10):1550–1564, 1986.
- [69] J. T. Hyland, G. T. Kennedy, A. Miller, and C. C. Button. Spin relaxation and all optical polarization switching at 1.52 micrometres in InGaAs(P)/InGaAsP multiple quantum wells. *Semicond. Sci. Technol.*, 14(3):215–221, 1999.
- [70] D. Marshall and A. Miller. Carrier transport, ultrafast spin dynamics and polarisation switching in InGaAsP multiple quantum wells. *Opt. Quantum Electron.*, page 1019, 2001.
- [71] Emilio E. Mendez and Gerald Bastard. Wannier-Stark ladders and Bloch oscillations in superlattices. *Phys. Today*, 46(6):34, 1993.

- [72] David Emin and C. F. Hart. Existence of wannier-stark localization. *Phys. Rev. B: Condens. Matter*, 36(14):7353–7359, Nov 1987.
- [73] G. D. Boyd, D. A. B. Miller, D. S. Chemla, S. L. McCall, A. C. Gossard, and J. H. English. Multiple quantum well reflection modulator. *Appl. Phys. Lett.*, 50(17):1119–1121, 1987.
- [74] T. H. Wood, C. A. Burrus, D. A. B. Miller, D. S. Chemla, T. C. Damen, A. C. Gossard, and W. Wiegmann. High-speed optical modulation with GaAs/GaAlAs quantum wells in a p-i-n diode structure. *Appl. Phys. Lett.*, 44(1):16–18, 1984.
- [75] G. D. Boyd, A. M. Fox, D. A. B. Miller, L. M. F. Chirovsky, L. A. D’Asaro, J. M. Kuo, R. F. Kopf, and A. L. Lentine. 33 ps optical switching of symmetric self-electro-optic effect devices. *Appl. Phys. Lett.*, 57(18):1843–1845, 1990.
- [76] D. S. McCallum, A. N. Cartwright, X. R. Huang, T. F. Boggess, A. L. Smirl, and T. C. Hasenberg. Enhanced ambipolar in-plane transport in an InAs/GaAs hetero-n-i-p-i. *J. Appl. Phys.*, 73(8):3860–3866, 1993.
- [77] P. F. Davies, C. C. Phillips, and C. Roberts. All-optical reflection modulator using a nonlinear heteronipi structure within an asymmetric fabry-perot optical cavity. *Appl. Phys. Lett.*, 74(24):3717–3719, 1999.
- [78] K. H. Gulden, H. Lin, P. Kiesel, P. Riel, G. H. Döhler, and K. J. Ebeling. Giant ambipolar diffusion constant of n-i-p-i doping superlattices. *Phys. Rev. Lett.*, 66(3):373, 1991.
- [79] M. B. Yairi, C. W. Coldren, D. A. B. Miller, and Jr. J. S. Harris. High-speed, optically controlled surface-normal optical switch based on diffusive conduction. *Appl. Phys. Lett.*, 75(5):597–599, 1999.
- [80] A. Larsson and J. Maserjian. Optically addressed asymmetric fabry-perot modulator. *Appl. Phys. Lett.*, 59(24):3099–3101, 1991.
- [81] A. Migus, A. Antonetti, D. Hulin, A. Mysyrowicz, H. M. Gibbs, N. Peychambarian, and J. L. Jewell. One-Picosecond Optial NOR Gate at Room-Temperature with a GaAs-AlGaAs Multiple-quantum-Well Nonlinear Fabry-Perot Etalon. *Appl. Phys. Lett.*, 46(1):70–72, 1985.
- [82] D. Hulin, A. Mysyrowicz, A. Antonetti, A. Migus, W. T. Masselink, H. Morkoç, H. M. Gibbs, and N. Peyghambarian. Ultrafast all-optical gate with subpicosecond on and off response time. *Appl. Phys. Lett.*, 49(13):749–751, 1986.
- [83] J. Paye and D. Hulin. Monochromatic All-Optical Gate With 1-ps Response-Time. *Appl. Phys. Lett.*, 62(12):1326–1328, MAR 22 1993.
- [84] R. Takahashi, H. Itoh, and H. Iwamura. Ultrafast high-contrast all-optical switching using spin polarization in low-temperature-grown multiple quantum wells. *Appl. Phys. Lett.*, 77(19):2958–2960, 2000.

- [85] H. S. Loka, S. D. Benjamin, and P. W. E. Smith. Optical characterization of low-temperature-grown GaAs for ultrafast all-optical switching devices. *IEEE J. Quantum Electron.*, 34(8):1426–1437, AUG 1998.
- [86] J. P. Prineas, J. Y. Zhou, J. Kuhl, H. M. Gibbs, G. Khitrova, S. W. Koch, and A. Knorr. Ultrafast AC Stark effect switching of the active photonic band gap from Bragg-periodic semiconductor quantum wells. *Appl. Phys. Lett.*, 81(23):4332–4334, 2002.
- [87] H. Shen, M. Wraback, J. Pamulapati, M. Dutta, P. G. Newman, A. Ballato, and Y. Lu. Normal incidence high contrast multiple quantum well light modulator based on polarization rotation. *Appl. Phys. Lett.*, 62(23):2908–2910, 1993.
- [88] Y. Nishikawa, A. Tackeuchi, S. Nakamura, S. Muto, and N. Yokoyama. All-optical picosecond switching of a quantum well etalon using spin-polarization relaxation. *Appl. Phys. Lett.*, 66(7):839–841, 1995.
- [89] A. L. Smirl, J. Dubard, A. G. Cui, T. F. Boggess, and G. C. Valley. Polarization-rotation switch using picosecond pulses in GaAs. *Opt. Lett.*, 14(4):242–244, FEB 15 1989.
- [90] E. J. Gansen. *All-Optical Polarization Switching Techniques Based on the Coherent Many-Body Interactions and The Virtual Excitation of Spin-Polarized Carriers In Semiconductor Quantum Wells*. PhD thesis, The University of Iowa, 2004.
- [91] D. S. McCallum, X. R. Huang, A. L. Smirl, D. Sun, and E. Towe. Polarization Rotation modulator in a Strained [110]-oriented Multiple-quantum-well. *Appl. Phys. Lett.*, 66(21):2885–2887, May 22 1995.
- [92] E. J. Gansen, K. Jarasiunas, and A. L. Smirl. Femtosecond all-optical polarization switching based on the virtual excitation of spin-polarized excitons in quantum wells. *Appl. Phys. Lett.*, 80(6):971–973, 2002.
- [93] M. Yildirim, J. P. Prineas, E. J. Gansen, and A. L. Smirl. A near-room-temperature all-optical polarization switch based on the excitation of spin-polarized “virtual” carriers in quantum wells. *J. Appl. Phys.*, 98(6):063506, 2005.
- [94] E. J. Gansen and A. L. Smirl. Ultrafast polarization modulation induced by the “virtual excitation” of spin-polarized excitons in quantum wells: Application to all-optical switching. *J. Appl. Phys.*, 95(8):3907–3915, 2004.
- [95] W. A. Schroeder, D. S. McCallum, D. R. Harken, M. D. Dvorak, D. R. Anderson, A. L. Smirl, and B. S. Wherrett. Intrinsic and Induced Anisotropy of Nonlinear Absorption And Refraction in Zinc Blende Semiconductors. *J. Opt. Soc. Am. B: Opt. Phys.*, 12(3):401–415, Mar 1995.

- [96] I. Romyantsev, N. H. Kwong, R. Binder, E. J. Gansen, and A. L. Smirl.  $\chi^{(3)}$  analysis of all-optical polarization switching in semiconductor quantum wells. *Phys. Rev. B: Condens. Matter*, 69(23):235329, Jun 2004.
- [97] M. Wraback and H. Shen. A femtosecond, polarization-sensitive optically addressed modulator based on virtual exciton effects in an anisotropically strained multiple quantum well. *Appl. Phys. Lett.*, 76(10):1288–1290, MAR 6 2000.
- [98] S. Tsuda and C. H. B. Cruz. Femtosecond Response-Time In a Polarization-Rotation Switch Using Semiconductor-Doped Glasses. *Opt. Lett.*, 16(20):1596–1598, OCT 15 1991.
- [99] R. Binder, Z. S. Yang, N. H. Kwong, D. T. Nguyen, and Arthur L. Smirl. Light pulse delay in semiconductor quantum well bragg structures. *Phys. Status Solidi B*, 243(10):2379–2383, 2006.
- [100] T. Yasui, R. Takahashi, N. Kondo, T. Nakahara, and H. Suzuki. Ultrafast all-optical pattern matching using differential spin excitation and its application to bypass/drop self-routing for asynchronous optical packets. *J. Lightwave Technol.*, 24:723, 2006.
- [101] Y. Nishikawa, A. Tackeuchi, M. Yamaguchi, S. Muto, and O. Wada. Ultrafast all-optical spin polarization switch using quantum-well etalon. *IEEE J. Quantum Electron.*, 2:661, 1996.
- [102] M. Schaarschmidt, J. Förstner, A. Knorr, J. P. Prineas, N. C. Nielsen, J. Kuhl, G. Khitrova, H. M. Gibbs, H. Giessen, and S. W. Koch. Adiabatically driven electron dynamics in a resonant photonic band gap: Optical switching of a Bragg periodic semiconductor. *Phys. Rev. B: Condens. Matter*, 70(23):233302, Dec 2004.
- [103] M Povolotskyi, J Gleize, A Di Carlo, P Lugli, S Birner, P Vogl, D Alderighi, M Gurioli, A Vinattieri, M Colocci, S Sanguinetti, and R Notzel. Non-linear optical properties of InGaAs/AlGaAs nanostructures grown on (N11) surfaces. *Semicond. Sci. Technol.*, 19(4):S351–S353, 2004.
- [104] P. C. Ku, F. Sedgwick, C. J. Chang-Hasnain, P. Palinginis, T. Li, H. Wang, S. W. Chang, and S. L. Chuang. Slow light in semiconductor quantum wells. *Opt. Lett.*, 29(19):2291–2293, 2004.
- [105] P. Palinginis, S. Crankshaw, F. Sedgwick, E. T. Kim, M. Moewe, C. J. Chang-Hasnain, H. Wang, and S. L. Chuang. Ultraslow light ( $\approx 200$  m/s) propagation in a semiconductor nanostructure. *Appl. Phys. Lett.*, 87(17):171102, 2005.
- [106] Z. Yang, J. E. Sipe, N. H. Kwong, R. Binder, and A. L. Smirl. Antireflection coating for quantum-well bragg structures. *J. Opt. Soc. Am. B: Opt. Phys.*, 24(8):20132022, 2007.

- [107] S. Schumacher, N. H. Kwong, and R. Binder. Large optical gain from four-wave mixing instabilities in semiconductor quantum wells. *Europhys. Lett.*, 81(2):27003 (5pp), 2008.
- [108] R. Takayama, N. H. Kwong, I. Romyantsev, M. Kuwata-Gonokami, and R. Binder. T-matrix analysis of biexcitonic correlations in the nonlinear optical response of semiconductor quantum wells. *Eur. Phys. J. B*, 25:445–462, 2002.
- [109] N. H. Kwong, I. Romyantsev, R. Binder, and A. L. Smirl. Relation between phenomenological few-level models and microscopic theories of the nonlinear optical response of semiconductor quantum wells. *Phys. Rev. B: Condens. Matter*, 72(23):235312, 2005.
- [110] John David Jackson. Classical electrodynamics, 1998.
- [111] M.J. Snelling, D.R. Harken, A.L. Smirl, and E. Towe. Electrooptic polarization modulation in [110]-oriented GaAs-InGaAs multiple quantum wells. *IEEE J. Quantum Electron.*, 33(7):1114–1122, Jul 1997.
- [112] Tao Wang, Gang Li, and Zheng Chen. The theoretical investigation of all-optical polarization switching based on InGaAs(P) Bragg-spaced quantum wells. *Opt. Express*, 16(1):127–132, 2008.
- [113] J. E. Heebner, P. Chak, S. Pereira, J. E. Sipe, and R. W. Boyd. Distributed and localized feedback in microresonator sequences for linear and nonlinear optics. *J. Opt. Soc. Am. B: Opt. Phys.*, 21(10):1818–1832, 2004.
- [114] Shayan Mookherjea and Mark A. Schneider. The nonlinear microring add-drop filter. *Opt. Express*, 16(19):15130–15136, 2008.
- [115] V. Van, T. A. Ibrahim, P. P. Absil, F. G. Johnson, R. Grover, and P. T. Ho. Optical signal processing using nonlinear semiconductor microring resonators. *IEEE J. Quantum Electron.*, 8(3):705–713, May/June 2002.
- [116] T. A. Ibrahim, K. Amarnath, L. C. Kuo, R. Grover, V. Van, and P. T. Ho. Photonic logic NOR gate based on two symmetric microring resonators. *Opt. Lett.*, 29(23):2779–2781, 2004.
- [117] T. A. Ibrahim, V. Van, and P. T. Ho. All-optical time-division demultiplexing and spatial pulse routing with a GaAs/AlGaAs microring resonator. *Opt. Lett.*, 27(10), 2002.
- [118] M. Thiel, G. von Freymann, and M. Wegener. Layer-by-layer three-dimensional chiral photonic crystals. *Opt. Lett.*, 32(17):2547–2549, 2007.
- [119] P. Tran. All-optical switching with a nonlinear chiral photonic bandgap structure. *J. Opt. Soc. Am. B: Opt. Phys.*, 16(1):70–73, 1999.

- [120] P. Tran. Optical limiting and switching of short pulses by use of a nonlinear photonic bandgap structure with a defect. *J. Opt. Soc. Am. B: Opt. Phys.*, 14(10):2589–2595, 1997.
- [121] S. Blair and K. Zheng. Intensity-tunable group delay using stimulated raman scattering in silicon slow-light waveguides. *Opt. Express*, 14(3):1064–1069, 2006.
- [122] M. F. Yanik and S. Fan. Stopping light all optically. *Phys. Rev. Lett.*, 92(8):083901, Feb 2004.
- [123] Takasumi Tanabe, Masaya Notomi, Satoshi Mitsugi, Akihiko Shinya, and Eiichi Kuramochi. All-optical switches on a silicon chip realized using photonic crystal nanocavities. *Appl. Phys. Lett.*, 87(15):151112, 2005.
- [124] Benfeng Bai, Kuniaki Konishi, Xiangfeng Meng, Petri Karvinen, Anni Lehmuskero, Makoto Kuwata-Gonokami, Yuri Svirko, and Jari Turunen. Mechanism of the large polarization rotation effect in the all-dielectric artificially chiral nanogratings. *Opt. Express*, 17(2):688–696, 2009.
- [125] A. Brunetti, M. Vladimirova, S. Cronenberger, D. Scalbert, M. Nawrocki, and J. Bloch. Linear dichroism in a GaAs microcavity. *Superlattices and Microstructures*, 41(5-6):429 – 433, 2007. Proceedings of the 6th International Conference on Physics of Light-Matter Coupling in Nanostructures, 6th International Conference on Physics of Light-Matter Coupling in Nanostructures.
- [126] G. Khitrova, H. M. Gibbs, F. Jahnke, M. Kira, and S. W. Koch. Nonlinear optics of normal-mode-coupling semiconductor microcavities. *Rev. Mod. Phys.*, 71(5):1591, October 1999.
- [127] P. Meystre and M. Sargent III. *Elements of Quantum Optics*. Springer-Verlag, 3rd edition, 1999.
- [128] V. A. Kosobukin. Transmission and reflection of light by semiconductor superlattices in the region of excitonic resonances. *Fiz. Tverd. Tela*, 34:3107–3118, 1992.
- [129] K. Cho. *Optical Response of Nanostructures: Microscopic Nonlocal Theory*. Springer-Verlag Berlin, 2003.
- [130] L. Pilozzi, A. D’Andrea, and K. Cho. Spatial dispersion effects on the optical properties of a resonant Bragg reflector. *Phys. Rev. B: Condens. Matter*, 69(20):205311, May 2004.